NTNU
Norwegian University of
Science and Technology

Stress sensitivity of velocities in anisotropic rocks

Rock models comparison and true-triaxial apparatus description

Marcin Duda

Petroleum Geosciences
Submission date: August 2017
Supervisor: Rune Martin Holt, IGP
Co-supervisor: Jørn Stenebråten, SINTEF

Norwegian University of Science and Technology
Department of Geoscience and Petroleum

Abstract

The purpose of this study was to investigate the effects of anisotropy on elastic parameters of rocks, and to compare various types of anisotropic rock models with the use of ultrasonic data obtained with a true-triaxial loading apparatus.

In the first part of the thesis, general concept of anisotropy is presented. Anisotropy sources and quantification methods are characterised, and its influence on seismic waves velocity is described. Grain pack, inclusion and microscopic classes of models are introduced. The thesis examines two of the presented models, an inclusion proposed by Fjær (2006) and a macroscopic model published by Prioul et al. (2004) - their general features, characteristics of modelling procedure, results and their limitations. Due to technical difficulties, the ultrasonic measurements on transversely isotropic Berea and Colton sandstones subjected to hydrostatic and biaxial loading used to test the models are taken from Coyner (1984) and Cruts et al. (1995), respectively.

The results of the tests show that both models are well suited to reproducing elastic stiffness parameters estimated from ultrasonic measurements. However, their characteristics entail significantly different methodologies and suggest that the models may be used interchangeably, depending on modelling conditions, interpreter expectations and amount of available experimental data.

The second part of the thesis focuses on the true-triaxial loading apparatus owned by SINTEF Petroleum Research and Norwegian University of Science and Technology. It describes performance tests and modifications introduced to the apparatus, and discusses possible causes of equipment malfunctions. Despite all the changes, performance of the apparatus has not been sufficiently improved. The author recommends further modification to the apparatus before any other uses are considered.

To my Parents, who encouraged my curiosity,
and to Joanna, for her unlimited patience.

Acknowledgements

I would like to express my sincere gratitude to my supervisors, Rune Holt and Jørn Stenebråten, for their help and guidance. I really enjoyed our discussions, consultations and conversations. I hope I was not too tiresome.

I wish to acknowledge SINTEF Petroleum Research for giving me access to their laboratory facilities. I would like to thank the laboratory personnel, especially Anna Stroisz and Dawid Szewczyk, for their support and comforting words.

Finally, I want to thank William G. Allen and Howard T. Hallowell for making my work much easier, and mechanical workshop at Department of Geoscience and Petroleum, efficiency of which never ceased to amaze me.

Table of contents

List of figures

List of tables

Abbreviations

APE	Average Percent Error
LVDT	Linear Variable Differential Transformer
NTNU	Norwegian University of Science and Technology
PEEK	Polyether Ether Ketone
PVC	Polyvinyl Chloride
SE	Squared Error
SP	Sample Placement (System)
TI	Transverse Isotropy
VTI	Vertical Transverse Isotropy

1. Introduction

Anisotropic behaviour of the rock has inspired multiple publications in the last few decades. One of the most important reasons to investigate this phenomena is the influence of anisotropy on seismic data, which makes it interesting not only from the academia's point of view, but also important for hydrocarbons exploration and production planning and safety. Anisotropy studies have been proven to be useful for velocity and in-situ stress field estimation, reservoir and overburden characterization and monitoring, fractures propagation and flow modelling (Wild, 2011).

The main objective of this thesis was to prepare a theoretical framework for anisotropy investigation, carry out laboratory experiments on anisotropic rock samples with the use of true-triaxial loading apparatus and combining both, the theory and the experimental data, to compare different types of mathematical models used to simulate the anisotropic behaviour of rocks under arbitrary stresses. Due to technical difficulties, the experimental part of the project was not successfully completed, and the measurements results had to be obtained from other publications. Therefore, the thesis was divided into two separate parts – chapters 2-5 consist of theoretical introduction and summary of numerical modelling, meanwhile chapter 6 describes the technical part of the project carried out in SINTEF Petroleum Research Formation Physics Laboratory. Some of the theoretical concepts investigated in this thesis were already described in the Specialization Project report submitted in December 2016.

Chapters 2 and 3 aim to recapitulate the current state of knowledge about anisotropy. The most prominent theories referring to the origin of anisotropy were described, as well as observable effects of the rock anisotropy and methods of anisotropic effects quantification – the elastic stiffness coefficients and Thomsen's parameters, their definitions and physical meaning. Different symmetry classes of a medium, i.e. isotropy, transverse isotropy and orthorhombic symmetry, were characterised. In order to set a basis for further comparison, three main approaches to the rock behaviour modelling were described (granular, inclusion and macroscopic) and exemplified with different models proposed by various authors.

Chapters 4 and 5 describe and summarise the comparison of an inclusion (Fjær, 2006) and a macroscopic model (Prioul et al., 2004). Due to technical problems with the true-triaxial apparatus, the models were tested with the use of the results of ultrasonic waves velocity measurements carried out under hydrostatic and non-hydrostatic stresses,

published by Coyner (1984) and Cruts et al. (1995). The most prominent features, application workflow variations and limitations of the models were investigated. The quality of the stiffness coefficients approximations was assessed in terms of partial and global misfit errors and trends reconstruction. Chapters 2-4, forming the first part of the thesis, are summarised together in chapter 5.

The second part of the thesis (chapter 6) consists of a description of the true-triaxial apparatus and laboratory work - the apparatus maintenance, modification and upgrading workflow and analysis of the apparatus subsystems tests carried out mostly between January and June 2017 (except for the first sensors calibration performed in November 2016). Apparatus limitations and flaws are investigated and described, and their probable causes listed. Chapter 6 is concluded with the analysis of the apparatus performance, discussion of the probable causes of the apparatus malfunction and further modifications which could allow to remove the existing problems.

2. Theory of rock anisotropy

2.1. Concept of rock anisotropy

Anisotropy is generally defined as a dependence of the response of the medium upon its spatial orientation. In the context of the seismic waves it may be described as the dependence of the seismic wave velocity upon the propagation direction within the material. Anisotropy is caused by material heterogeneities present on a scale smaller than the volume in which anisotropy in observed. This phenomena is not limited to particular type of heterogeneities nor range of dimensions – anisotropy can result from features both as large as a sequence of layers of various types of rocks and as small as molecular configuration of the particles composing the medium (Fjær et al., 2008). There are two main mechanisms responsible for creation of the anisotropic effects.

The *intrinsic* anisotropy originates from the original internal structure of the material and properties of its building elements. This type of anisotropy may result from preferred orientation of anisotropic minerals and pores (Vernik, 1993), presence of bedding planes (Thomsen, 1986) and resultant parallel alignment of minerals along them (Sayers, 1994). The induced, or *extrinsic* (i.e. produced by other mechanisms), anisotropy results from the impact of stress acting on the rock mass and may be related to factors such as high levels of differential stress (Nur and Simmons, 1969), presence of set (or sets) of aligned microcracks (Hudson, 1981) and large scale fractures (Mueller, 1991). Both types of anisotropy are schematically presented in fig. (2-1).

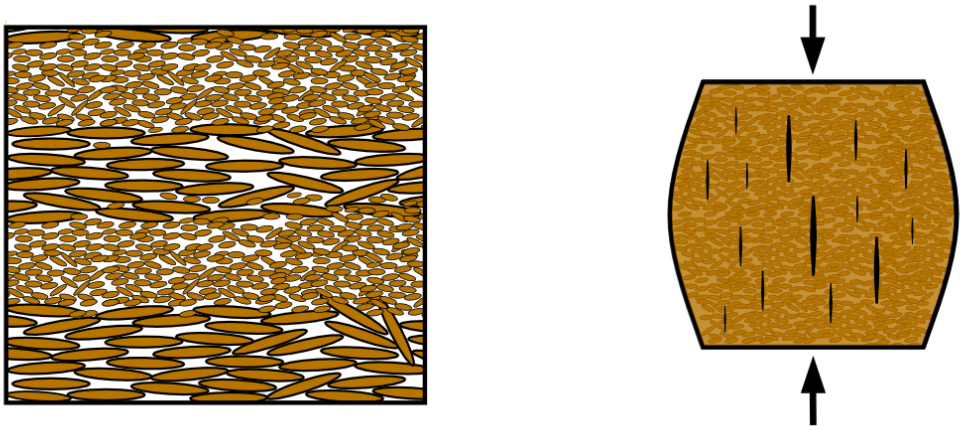

Fig. 2-1. Anisotropy sources: intrinsic (left) and extrinsic (right) (after: Fjær et al., 2008)

Despite the variety of possible causes and its complexity, anisotropy can be included in the mathematical description of elastic waves propagation within the medium. It is usually made with use of effective parameters, describing the behaviour of the entire medium volume rather than characteristics of each grain, pore or crack. Introduction of anisotropy into the mathematical formulation tends to require numerous input parameters, which are not easily extracted from the geophysical and the laboratory data making the entire process rather difficult. In order to simplify the calculations it is a common practice to neglect the influence of anisotropy. However, this may introduce significant error in computations, as it is experimentally confirmed that most earth crust rocks are anisotropic (Thomsen, 1986). It was also analytically described and experimentally observed that a stack of isotropic elements may produce anisotropic behaviour of the entire medium volume. This phenomena is most clearly observed in wide-angle survey results (Backus, 1962).

2.2. Stress-strain relationship in anisotropic material

The stress-strain relationship in an anisotropic sample may be expressed using equation (1). As in the isotropic case, strain is directly related to stress, and this relation is proportional to a corresponding elastic stiffness matrix element. The choice of the stiffness matrix element depends on the orientation of the material and the direction of the exerted stress and the investigated strain.

$$\sigma_{ij} = \sum_{l,k} C_{ijkl} \cdot \varepsilon_{lk} \tag{1}$$

where: $\sigma_{ij} - stress, C_{ijkl} - elastic\ stiffness\ matrix, \varepsilon_{kl} - strain.$

The elastic stiffness matrix expressed in a three-dimensional space allows i,j,k and l to vary from 1 to 3, and hence in the most general form it consists of 81 elements. The number of constants reduces significantly due to symmetry of the matrix, equation (2), resulting from characteristics of stress and strain tensors presented in equations (3) and (4).

$$C_{ijkl} = C_{jikl} = C_{ijlk} = C_{jilk} \tag{2}$$

$$\sigma_{ij} = \sigma_{ji} \tag{3}$$

$$\varepsilon_{ij} = \frac{1}{2}\left(\frac{\partial u_i}{\partial x_j} + \frac{\partial u_j}{\partial x_i}\right) \tag{4}$$

where: $u - displacement, x - displacement\ direction.$

Equation (2) indicates that the change of order in pairs of indices (*i.e.* ij and kl) does not affect the value of the element. It suggests that deformation amplitude depends only on a direction and magnitude of a stress vector, but not on its sense. Taking into consideration the strain energy relation with strain and stress derivatives, expressed by equation (6), it is possible to validate equation (5) and further limit the number of the elastic stiffness matrix constants. As the order of the indices pairs is neither affecting the constant, the number of independent elements of the C_{ijkl} matrix goes down to 21. This number of constants is sufficient to describe behaviour of any anisotropic medium and may be even further reduced in case of presence of additional symmetries.

$$C_{ijkl} = C_{klij} \tag{5}$$

$$\frac{\partial \sigma_i}{\partial \varepsilon_j} = \frac{\partial^2 W}{\partial \varepsilon_j \partial \varepsilon_i} = \frac{\partial \sigma_j}{\partial \varepsilon_i} \tag{6}$$

where: $W - strain\ energy$ ($potential\ energy\ stored\ by\ deformed\ body\ per\ unit\ volume$).

2.2.1. Orthorhombic symmetry

In case of three mutually perpendicular symmetry planes the medium can be described as orthorhombically symmetric. This kind of symmetry is assumed to be sufficient to reasonably capture the properties of rocks (Fjær et al., 2008). Assuming that the symmetry axes coincide with the three-dimensional coordinate system axes, an expression for stress vector should be identical for situation in which one of the axes is turned around (*i.e.* $x' = x$, $y' = y$, $z' = -z$). However, the produced results are different due to the change of the constants sign according to the axis inversion operation shown by equation (7).

$$\begin{bmatrix} 1 & 0 & 0 \\ 0 & 1 & 0 \\ 0 & 0 & -1 \end{bmatrix} \begin{bmatrix} a_{11} & a_{21} & a_{31} \\ a_{12} & a_{22} & a_{32} \\ a_{13} & a_{23} & a_{33} \end{bmatrix} \begin{bmatrix} 1 & 0 & 0 \\ 0 & 1 & 0 \\ 0 & 0 & -1 \end{bmatrix} = \begin{bmatrix} a_{11} & a_{21} & -a_{31} \\ a_{12} & a_{22} & -a_{32} \\ -a_{13} & -a_{23} & a_{33} \end{bmatrix} \tag{7}$$

If applied to all stress components and possible orientations, the number of independent elements of the elastic stiffness matrix is reduced to nine elements: $C_{1111}, C_{2222}, C_{3333}, C_{1122}, C_{1133}, C_{2233}, C_{2323}, C_{1313}$ and C_{1212}. In order to simplify the indices, Voigt's notation is used: $11 \rightarrow 1, 22 \rightarrow 2, 33 \rightarrow 3, 23 \rightarrow 4, 13 \rightarrow 5, 12 \rightarrow 6$. Vanishing elements can be replaced with 0, and therefore the elastic stiffness matrix and the stress and the strain vectors simplify to expressions (8), (9) and (10), respectively.

$$\boldsymbol{C} = \begin{bmatrix} C_{11} & C_{12} & C_{13} & 0 & 0 & 0 \\ C_{12} & C_{22} & C_{23} & 0 & 0 & 0 \\ C_{13} & C_{23} & C_{33} & 0 & 0 & 0 \\ 0 & 0 & 0 & C_{44} & 0 & 0 \\ 0 & 0 & 0 & 0 & C_{55} & 0 \\ 0 & 0 & 0 & 0 & 0 & C_{66} \end{bmatrix} \tag{8}$$

$$\boldsymbol{\sigma} = \begin{bmatrix} \sigma_x \\ \sigma_y \\ \sigma_z \\ \tau_{yz} \\ \tau_{xz} \\ \tau_{xy} \end{bmatrix} \tag{9}$$

$$\boldsymbol{\varepsilon} = \begin{bmatrix} \varepsilon_x \\ \varepsilon_y \\ \varepsilon_z \\ 2\Gamma_{yz} \\ 2\Gamma_{xz} \\ 2\Gamma_{xy} \end{bmatrix} \tag{10}$$

The above vectors include terms for both normal ($\sigma_x, \sigma_y, \sigma_z, \varepsilon_x, \varepsilon_y$ and ε_z) and shear components ($\tau_{yz}, \tau_{xz}, \tau_{xy}, 2\Gamma_{yz}, 2\Gamma_{xz}$ and $2\Gamma_{xy}$), allowing to cover both forms of deformation. Normal components indices points the axis along which stress is exerted or the body is deformed. In case of the shear components, the first index indicates "face" of the body (perpendicular to the axis given by the index) to which the interaction is applied and the second specifies the direction of stress loading or deformation. Distribution of the stress components around a three-dimensional body is presented in fig. (2-2).

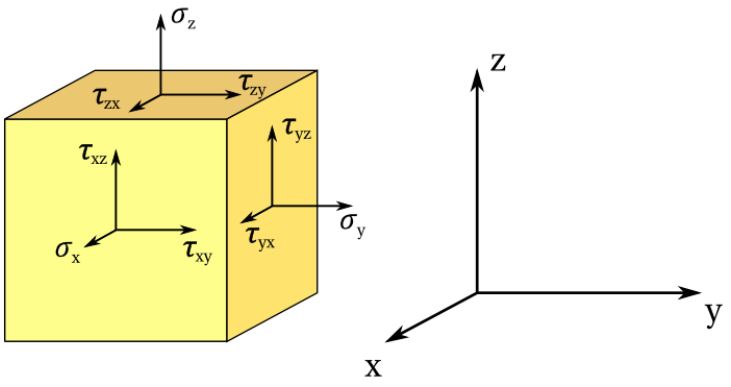

Fig. 2-2. Stress tensor visualization.

To determine which elements of the matrix should be considered, it is necessary to solve equation (11), expressing the final form of stress-to-strain relationship, for each of the stress vector components.

$$\boldsymbol{\sigma} = \boldsymbol{C}\,\boldsymbol{\varepsilon} \tag{11}$$

The resultant expressions (12) are sufficient to describe most types of rocks. Stiffness matrix coefficients $C_{11}, C_{12}, C_{13}, C_{22}, C_{23}$ and C_{33} are related to stresses and deformations along the axes, meanwhile coefficients C_{44}, C_{55} and C_{66} are exclusively used for calculating relations between shear stresses and shear strains with additional scaling factor of two.

$$\begin{aligned}
\sigma_x &= C_{11}\varepsilon_x + C_{12}\varepsilon_y + C_{13}\varepsilon_z \\
\sigma_y &= C_{12}\varepsilon_x + C_{22}\varepsilon_y + C_{23}\varepsilon_z \\
\sigma_z &= C_{13}\varepsilon_x + C_{23}\varepsilon_y + C_{33}\varepsilon_z \\
\tau_{yz} &= 2C_{44}\,\Gamma_{yz} \\
\tau_{yz} &= 2C_{55}\,\Gamma_{xz} \\
\tau_{yz} &= 2C_{66}\,\Gamma_{xy}
\end{aligned} \tag{12}$$

2.2.2. Isotropy

Isotropy is an extreme case of symmetry leading to significant simplification of the stiffness coefficients matrix. The number of independent parameters reduces to two, transforming the stress-to-strain relationship into equations (13).

$$\begin{aligned}
\sigma_x &= (\lambda + 2G)\varepsilon_x + \lambda\varepsilon_y + \lambda\varepsilon_z \\
\sigma_y &= \lambda\varepsilon_x + (\lambda + 2G)\varepsilon_y + \lambda\varepsilon_z \\
\sigma_z &= \lambda\varepsilon_x + \lambda\varepsilon_y + (\lambda + 2G)\varepsilon_z \\
\tau_{yz} &= 2G\,\Gamma_{yz} \\
\tau_{yz} &= 2G\,\Gamma_{xz} \\
\tau_{yz} &= 2G\,\Gamma_{xy}
\end{aligned} \tag{13}$$

where: $\lambda, G\ (shear\ modulus) - Lame's\ parameters.$

Lame's constants, λ and G, can be related to particular elements of the stiffness coefficients matrix by combining equations (12) and (13), which gives identities (14) shown below.

In case of an isotropic medium, Lame's parameters may be replaced with different pair of elastic moduli according to the relationships shown in table 2-1.

$$\begin{aligned} C_{11} &= C_{22} = C_{33} = \lambda + 2G \\ C_{12} &= C_{13} = C_{23} = \lambda \\ C_{44} &= C_{55} = C_{66} = G \end{aligned} \tag{14}$$

Table 2-1. Relationship between elastic moduli for isotropic medium.

Modulus	$\boldsymbol{\lambda}$ & $\boldsymbol{G}$	$\boldsymbol{H}$ & $\boldsymbol{G}$	$\boldsymbol{K}$ & $\boldsymbol{G}$	$\boldsymbol{E}$ & $\boldsymbol{\nu}$
Plane wave modulus H	$\lambda + 2G$	H	$K + \frac{4}{3}G$	$E\frac{1-\nu}{(1+\nu)(1-2\nu)}$
Shear modulus G	G	G	G	$E\frac{1}{2(1+\nu)}$
Bulk modulus K	$\lambda + \frac{2}{3}G$	$H - \frac{4}{3}G$	K	$E\frac{1}{3(1-2\nu)}$
Young's modulus E	$\frac{G(3\lambda+2G)}{\lambda+G}$	$\frac{G(3H-4G)}{H-G}$	$\frac{9KG}{3K+G}$	E
Lamé's coefficient λ	λ	$H - 2G$	$K - \frac{2}{3}G$	$E\frac{\nu}{(1+\nu)(1-2\nu)}$
Poisson's ratio ν	$\frac{\lambda}{2(\lambda+G)}$	$\frac{H-2G}{2(H-G)}$	$\frac{3K-2G}{2(3K-G)}$	ν

Equations (13) indicate that not only the sense of stress and strain vectors, but also the direction do not affect the behaviour of the body. Changes along the direction parallel to the coordinate system axes are governed by both moduli, while angular (shear) deformation depends exclusively on shear modulus of the medium. Small number of parameters required to describe an isotropic body and possibility to substitute them with other moduli make it much easier to use the isotropic model for practical purposes. It may explain the tendency to ignore anisotropic effects in field studies where all necessary parameters are hardly available.

2.2.3. Transverse isotropy

Transverse isotropy is an intermediate case of symmetry, somewhere in between orthorhombic symmetry and isotropy, used to describe a medium containing parallel-

oriented symmetry planes localised along an unique symmetry axis. The difference between the orthorhombic symmetry and transverse isotropy are shown in fig. (2-3).

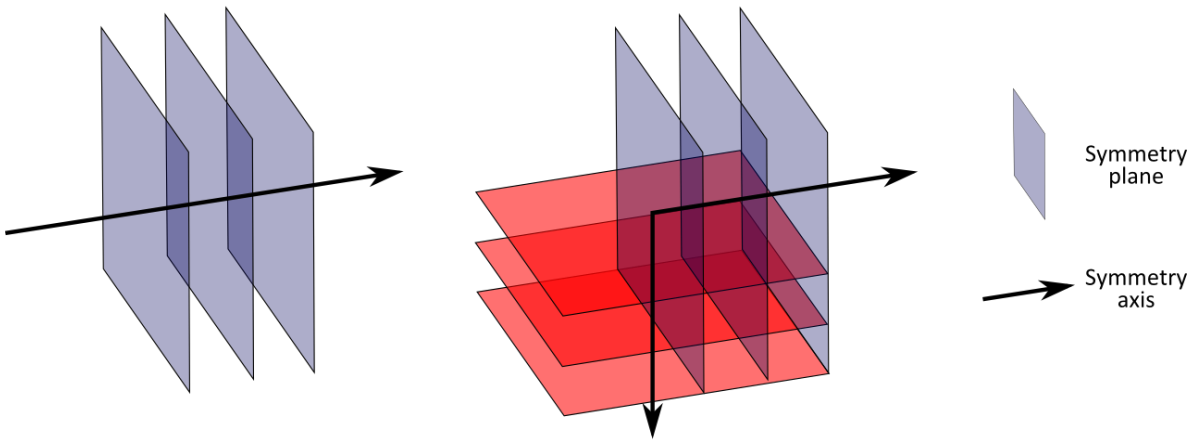

Fig. 2-3. Graphical representation of transverse (left) and orthorhombic (right) symmetries. .

It is assumed that this type of medium is characterised with fully rotational symmetry, and therefore the properties of a *TI* (*Transversely Isotropic*) medium do not change within a symmetry plane, but may vary in any other direction. In order to fulfil these conditions a new set of the stiffness coefficients definitions has to be established (equations 15).

$$\begin{aligned} C_{11} &= C_{22} \\ C_{13} &= C_{23} \\ C_{12} &= C_{11} - 2C_{66} \\ C_{44} &= C_{55} \end{aligned} \tag{15}$$

Transverse isotropy assumes that some of the directions of wave propagation are governed by the same stiffness moduli, as their oscillations occur within the same symmetry planes. This assumption allows to place equality sign between C_{11} and C_{22}, and between C_{44} and C_{55} due to coincidence in the direction and modes of corresponding wave oscillations (the relationship between the elastic stiffness coefficients and the direction and mode of wave propagation will be explained more in detail in the next chapter). Moreover, it allows to simplify other, more complex, elements of the matrix reducing the number of independent constants to five. Applying this relations to the general form of the elastic stiffness coefficients matrix (8) allows to obtain $\boldsymbol{C}$ matrix for TI medium (16).

$$\boldsymbol{C} = \begin{bmatrix} C_{11} & C_{11}-2C_{66} & C_{13} & 0 & 0 & 0 \\ C_{11}-2C_{66} & C_{11} & C_{13} & 0 & 0 & 0 \\ C_{13} & C_{13} & C_{33} & 0 & 0 & 0 \\ 0 & 0 & 0 & C_{44} & 0 & 0 \\ 0 & 0 & 0 & 0 & C_{44} & 0 \\ 0 & 0 & 0 & 0 & 0 & C_{66} \end{bmatrix} \tag{16}$$

TI medium theory may be successfully applied to describe horizontally layered sedimentary rock or stress-induced anisotropy (Zoback, 2007). Combining transverse isotropy with the previously introduced symmetry variants it is possible to develop more complex rock models for layered or/and fractured rocks, as ones presented in fig. (2-4).

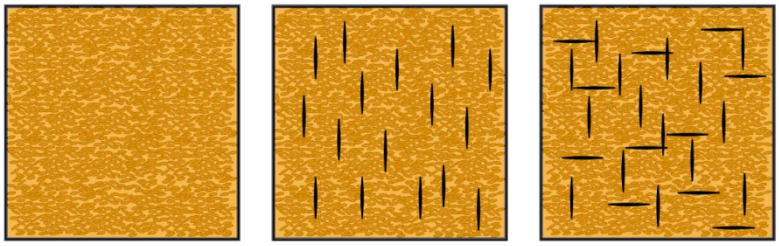

Fig. 2-4. Isotropic (left), transversely isotropic (centre) and orthorhombic (right) rock models.

2.3. Stiffness coefficients and seismic velocities

Seismic wave propagation in an isotropic medium can be described using Lame's coefficients or other pair of moduli, as shown in table 1. For the purposes of giving a typical example of seismic velocities expressed in terms of medium moduli, equations (17) and (18) are introduced:

$$V_P = \sqrt{\frac{K + \frac{4}{3}G}{\rho}} \tag{17}$$

$$V_S = \sqrt{\frac{G}{\rho}} \tag{18}$$

where: $K - bulk\ modulus, \rho - density$.

In the anisotropic case, elastic moduli of a medium can be directly related to the stiffness matrix coefficients C_{ij}, which can be used to approximate seismic wave propagation within given body. The stiffness constants for TI medium can be related to various modes, directions and polarizations of a propagating wave, as described by Bhuiyan and Holt (2016):

- C_{11} – P-wave modulus computed from propagation within the symmetry plane,
- C_{33} – P-wave modulus computed from propagation along the symmetry axis,
- C_{44} – S-wave modulus computed from propagation along the symmetry axis,
- C_{66} – S-wave modulus computed from propagation within the symmetry plane and wave polarization in the symmetry plane.
- C_{13} – constant calculated from quasi P-wave velocities measured at an angle between the symmetry plane and the symmetry axis.

The definitions introduced above describe the elements of the elastic stiffness matrix as a result of wave velocity measurements carried out in the investigated medium, and therefore they can be treated as effective parameters describing all seismic wave propagation-related phenomena. Hence, vertical propagation of P- and S-waves in transversely isotropic medium with horizontally oriented symmetry planes can be expressed in terms of the C_{ij} coefficients, as in equations (19) and (20).

$$V_{P0} = \sqrt{\frac{C_{33}}{\rho}} \tag{19}$$

$$V_{S0} = \sqrt{\frac{C_{44}}{\rho}} \tag{20}$$

2.4. Alternative parametrization of TI medium

In order to complement the list of elements required to alternatively characterise anisotropic medium introduced by Thomsen (1986), containing vertical P- and S-wave velocities expressed in the way presented in equations (19) and (20), it is necessary to define three more dimensionless parameters.

$$\varepsilon = \frac{C_{11} - C_{33}}{2C_{33}} \tag{21}$$

$$\gamma = \frac{C_{66} - C_{44}}{2C_{44}} \tag{22}$$

$$\delta = \frac{(C_{13} + C_{44})^2 - (C_{33} - C_{44})^2}{2C_{33}(C_{33} - C_{44})} \tag{23}$$

Thomsen's parameters $V_{P0}, V_{S0}, \varepsilon, \gamma$ and δ together with density ρ are sufficient to describe the wave propagation within the medium. Dimensionless parameters carry information regarding anisotropy strength and shape of the waterfront. Parameter ε provides quantitative information about the deviation of the P-wave velocity within the symmetry plane in comparison to the P-wave velocity along the symmetry axis. Thomsen's parameter γ carries analogical information for S-wave polarised parallel to the symmetry plane. The above relations are presented in equations (24 a), (24b) and (24c). Parameter δ is related to normal moveout velocities, defining curvature of the wave front and may be used as shown in equation (25a), (25b) and (25c).

$$V_P^2(\theta = 90) = V_{P0}^2(1 + 2\varepsilon) \tag{24a}$$

$$V_{SH}^2(\theta = 90) = V_{S0}^2(1 + 2\gamma) \tag{24b}$$

$$V_{SV}^2(\theta = 90) = V_{S0}^2 \tag{24c}$$

$$V_{P(NMO)}^2 = V_{P0}^2(1 + 2\delta) \tag{25a}$$

$$V_{SV(NMO)}^2 = V_{S0}^2\left(1 + 2\frac{V_{P0}^2}{V_{S0}^2}(\varepsilon - \delta)\right) \tag{25b}$$

$$V_{SH(NMO)}^2 = V_{S0}^2(1 + \gamma) \tag{25c}$$

where: $\theta - angle\ between\ the\ symmetry\ axis\ and\ propagation\ direction,$

$V_{SH} -\ shear\ wave\ polarized\ in\ the\ symmetry\ plane\ surface.$

However, equations (24 a-c) are only a specific case of more general formulations (26 a-c) allowing to compute seismic velocities for any arbitrary angle (Thomsen, 1986).

$$V_P^2(\theta) = V_{P0}^2(1 + \varepsilon \sin^2\theta + D^*(\theta)) \tag{26a}$$

$$V_{SH}^2(\theta) = V_{S0}^2(1 + 2\gamma \sin^2\theta) \tag{26b}$$

$$V_{SV}^2(\theta) = V_{S0}^2\left(1 + \frac{V_{P0}^2}{V_{S0}^2}\varepsilon \sin^2\theta - \frac{V_{P0}^2}{V_{S0}^2}D^*(\theta)\right) \tag{26c}$$

where

$$D^*(\theta) = \frac{1}{2}\left(1 - \frac{V_{S0}^2}{V_{P0}^2}\right)\left\{\left[1 + \frac{4\left(\frac{1}{2C_{33}^2}[2(C_{13}+C_{44})^2 - (C_{33}+C_{44})(C_{11}+C_{33}-2C_{44})]\right)}{\left(1 - \frac{V_{S0}^2}{V_{P0}^2}\right)^2}\sin^2\theta\cos^2\theta + \frac{4\left(1 - \frac{V_{S0}^2}{V_{P0}^2} + \varepsilon\right)\varepsilon}{\left(1 - \frac{V_{S0}^2}{V_{P0}^2}\right)^2}\sin^4\theta\right]^{\frac{1}{2}} - 1\right\}. \tag{27}$$

As they are derived directly from the elastic stiffness matrix, they can be related to the elastic properties of the medium. At the same time it is possible to estimate them by analysing wave fronts registered during field studies which makes them an useful tool in anisotropy studies and quantitative seismic data interpretation, providing a direct link between elastic properties of a medium and observed large-scale data. In the majority of studies Thomsen's parameters of rocks had relatively small values ($\varepsilon, \gamma, \delta \ll 1$), as the discrepancies between seismic velocities in particular directions tend to be rather small. This observation suggests that earth-like media may be treated as an isotropic background with additional slightly pronounced anisotropic effects. The influence of Thomsen's parameters on seismic wave fronts is visualised in fig. (2-5).

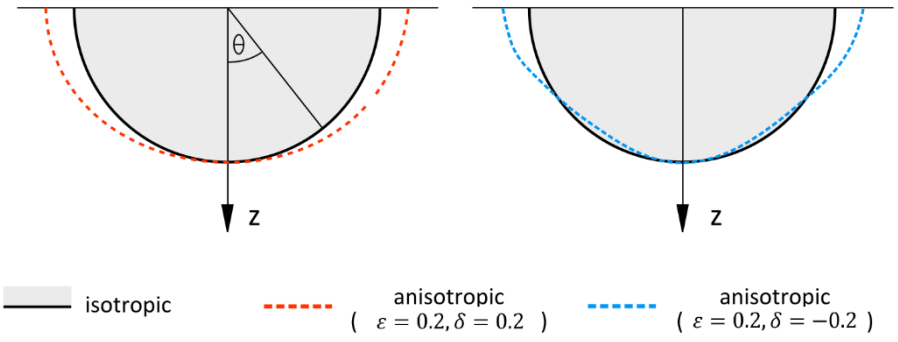

Fig. 2-5. P-wave wave fronts propagating within an anisotropic half-spaces (after Thomsen, 1986).

According to equation (26a) the vertical velocity ($\theta = 0°$) is equal for both, isotropic and anisotropic wavefronts, and discrepancies appear when the angle has a non-zero value. For the intermediate angles, $\theta \in (0,90°)$, where the influence of δ parameter is well pronounced, the differences between the wave fronts are obvious (the parameter δ, although not directly used in the formulas, is actually included in one of the terms of equation 27). As proven by fig. (2-5), different values of the parameters ε and δ cause non-ellipticity of the emanating wavefront. The horizontal velocity ($\theta = 90°$) is the same in both cases, as the horizontal V_P is influenced only by Thomsen's ε.

Due to their versatility, Thomsen's parameters can describe any transversely isotropic medium regardless its spatial scale. They can be used to describe wave propagation within a centimetre-long laboratory sample as well as within a set of field-scale layered sediments. For the purpose of even more intuitive description of the transversely anisotropic medium, the parameters ε and γ can be used to approximate the fractional difference between the vertical and horizontal velocities. In order to achieve that, equation (24a) and (24b) have to be transformed into equation (28). The terms under the root can be approximated using Tylor's expansion giving equations (29), which can be simply transformed into the final forms of the estimates (30).

$$V_P(90°) = V_{P0}\sqrt{1+2\varepsilon}$$
$$V_S(90°) = V_{S0}\sqrt{1+2\gamma} \tag{28}$$

$$V_P(90°) = V_{P0}(1+\varepsilon)$$
$$V_S(90°) = V_{S0}(1+\gamma) \tag{29}$$

$$\varepsilon = \frac{V_P(90°) - V_{P0}}{V_{P0}}$$
$$\gamma = \frac{V_S(90°) - V_{S0}}{V_{S0}} \tag{30}$$

The discrepancies between isotropic and anisotropic wavefronts can be also described using phase and group velocities, introduced in equations (31) and (32), respectively. In an isotropic medium both velocities are equal, and they start to diverge as

soon as any anisotropy is introduced. The discrepancies between the velocities grow with increasing level of anisotropy in the medium. The concept of phase and group velocities is shown in fig. (2-6).

$$V_{phase} = \frac{1}{\sqrt{p^2 + q^2}} \tag{31}$$

$$V_{group} = \sqrt{V_x^2 + V_z^2} \tag{32}$$

where: $p = \frac{\sin(\theta)}{V(\theta)} - horizontal\ slowness, q = \frac{\cos(\theta)}{V(\theta)} - vertical\ slowness,\ V_x\ horizontal\ component\ of\ velocity\ vector, V_z - vertical\ component\ of\ velocity\ vector.$

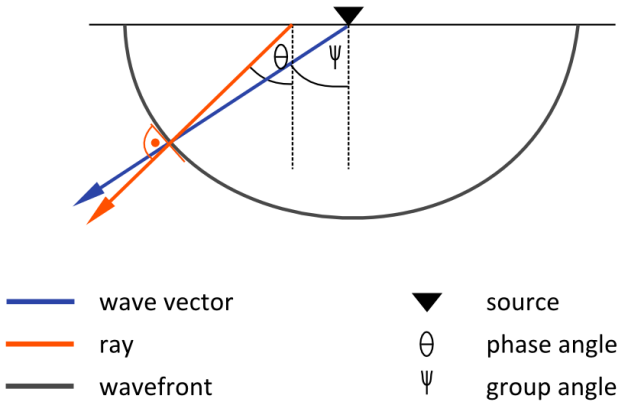

Fig. 2-6. Group and phase velocities and angles (after Thomsen, 1986).

2.5. Thomsen's parameters in orthorhombic medium

Despites their versatility, Thomsen's parameters in their original form do not allow to correctly describe more complex systems with higher number of symmetry axes and symmetry planes than transversely isotropic medium (e.g. layered medium with a set of cracks perpendicular to the layering). In order to apply Thomsen's parametrization to more complex symmetries, it is necessary to adjust the definition of the parameters. To rearticulate Thomsen's equations, a new coordinate system has to be oriented according to the symmetry planes in the medium, as shown in fig. (2-7). In the presented example,

x_3 is the symmetry axis for layering in the medium, meanwhile x_1 axis is parallel to crack normal vectors, resembling the situation presented in fig. (2-3)

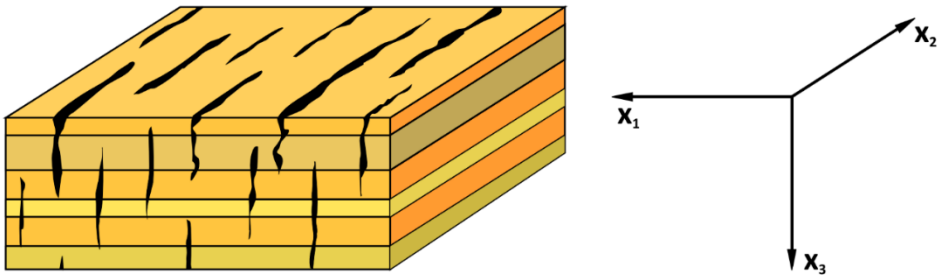

Fig. 2-7. Orthorhombic model of layered medium with a set of cracks perpendicular to the layering (after Tsvankin, 1997).

For this kind of medium not all of the identities presented in equations (15) are still valid, as changes in the medium parameters are no longer related to a unique symmetry axis and may be varying along other directions. The stiffness matrix coefficient C_{44} does not equal C_{55} – in the orthorhombic medium these coefficients stand for S-wave moduli for propagation along x_3 symmetry axis and polarised in $[x_2, x_3]$ and $[x_1, x_3]$ planes, respectively. Accordingly, the seismic velocities and Thomsen's parameters for waves propagating along x_3 axis and S-wave oscillating within the $[x_1, x_3]$ symmetry plane were expressed by Tsvankin (1997), here in equations (33-37). The parameters indices refer to x_2 axis, normal to the chosen polarisation plane.

$$V_{P0} = \sqrt{\frac{C_{33}}{\rho}} \tag{33}$$

$$V_S^{(2)} = \sqrt{\frac{C_{55}}{\rho}} \tag{34}$$

$$\varepsilon^{(2)} = \frac{C_{11} - C_{33}}{2C_{33}} \tag{35}$$

$$\gamma^{(2)} = \frac{C_{66} - C_{44}}{2C_{44}} \tag{36}$$

$$\delta^{(2)} = \frac{(C_{13} + C_{55})^2 - (C_{33} - C_{55})^2}{2C_{33}(C_{33} - C_{55})} \tag{37}$$

In the case of shear waves polarised in $[x_2, x_3]$ plane, parallelly to x_1 axis, Thomsen's parameters are defined by equations (38-41) using different set of the elastic stiffness matrix coefficients. Vertical velocities V_P and $V_S^{(2)}$ and six new parameters can replace the stiffness matrix coefficients $C_{11}, C_{22}, C_{33}, C_{44}, C_{55}, C_{66}, C_{23}$ and C_{13}, and be used instead of them to describe anisotropy of the medium. .

$$V_S^{(1)} = \sqrt{\frac{C_{44}}{\rho}} \tag{38}$$

$$\varepsilon^{(1)} = \frac{C_{22} - C_{33}}{2C_{33}} \tag{39}$$

$$\gamma^{(1)} = \frac{C_{66} - C_{55}}{2C_{55}} \tag{40}$$

$$\delta^{(1)} = \frac{(C_{23} + C_{44})^2 - (C_{33} - C_{44})^2}{2C_{33}(C_{33} - C_{44})} \tag{41}$$

In order to substitute coefficient C_{12} and to complete the list of parameter necessary to fully characterise the orthorhombic media, $\delta^{(3)}$ has to be defined. This anisotropy parameter is responsible for waves polarised in $[x_1, x_2]$ plane.

$$\delta^{(3)} = \frac{(C_{12} + C_{66})^2 - (C_{11} - C_{66})^2}{2C_{11}(C_{11} - C_{66})} \tag{42}$$

Due to the introduction of yet another shear wave modulus C_{55}, the vertical velocity of S-wave depends not only on the direction of propagation but also its polarisation, and therefore there may be two separate S-waves observed in the propagation records. This phenomena is often referred to as *shear wave splitting*, and has been observed many times in experimental data. The discrepancies in velocities between the two S-waves can be describe in the same way as it was previously done for horizontal and vertical propagation in transversely isotropic medium in one of equations (30). The velocities divergence was approximated in equation (43).

$$\gamma^{(S)} = \frac{C_{44} - C_{55}}{2C_{55}} = \frac{\gamma^{(1)} - \gamma^{(2)}}{1 + 2\gamma^{(2)}} \approx \frac{V_S^{(1)} - V_S^{(2)}}{V_S^{(2)}} \tag{43}$$

3. Rock models

Changing stress field is one of the most prominent factors affecting seismic velocities in rocks, also having an effect on their internal structure and volume. Comparable changes may be caused by pore fluid substitution and temperature variations. The most important mechanisms responsible for the rock stiffness stress-dependence are porosity change, grain contacts alteration and closure or generation of cracks (Adams and Williamson, 1923). The two last factors are commonly used as a starting point for rock models formulation. Grain contacts-based models are based on scaling of the influence of changes of an individual contact zone on the entire rock volume. Crack closure analysis is a basis for inclusion approach, in which the rock volume is treated as a solid medium with inclusions or voids affecting its elastic properties. Porosity changes may be also introduced as an additional parameter to both classes of models.

3.1. Granular approach

In the granular approach the rock is considered to be a set of interacting grains, responding to changes in the stress field and consequently affecting the effective elastic properties of the medium. Force applied to the system causes deformation of the grains and elastic, as well as geometrical, changes of their contact zones. One of the first attempts to describe this mechanism was made by Hertz (1882), who analysed interactions between two identical spherical grains, as presented in fig. (3-1).

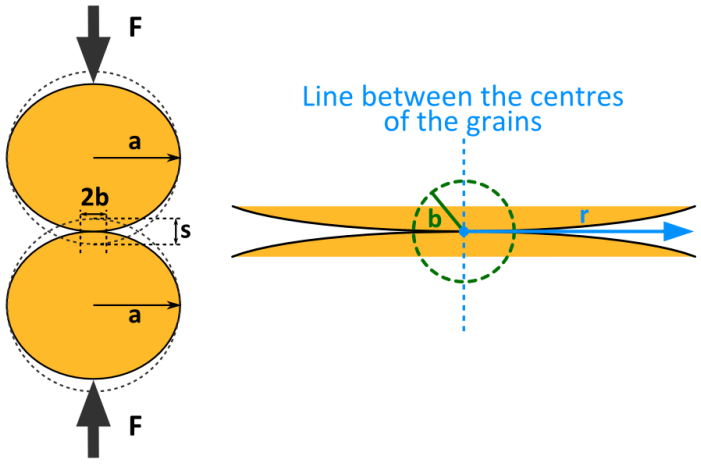

Fig. 3-1. Spherical grains contact..

Hertz assumed that the grains are linearly elastic and that the contact zone between the grains b is relatively small in comparison to the grains radii a and its surface is changing under the influence of applied force F, as shown in equation (44). As a consequence of grains deformation, the distance between the centres of granules s is also changing. The amplitude of both geometrical changes are somehow proportional to the elastic moduli of the solid, i.e. Young's modulus E_s and Poisson's ratio v_s. Finally, changes in the force applied to the grains imply alteration of the normal stress along the contact surface σ according to equation (46). This equation indicates that stress distribution is a function of the exerted force and the contact area, which is consistent with the general stress definition.

$$b = \left(\frac{3(1-v_s^2)aF}{4E_s}\right)^{\frac{1}{3}} \tag{44}$$

$$s = \left(\frac{9(1-v_s^2)^2F^2}{2E_s^2a}\right)^{\frac{1}{3}} \tag{45}$$

$$\sigma = \frac{3F}{2\pi b^2}\left(1-\frac{r^2}{b^2}\right)^{\frac{1}{2}} \tag{46}$$

where: $r - lateral\ distance\ from\ the\ line\ between\ the\ centres\ of\ the\ grains.$

Proportionality between the increment of force ΔF and the advancing deformation Δs can be also expressed by an individual force coefficient D_n. Mindlin (1949) extended Hertz's theory by introducing terms responsible for shear force F', lateral displacement s' and shear force coefficient D_t. This allowed to involve lateral deformations and movements in the contact zone, a behaviour frequently observed in complex systems consisting of larger number of interacting elements, and therefore made so-called Hertz-Mindlin's theory more suitable for description of rock-like media. Both coefficients in their simplest forms depend on shear modulus G_s, Poisson's ratio v_s and contact radius b exposing the importance of the lateral deformations for the effective elastic properties of the medium. Young's modulus E_s was substituted with shear modulus G_s according to the relationships shown in table 1.

$$D_n = \frac{\Delta F}{\Delta s} = \left(\frac{3E_s^2aF}{4(1-v_s^2)^2}\right)^{\frac{1}{3}} = \frac{2G_sb}{1-v_s} \tag{47}$$

$$D_t = \frac{\Delta F'}{\Delta s'} = \frac{[6E_s^2 aF(1-v_s^2)^2]^{\frac{1}{3}}}{(2-v_s)(1+v_s)} = \frac{4G_s b}{2-v_s} \tag{48}$$

It is worth noting that the normal and the shear stress distributions along the contact surface differ significantly, both in their functions complexity and locations of maximum concentration. Stress functions are shown in fig. (3-2).

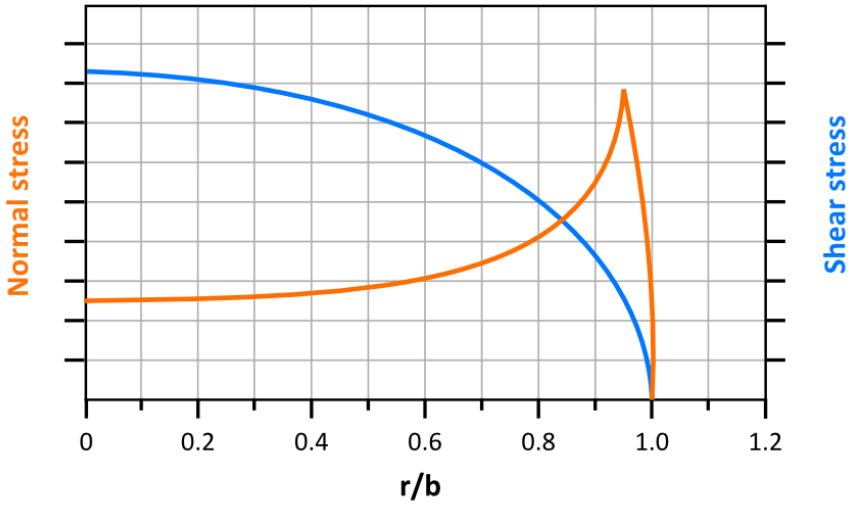

Fig. 3-2. Stress distribution along the sphere contact surface (after White, 1983).

To transform the equations into a more practical form, the relation between the confining force F and the initial external pressure σ_p was established. The proportionality between these quantities depends on the external surface of the spheres, coordination number N_c (being the average number of contacts per sphere) and porosity ϕ, which carry a significant piece of information about the internal structure of the medium.

$$F = \frac{4\pi a^2 \sigma_P}{N_c(1-\phi)} \tag{49}$$

Finally, Digby (1981) introduced the relationship between the external stress exerted on the grains contacts and bulk and shear moduli, K and G respectively. It was assumed that grains are randomly packed and that there is no slip on the grain contacts. Digby's model is expressed by equations (50) and (51).

$$K = \frac{\partial \sigma_P}{\partial \varepsilon_{vol}} = \frac{N_c(1-\phi)}{6\pi a} D_n = \left[\frac{N_c^2(1-\phi)^2 G_s^2 \sigma_P}{18\pi^2(1-v_s)^2}\right]^{\frac{1}{3}} \tag{50}$$

$$G = \frac{N_c(1-\phi)}{10\pi a}\left(D_n + \frac{3}{2}D_t\right) = \frac{5-4v_s}{5(2-v_s)}\left[\frac{3N_c^2(1-\phi)^2 G_s^2 \sigma_P}{2\pi^2(1-v_s)^2}\right]^{\frac{1}{3}} \tag{51}$$

where: $\varepsilon_{vol} = \frac{3s}{2a} - volumetric\ strain.$

Walton (1987) developed the theory by taking into consideration the influence of possible slip on the contact grains, implying that the friction between the grains, governed by the friction coefficient, has an impact on the elastic moduli of the medium. Walton's model is expressed by equation (52-54).

$$K = \frac{1}{6}\left[\frac{3N_c^2(1-\phi)^2 \sigma_P}{\pi^4 B^2}\right]^{\frac{1}{3}} \tag{52}$$

$$G = \frac{1}{10}\left[\frac{3N_c^2(1-\phi)^2 \sigma_P}{\pi^4 B^2}\right]^{\frac{1}{3}} = \frac{3}{5}K \tag{53}$$

$$B = \frac{3}{2\pi}\frac{(1-2v_s)(1-v_s)}{E_s} \tag{54}$$

The link between the external stress σ and the elastic moduli of the medium, combined with equation for velocities (17) and (18), makes it possible to investigate the influence of stress on seismic waves propagation in a rock-like medium.

However, the stress dependency of the elastic moduli is a complex phenomenon and may be affected by various factor which are not directly covered by Walton's theory. Grain shape, rotation and rearrangement, uneven stress distribution within a grain assembly, fluid saturation and cementing of the grain contacts may have a significant impact on the effective properties of the medium (Makse et al., 2001). In order to include those factors, some of the parameters of the model may be changed – in Walton's theory the power n of the confining stress was assumed to be $n = 1/3$, but its value can be shifted to adjust the model to a particular system. Moreover, at high effective stresses partial grain

plasticisation may occur, causing additional discrepancies between the predictions of the model and the experimental data. Unequal grain radiuses and partial slipping on the grain contacts were addressed by Bachrach and Avseth (2008), who introduced additional parameters for effective contact radii and volume fraction of slip and non-slip contacts. Finally, Norris and Johnson (1997) rederived the expressions for the elastic moduli using various energy density functions for different contact types in order to introduce stress path dependency into the granular media models, and proved that stress sensitivity of the system also depends on the loading path.

3.2. Inclusion approach

In the alternative approach, the medium is considered as a solid containing various inclusions or voids. For small concentration of inclusions ξ_{incl} it is assumed that there is no interaction between them. Therefore, the effective elastic moduli of the medium (K^* and G^*) can be assumed to be the result of perturbation of the solid material moduli (K_s and G_s) proportional to the concentration of inclusions. The relationship between the solid medium and the effective moduli is captured by equations (55) taken from Fjær et al. (2008).

$$K^* = K_s(1 - Q_K\xi_{incl})$$
$$G^* = G_s(1 - Q_G\xi_{incl}) \tag{55}$$

where: $Q_{K,G} - measure\ of\ impact\ of\ inclusions\ on\ effective\ moduli.$

Assuming positive values of the parameter Q_K and Q_G, it could be concluded that the presence of voids causes drop of the effective elastic moduli value. The amplitude of the decrease depends on the impact factor itself and the inclusions concentration.

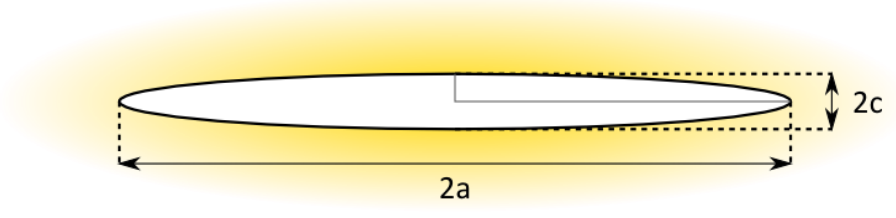

Fig. 3-3. Crack geometry.

If the voids are assumed to be of form of thin and flat cracks, they can be described with additional terms containing information about their shape and distribution in the medium. For the purpose of simplicity, disc-like cracks, shown in two dimension in fig. (3-3), are described with the aspect ratio α and the crack density parameter ξ.

$$\alpha = \frac{c}{a} \tag{56}$$

$$\xi = \frac{N}{V} < a^3 > \tag{57}$$

where: $c - crack\ thickness,\ a - \ diameter,\ <>\ - average\ over\ all\ cracks,$

$N - number\ of\ cracks, V - volume.$

The aspect ratio α, being a dimensionless parameter, captures only the proportion between the dimensions of cracks. The crack density parameter ξ approximates the number of cracks per unit volume and contains averaged information about their diameter. Carrying information about both cracks geometry and distribution makes the density parameter ξ suitable to be used as a concentration factor in more complex inclusion models.

3.2.1. Random crack distribution

Budiansky and O'Connell (1976) assumed random orientation of cracks and managed to expand the general equations (55) into more precise formulations. The model proposed by the mentioned authors involves the crack density parameter ξ,the elastic moduli and the Poisson's ratio of the solid (K_s, G_s and v_s, respectively) and the drainage parameter D.

$$K^* = K_s\left(1 - \frac{16}{9}\frac{1 - v_s^2}{1 - 2v_s}D\xi\right) \tag{58}$$

$$G^* = G_s\left(1 - \frac{32}{45}(1 - v_s)\left[D + \frac{3}{2 - v_s}\right]\xi\right) \tag{59}$$

$$\frac{1}{D} = 1 + \frac{4}{3\pi\alpha}\frac{1 - v_s^2}{1 - 2v_s}\frac{K_f}{K_s} \tag{60}$$

where: $K_f - fluid\ bulk\ modulus, D - drainage\ parameter.$

The drainage parameter D, giving an insight into the properties of the fluid filling the cracks, can vary greatly not only with type of fluid, but also with saturation. For dry rocks, i.e. $K_f = 0$, the parameter reduces to $D = 1$. In case of fully-saturated thin cracks, fulfilling the relationship $\alpha \ll K_f/K_s$, the parameter D approaches 0, decreasing dramatically the compliance of the cracks. The relationship between the moduli and the aspect ratio of the cracks excludes cases of highly compressible fluids filling the voids. However, aspect ratio does not affect the effective moduli in any of both situations (Mavko and Nur, 1978). Analysis of the impact of the drainage parameter D, i.e. saturation, on the elastic moduli is presented in fig. (3-4). The results of this simple modelling suggest that for dry fractured rocks even small values of stress may result in much higher strain amplitudes than for the stresses in a medium without cracks. Moreover, presence of any fluid in the cracks causes counteraction against the deformation of the medium, consequently increasing the effective moduli. The dependence between the fluid bulk modulus K_f and the effective moduli is not linear – the biggest changes of the effective moduli are observed for low fluid modulus values suggesting strong influence of gas on the effective rock stiffness. The relationship between the effective shear modulus G^* and saturation is much less intuitive than in the case of the effective bulk modulus K^*. The dependence of these two parameters comes from the deformation of insulated cracks induced by shear stress and influenced by the fluid bulk modulus. In this conditions any kind of deformation is a result of interplay between the solid and the cracks, and hence it is sensitive to the impact of compressibility of the crack-filling fluid.

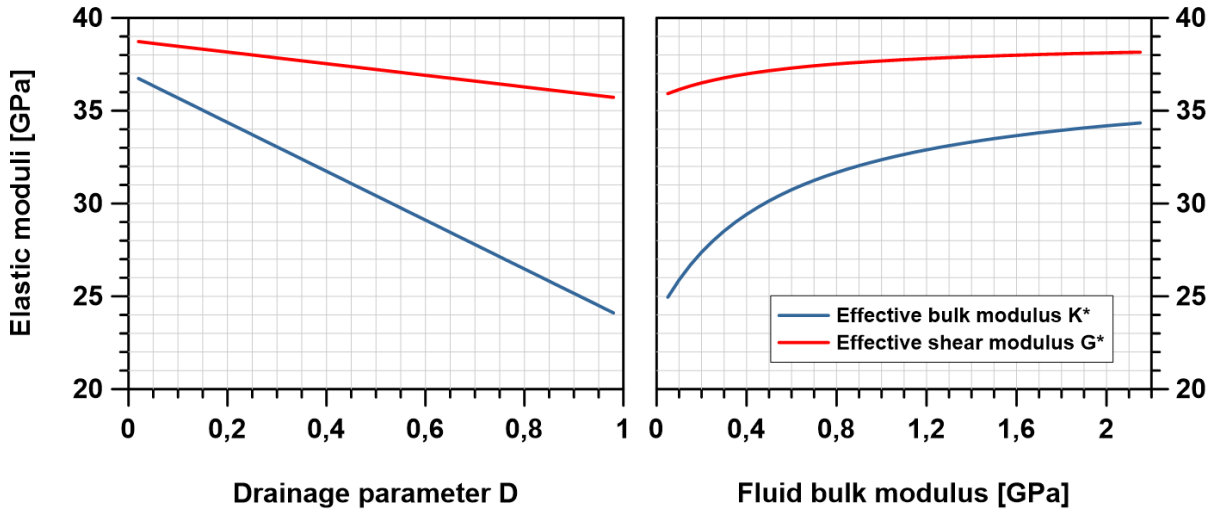

Fig. 3-4. Effective moduli modelling ($K_s = 37\ GPa, G_s = 44\ GPa, \nu_s = 0.2, \alpha = 0.01, \xi = 0.125$)

To maintain consistency between the inclusion approach and Biot's theory, it is recommended to compute the effective moduli for dry rock ($D = 1$) and add the saturation effects using Biot's theory afterwards. This approach is proved to provide more accurate effective moduli approximations, especially in the low frequency limit, when the fluid has enough time to equilibrate (Fjær et al., 2008).

3.2.2. Sets of parallel cracks

The orientation of cracks in subsurface is highly correlated with the anisotropy of stress field, and therefore is hardly ever random. Cracks spatial arrangement is subjected to the principle stresses - their planes are usually observed to be perpendicular or subperpendicular to the minimum principle stress direction, and consequently parallel or subparallel to the maximum principle stress (Crampin, 1990).

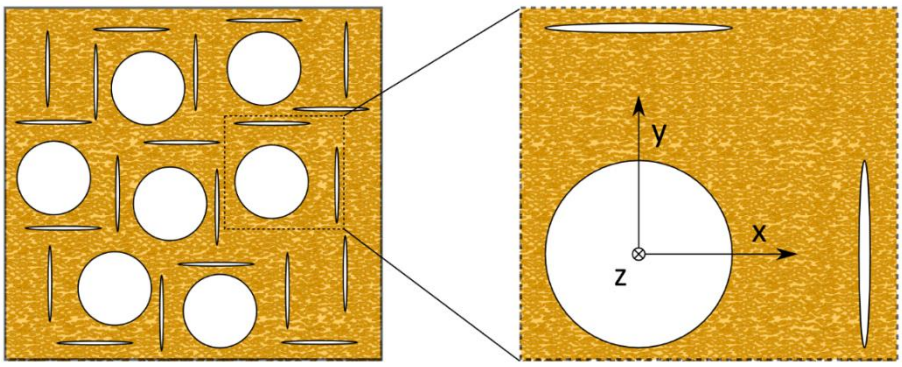

Fig. 3-5. Sets of perpendicular cracks (after Fjær, 2006).

In case of preferential direction of cracks opening it is more convenient to use stiffness coefficients instead of bulk moduli of the rock. Equation (61) shows the general form of the effective stiffness coefficient C_{ij}^{*}. When there is more than one set of cracks, the crack density parameter ξ and the crack impact factor Q should be defined separately for each of them, which transforms the general form into equation (62).

$$C_{ij}^{*} = C_{ij}^{0}(1 - Q_{ij}\xi) \tag{61}$$

$$C_{ij}^{*} = C_{ij}^{0}(1 - Q_{ij}^{(1)}\,\xi^{(1)} - Q_{ij}^{(2)}\,\xi^{(2)} - \dots) \tag{62}$$

where: $C_{ij}^{0} - stiffness\ coeficients\ of\ the\ unfractured\ material,\ Q_{ij}^{(k)}, \xi^{(k)} - parameters\ for\ k\ set\ of\ cracks.$

This model can be further refined and adjusted to particular situations. Fjær (2006) assumed the coexistence of pores and three sets of non-interacting penny-shaped fractures, as shown in fig. (3-5), and obtained a set of equations (63) for stiffness coefficients of an anisotropic medium.

$$
\begin{aligned}
C_{11}^{*} &= C_{11}^{0}\left(1 - Q_{11}^{(P)}\phi - Q_{33}\,\xi_x - Q_{11}(\xi_y + \xi_z)\right)\\
C_{22}^{*} &= C_{22}^{0}\left(1 - Q_{11}^{(P)}\phi - Q_{33}\,\xi_y - Q_{11}(\xi_z + \xi_x)\right)\\
C_{33}^{*} &= C_{33}^{0}\left(1 - Q_{33}^{(P)}\phi - Q_{33}\,\xi_z - Q_{11}(\xi_x + \xi_y)\right)\\
C_{12}^{*} &= C_{12}^{0}\left(1 - Q_{13}^{(P)}\phi - Q_{13}(\xi_x + \xi_y) - Q_{12}\,\xi_z\right)\\
C_{13}^{*} &= C_{13}^{0}\left(1 - Q_{13}^{(P)}\phi - Q_{13}(\xi_z + \xi_x) - Q_{12}\,\xi_y\right)\\
C_{23}^{*} &= C_{23}^{0}\left(1 - Q_{13}^{(P)}\phi - Q_{13}(\xi_y + \xi_z) - Q_{12}\,\xi_x\right)\\
C_{44}^{*} &= C_{44}^{0}\left(1 - Q_{44}^{(P)}\phi - Q_{44}(\xi_y + \xi_z) - Q_{66}\,\xi_x\right)\\
C_{55}^{*} &= C_{55}^{0}\left(1 - Q_{44}^{(P)}\phi - Q_{44}(\xi_z + \xi_x) - Q_{66}\,\xi_z\right)\\
C_{66}^{*} &= C_{66}^{0}\left(1 - Q_{66}^{(P)}\phi - Q_{44}(\xi_x + \xi_y) - Q_{66}\,\xi_z\right)
\end{aligned}
\tag{63}
$$

Each of the effective stiffness coefficients has its corresponding set of Q_{ij} impact factors, linking the effective moduli with the crack densities. In this particular model, the effective stiffness coefficients are not only affected by the presence of cracks, but also by the porosity of the medium ϕ, influence of which is given by the Q_{ij}^{P} impact factors. In case of no intrinsic anisotropy some of the stiffness coefficients can be expressed with the uniaxial compaction modulus H_0 and the shear modulus G_0, as shown in equations (64).

$$
\begin{aligned}
C_{11}^{0} &= C_{22}^{0} = C_{33}^{0} = H_0\\
C_{44}^{0} &= C_{55}^{0} = C_{66}^{0} = G_0\\
C_{66}^{0} &= C_{13}^{0} = C_{23}^{0} = H_0 - 2G_0
\end{aligned}
\tag{64}
$$

Hudson (1981) defined the impact coefficients Q using equations (65) and (66). For both groups of Q factors, the crack- and the porosity-related, Poisson's ratio v_s is the most prominent medium parameter influencing their values. Some of the crack-related impact factors (i.e. Q_{11}, Q_{33} and Q_{12}) are also influenced by the drainage parameter D, and therefore are also dependent to the saturation and the properties of the fluid, meanwhile the rest (including all of the porosity-related factors) depends only on properties of the solid fraction.

$$
\begin{aligned}
Q_{11} &= \frac{16}{3}\frac{v_s^2}{1-2v_s}D \\
Q_{33} = Q_{13} &= \frac{16}{3}\frac{(1-v_s)^2}{1-2v_s}D \\
Q_{12} &= \frac{16}{3}\frac{v_s(1-v_s)}{1-2v_s}D \\
Q_{44} &= \frac{16}{3}\frac{1-v_s}{2-v_s} \\
Q_{66} &= 0
\end{aligned}
\tag{65}
$$

$$
\begin{aligned}
Q_{11}^P = Q_{33}^P &= \frac{1}{2}\left(\frac{1+v_s}{1-2v_s} + 10\frac{1-2v_s}{7-5v_s}\right) \\
Q_{13}^P &= \frac{1-v_s}{2v_s}\left(\frac{1+v_s}{1-2v_s} - 10\frac{1-2v_s}{7-5v_s}\right) \\
Q_{44}^P = Q_{66}^P &= 15\frac{1-v_s}{7-5v_s}
\end{aligned}
\tag{66}
$$

In order to insert stress dependence into the model, the crack densities are expressed in terms of stresses and strains, as shown in equations (67). The influence of the rock composition and characteristics is directly expressed with the parameter somehow related to tensile strength T_0. The influence of normal stresses, shear stress and strains on cracks can be individually moderated using additional model parameters n, β and η. Model parameter n controls the influence of the normal stresses. Parameter β governs the influence of the shear deformation and η indicates the stress sensitivity of the cracks.

$$\xi_x = \xi_x^0 \left(\frac{\sigma_x^0 + T_0}{\sigma_x + T_0}\right)^n e^{-\beta(2\varepsilon_x - \varepsilon_y - \varepsilon_z) + \eta\Gamma^2}$$

$$\xi_y = \xi_y^0 \left(\frac{\sigma_y^0 + T_0}{\sigma_y + T_0}\right)^n e^{-\beta(2\varepsilon_y - \varepsilon_x - \varepsilon_z) + \eta\Gamma^2} \quad (67)$$

$$\xi_z = \xi_z^0 \left(\frac{\sigma_z^0 + T_0}{\sigma_z + T_0}\right)^n e^{-\beta(2\varepsilon_z - \varepsilon_y - \varepsilon_x) + \eta\Gamma^2}$$

where: $\xi_i^0 - initial\ crack\ density\ \left(at\ stress\ \sigma_i^0\ and\ strains\ \varepsilon_x = \varepsilon_y = \varepsilon_z = 0\right)$,
$\beta\ and\ \eta - exponents\ related\ to\ local\ failure\ from\ shearing$,
$n - notmal\ stress - related\ exponent$.

Cracks creation and opening, usually linked with the tensile strength of the rock, is affected by both normal and shear stresses due to the mechanisms presented in fig. (3-6).

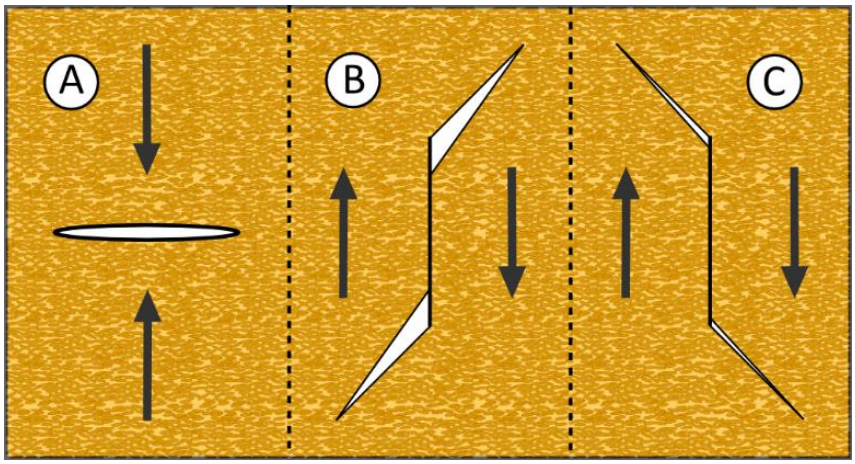

Fig. 3-6. Normal and shear stress effects on cracks: A - crack closure due to normal stress, B - cracks opening associated with shear deformation, C - crack closure associated with shear deformation (after Fjær, 2006).

Fjær (2006) expressed the modelling results in terms of velocities and strains, as there is a direct link between the displacement of particles and the alterations of cracks affecting the seismic velocities values. Stress values were presented as an additional piece of information to explain the causes of resultant deformations. In order to obtain the velocities of elastic waves it is necessary to implement the effective stiffness coefficients into equations (19) and (20) taking into account the direction of propagation in relation to the symmetry axes and planes.

According to Sayers and Kachanov (1996) anisotropy of the fractured rock can be expressed in terms of second and forth degree crack density tensor providing reasonable fit with experimental data. However, this approach will not be discussed in more detail, as no new elements introduced by the authors will be covered in the practical part of the thesis.

3.3. Macroscopic approach

An anisotropic medium can be also described with macroscopic models, which do not differentiate between the influence of particular components of the medium, but rather assign effective parameters to the entire rock volume. In order to describe an anisotropic medium with stress-dependent stiffness coefficients, it is necessary to use non-linear elasticity, where the relation between the effective stiffness coefficients and stress is expressed with the use of third-order elastic constants (Thurston, 1974). One of the experimentally verified models was introduced by Prioul et al. (2004). The Authors assumed that the deformation of the rock caused by a static external stress, characterised by relatively high strains, is governed by the non-linear components of the stiffness coefficients matrix. However, the deformations resulting from wave propagation, usually causing much smaller strains, are linearized, as in the standard elastic theory. Another assumption is that the third-order tensor is implicitly isotropic, and therefore it can be expressed with three independent stiffness coefficients, i.e. c_{111}, c_{112} and c_{123}, and their linear combinations c_{144} and c_{155} constant within defined stress range.

$$c_{144} = \frac{c_{112} - c_{123}}{2}$$
$$c_{155} = \frac{c_{111} - c_{112}}{4} \tag{68}$$

According to Prioul and Lebrat (2004) the constrains of the third-order stiffness tensor (assuming that compression is expressed with positive values of stress and strain) assuring that P- and S-waves are affected mostly by the stress changes in the directions of their propagation and polarization are:

$$c_{111} > c_{112} > c_{123}$$
$$c_{155} > c_{144} \quad \text{and} \quad c_{155} > 0 \tag{69}$$

The effective elastic constants for VTI medium expressed in terms of nonlinear elasticity were defined by Thurston (1974) and Sinha and Kostek (1996) with equations (70).

$$
\begin{aligned}
C_{1111} &= C_{11}^{0}(1+2\varepsilon_{11}) + \sigma_{11} + c_{111}\varepsilon_{11} + c_{112}(\varepsilon_{22}+\varepsilon_{33}) \\
C_{2222} &= C_{11}^{0}(1+2\varepsilon_{22}) + \sigma_{22} + c_{111}\varepsilon_{22} + c_{112}(\varepsilon_{11}+\varepsilon_{33}) \\
C_{3333} &= C_{33}^{0}(1+2\varepsilon_{33}) + \sigma_{33} + c_{111}\varepsilon_{33} + c_{112}(\varepsilon_{11}+\varepsilon_{22}) \\
C_{1122} &= C_{2211} = C_{12}^{0}(1+\varepsilon_{11}+\varepsilon_{22}) + c_{112}(\varepsilon_{11}+\varepsilon_{22}) + c_{123}\varepsilon_{33} \\
C_{1133} &= C_{3311} = C_{13}^{0}(1+\varepsilon_{11}+\varepsilon_{33}) + c_{112}(\varepsilon_{11}+\varepsilon_{33}) + c_{123}\varepsilon_{22} \\
C_{2233} &= C_{3322} = C_{13}^{0}(1+\varepsilon_{22}+\varepsilon_{33}) + c_{112}(\varepsilon_{22}+\varepsilon_{33}) + c_{123}\varepsilon_{11} \\
C_{1212} &= C_{66}^{0}(1+2\varepsilon_{22}) + \sigma_{11} + c_{144}\varepsilon_{33} + c_{155}(\varepsilon_{11}+\varepsilon_{22}) \\
C_{2121} &= C_{66}^{0}(1+2\varepsilon_{11}) + \sigma_{22} + c_{144}\varepsilon_{33} + c_{155}(\varepsilon_{11}+\varepsilon_{22}) \\
C_{1221} &= C_{2112} = C_{66}^{0}(1+\varepsilon_{11}+\varepsilon_{22}) + c_{144}\varepsilon_{33} + c_{155}(\varepsilon_{22}+\varepsilon_{33}) \\
C_{1313} &= C_{44}^{0}(1+2\varepsilon_{33}) + \sigma_{11} + c_{144}\varepsilon_{22} + c_{155}(\varepsilon_{11}+\varepsilon_{33}) \\
C_{3131} &= C_{44}^{0}(1+2\varepsilon_{11}) + \sigma_{33} + c_{144}\varepsilon_{22} + c_{155}(\varepsilon_{11}+\varepsilon_{33}) \\
C_{1331} &= C_{3113} = C_{44}^{0}(1+\varepsilon_{11}+\varepsilon_{33}) + c_{144}\varepsilon_{22} + c_{155}(\varepsilon_{11}+\varepsilon_{33}) \\
C_{2323} &= C_{44}^{0}(1+2\varepsilon_{33}) + \sigma_{22} + c_{144}\varepsilon_{11} + c_{155}(\varepsilon_{22}+\varepsilon_{33}) \\
C_{3232} &= C_{44}^{0}(1+2\varepsilon_{22}) + \sigma_{33} + c_{144}\varepsilon_{11} + c_{155}(\varepsilon_{22}+\varepsilon_{33}) \\
C_{1331} &= C_{3113} = C_{44}^{0}(1+\varepsilon_{22}+\varepsilon_{33}) + c_{144}\varepsilon_{11} + c_{155}(\varepsilon_{22}+\varepsilon_{33})
\end{aligned}
\tag{70}
$$

Distinctive lack of symmetry between elements C_{ijkl} and C_{jikl}, C_{ijlk} and C_{jilk} is caused by the presence of terms $C_{ij}^{0}\varepsilon_{kl}$ and σ_{mn}, indicating that the described system is not exactly equal to a typical transversely isotropic medium. These terms are usually very small in comparison to the rest of terms C_{ij}^{0} and $c_{ijk}\varepsilon_{mn}$ (Prioul et al., 2004), changing the effective moduli values by no more than 0.1% (Thurston, 1974 and Rasolofosaon, 2006). Their impact is much below the accuracy of the method, and therefore can be neglected. This simplification allows to

restore typical symmetry of stiffness coefficients and rewrite equations (70) using Voigt notation.

$$
\begin{aligned}
C_{11} &\approx C_{11}^0 + c_{111}\varepsilon_{11} + c_{112}(\varepsilon_{22} + \varepsilon_{33}) \\
C_{22} &\approx C_{11}^0 + c_{111}\varepsilon_{22} + c_{112}(\varepsilon_{11} + \varepsilon_{33}) \\
C_{33} &\approx C_{33}^0 + c_{111}\varepsilon_{33} + c_{112}(\varepsilon_{11} + \varepsilon_{22}) \\
C_{12} &\approx C_{12}^0 + c_{112}(\varepsilon_{11} + \varepsilon_{22}) + c_{123}\varepsilon_{33} \\
C_{13} &\approx C_{13}^0 + c_{112}(\varepsilon_{11} + \varepsilon_{33}) + c_{123}\varepsilon_{22} \\
C_{23} &\approx C_{13}^0 + c_{112}(\varepsilon_{22} + \varepsilon_{33}) + c_{123}\varepsilon_{11} \\
C_{44} &\approx C_{44}^0 + c_{144}\varepsilon_{11} + c_{155}(\varepsilon_{22} + \varepsilon_{33}) \\
C_{55} &\approx C_{44}^0 + c_{144}\varepsilon_{22} + c_{155}(\varepsilon_{11} + \varepsilon_{33}) \\
C_{66} &\approx C_{66}^0 + c_{144}\varepsilon_{33} + c_{155}(\varepsilon_{11} + \varepsilon_{22})
\end{aligned}
\tag{71}
$$

Stiffness coefficients C_{11}^0, C_{33}^0, C_{44}^0, C_{66}^0 and C_{13}^0 are used to describe a VTI medium in the absence of stress. With the assumption of constant c_{ijk} values within specified stress ranges, it is possible to exchange C_{ij}^0 with stiffness coefficients measured in well-defined reference point C_{ij}^R, and ε_{kl} with $\Delta\varepsilon_{kl} = \varepsilon_{kl} - \varepsilon_{kl}^R$. The impact of the external stress is included by adding terms consisting of third-order parameters (defined for the unstressed or the reference stress state) and strains, being related to stresses via Hook's law. The third-order constants are assumed to be sufficient to completely describe anisotropic response of a medium, even though they are not directly related to an individual phenomena or type of medium components interaction responsible for stiffening (or weakening) of a rock. The most significant feature of this rock model is the linearity of change of the stiffness coefficients with changing stress. One of the results of the described assumptions is that C_{ij} under increasing hydrostatic stress would be represented by a straight line, which was not expected in the previously described model classes.

4. Models comparison

The models presented by Fjær (2006) and Prioul et al. (2004), as representatives of two different classes of rock models using strains to approximate the effective stiffness coefficients, were selected for further comparison in terms of trends and individual measurement points prediction accuracy. Originally, both models were supposed to be tested with the use of data obtained with the true-triaxial apparatus owned by NTNU and SINTEF Petroleum Research Formation Physics Laboratory. Eventually, due to the technical problems described in Technical Report (chapter 6), the data was taken from papers published by other authors.

4.1. Models implementation

The modelling procedures for both models were reconstructed on the basis of the aforementioned publications and implemented in MATLAB software. Simplified version of the scripts used during modelling can be found in APPENDICES A and B. The quality of approximation was estimated for each of the stiffness coefficients and in total with squared misfit function SE (SE_{ij} and $\boldsymbol{SE}$, respectively) and average percent error APE (equations APE_{ij} and $\boldsymbol{APE}$, respectively). Although SE is not normalised, and hence it favours the fit of coefficient with higher value, it was determined to be a helpful error estimator during modelling. Scripts used to estimate the errors can be found in APPENDIX C.

$$SE_{ij} = \sum_{k} \left[c_{ij}^{(k),measured} - c_{ij}^{(k),predicted} \right]^2 \tag{72}$$

$$APE_{ij} = \frac{1}{K} \sum_{k} \left| \frac{c_{ij}^{(k),measured} - c_{ij}^{(k),predicted}}{c_{ij}^{(k),measured}} \cdot 100\% \right| \tag{73}$$

$$\boldsymbol{SE} = \sum_{i,j} SE_{ij} \tag{74}$$

$$\boldsymbol{APE} = \frac{\sum_{i,j} APE_{ij}}{IJ} \tag{75}$$

where: $k - data\ point\ number, K - total\ number\ of\ data\ points, IJ - number\ of\ estimated\ stiffness\ coefficients\ for\ each\ data\ point.$

4.1.1. Inclusion model (Fjær, 2006)

Due to significant differences in parametrization and applying the influence of stress in the models, it was impossible to establish a common basis of initial parameters applicable to both of them. Initial values of the stiffness coefficients in Fjær's model are hard to be pre-estimated, as they represent properties of solid material unaffected by pores and cracks. Rock densities and porosities were taken from publications in which the experimental data was published. Moreover, constant values were assigned to drainage parameter (for dry rocks $D = 1$), parameter related to the tensile strength and Poisson's ratio (typical values for sandstones: $T_0 = 2\ MPa$ and $v = 0.2$, respectively). Initial stiffness coefficients C_{ij}^0 (via H_0 and G_0, according to equations 64) and crack densities ξ_i^0 were estimated together to fit initial values of the effective stiffness coefficients observed during the experiments. In the absence of strain measurements in the available datasets, the stiffness coefficient matrix obtained for the initial stress state (including the effects of porosity and cracks) is used to compute strains for the entire stress cycle. It is assumed that shear stresses are $\tau_{xy} = \tau_{xz} = \tau_{zy} = 0$. The porosity change was expressed in the same way as in the original publication by Fjær (2006):

$$\phi = \frac{\phi_0 - \varepsilon_{vol}}{1 - \varepsilon_{vol}} \tag{76}$$

$$\varepsilon_{vol} = \varepsilon_x + \varepsilon_y + \varepsilon_z \tag{77}$$

Further inverting for model parameters is a two-step iterative procedure. First, model parameters n, β and η are inverted for by minimizing the misfit between the predicted and the experimentally estimated stiffness coefficients for all measurement points in the dataset. Then, after finding a set of model parameters giving an error function minimum, values of solid material uniaxial compaction strength H_0 and shear modulus G_0, parameter related to tensile strength T_0 and Poisson's ratio v are redefined in order to further minimize the misfit function. These two steps are repeated several time, as long as parameter values changes make the total squared error $\boldsymbol{SE}$ value decrease by more than 0.01 GPa^2.

4.1.2. Macroscopic model (Prioul et al., 2004)

In the model published by Prioul et al. (2004) the initial stiffness coefficients $C_{11}^0, C_{33}^0, C_{44}^0, C_{66}^0$ and C_{13}^0 come directly from the experimentally observed velocities, densities and estimated Thomsen's parameters, according to equations (19-23), as they are identified with the effective stiffness coefficients at the reference pressure. Analogically to Fjær's model, strains are estimated with the use of Hook's law for TI medium. The third-order elastic constants c_{ijk} are estimated with an inversive algorithm, attached in APPENDIX D, using the differences in experimentally estimated second-order coefficients and strains between the reference and other measurement point(s) - according to Prioul et al. (2004) it is sufficient to run the inversion using readings from only two measurement points taken under hydrostatic pressure.

$$\begin{bmatrix} \Delta C_{11}^1 \\ \Delta C_{33}^1 \\ \Delta C_{66}^1 \\ \Delta C_{44}^1 \\ \vdots \\ \Delta C_{11}^n \\ \Delta C_{33}^n \\ \Delta C_{66}^n \\ \Delta C_{44}^n \\ \vdots \\ \Delta C_{11}^N \\ \Delta C_{33}^N \\ \Delta C_{66}^N \\ \Delta C_{44}^N \end{bmatrix} = \begin{bmatrix} \Delta\varepsilon_{11}^1 & \Delta\varepsilon_{22}^1 + \Delta\varepsilon_{33}^1 & 0 \\ \Delta\varepsilon_{33}^1 & \Delta\varepsilon_{11}^1 + \Delta\varepsilon_{22}^1 & 0 \\ \frac{1}{4}(\Delta\varepsilon_{11}^1 + \Delta\varepsilon_{22}^1) & \frac{1}{2}\Delta\varepsilon_{33}^1 - \frac{1}{4}(\Delta\varepsilon_{11}^1 + \Delta\varepsilon_{22}^1) & -\frac{1}{2}\Delta\varepsilon_{33}^1 \\ \frac{1}{4}(\Delta\varepsilon_{22}^1 + \Delta\varepsilon_{33}^1) & \frac{1}{2}\Delta\varepsilon_{11}^1 - \frac{1}{4}(\Delta\varepsilon_{22}^1 + \Delta\varepsilon_{33}^1) & -\frac{1}{2}\Delta\varepsilon_{11}^1 \\ & \vdots & \\ \Delta\varepsilon_{11}^n & \Delta\varepsilon_{22}^n + \Delta\varepsilon_{33}^n & 0 \\ \Delta\varepsilon_{33}^n & \Delta\varepsilon_{11}^n + \Delta\varepsilon_{22}^n & 0 \\ \frac{1}{4}(\Delta\varepsilon_{11}^n + \Delta\varepsilon_{22}^n) & \frac{1}{2}\Delta\varepsilon_{33}^n - \frac{1}{4}(\Delta\varepsilon_{11}^n + \Delta\varepsilon_{22}^n) & -\frac{1}{2}\Delta\varepsilon_{33}^n \\ \frac{1}{4}(\Delta\varepsilon_{22}^n + \Delta\varepsilon_{33}^n) & \frac{1}{2}\Delta\varepsilon_{11}^n - \frac{1}{4}(\Delta\varepsilon_{22}^n + \Delta\varepsilon_{33}^n) & -\frac{1}{2}\Delta\varepsilon_{11}^n \\ & \vdots & \\ \Delta\varepsilon_{11}^N & \Delta\varepsilon_{22}^N + \Delta\varepsilon_{33}^N & 0 \\ \Delta\varepsilon_{33}^N & \Delta\varepsilon_{11}^N + \Delta\varepsilon_{22}^N & 0 \\ \frac{1}{4}(\Delta\varepsilon_{11}^N + \Delta\varepsilon_{22}^N) & \frac{1}{2}\Delta\varepsilon_{33}^N - \frac{1}{4}(\Delta\varepsilon_{11}^N + \Delta\varepsilon_{22}^N) & -\frac{1}{2}\Delta\varepsilon_{33}^N \\ \frac{1}{4}(\Delta\varepsilon_{22}^N + \Delta\varepsilon_{33}^N) & \frac{1}{2}\Delta\varepsilon_{11}^N - \frac{1}{4}(\Delta\varepsilon_{22}^N + \Delta\varepsilon_{33}^N) & -\frac{1}{2}\Delta\varepsilon_{11}^N \end{bmatrix} \begin{bmatrix} c_{111} \\ c_{112} \\ c_{123} \end{bmatrix} + \begin{bmatrix} E_{11}^1 \\ E_{33}^1 \\ E_{66}^1 \\ E_{44}^1 \\ \vdots \\ E_{11}^n \\ E_{33}^n \\ E_{66}^n \\ E_{44}^n \\ \vdots \\ E_{11}^N \\ E_{33}^N \\ E_{66}^N \\ E_{44}^N \end{bmatrix} \tag{78}$$

where: $n - number\ of\ data\ point,\ N - total\ number\ of\ data\ points,\ r - reference\ point,$

$$\Delta\varepsilon_{ij}^n = \varepsilon_{ij}^n - \varepsilon_{ij}^r, \Delta C_{ij}^n = C_{ij}^n - C_{ij}^r, E_{ij}^n - misfit\ error$$

The inversion is carried out by numerical minimization of the misfit vector $\boldsymbol{E}$ in equation (78) derived from equations (68) and (71). The result are later tested against the constraints given by equation (69). As the resultant third-order stiffness tensor is assumed to be isotropic within a specified stress range, for some datasets it is necessary to invert for multiple sets of third-order coefficients valid within different stress limits. It is carried out by changing the data and reference points included in the inversion, and running the algorithm for each of the sets separately.

4.2. Hydrostatic stress cycle

In order to compare accuracy and characteristic features of the models in easily controllable conditions, they were used to approximate results of hydrostatic test carried out on Berea sandstone with relatively regular sampling and broad stress range (from 2.5 to 100 MPa), published by Coyner (1984). Available dataset consisted of axial P- and S-wave velocities, which allowed to estimate C_{33} and C_{44} for all measurement points. Estimated initial porosity of the sample was $\phi_0 = 17.8$ % and density $\rho = 2.197\ g/cm^3$.

4.2.1. Inclusion model – n, β, η and porosity change impact

The parameters of the inclusions model were estimated according to the procedure described in the previous subchapter. Uniaxial compaction strength value was found to be $H_0 = 53.6\ GPa$, shear modulus $G_0 = 24.6\ GPa$, parameter related to tensile strength $T_0 = 2.3\ GPa$ and Poisson's ratio $v = 0.2$. Initial crack densities in direction parallel to the bedding were set to be equal and were $\xi_x = \xi_y = 0.0716$, while crack density in the perpendicular to the bedding was $\xi_z = 0.0733$. Higher value of "vertical" crack density is rather unexpected, as it suggests that horizontal components of the in-situ stress field were larger than vertical, favouring opening of the cracks perpendicular to the direction of the vertical stress. Other possible explanations may be the presence of intrinsic anisotropy in the sample (supported by the presence of bedding, may invalidate the relation between H_0, G_0 and initial stiffness coefficients) or damage experienced by the rock during drilling. Constant reduction of the vertical stress, due to the removal of overburden disturbs the initial stress state and may lead to rock failure. It is worth mentioning that according to the relations (63) and (64) the stiffness coefficient C_{13} has negative value in the unstressed state (approximately $-1.27\ GPa$). Although unexpected, this value does not violate general bounds for VTI medium suggested by Holt (2016) shown by equation (79).

$$-\sqrt{C_{33}(C_{11}-C_{66})} \leq C_{13} \leq \sqrt{C_{33}(C_{11}-C_{66})} \tag{79}$$

$$-\sqrt{14.04(14.53-7.51)} \leq C_{13} \leq \sqrt{14.04(14.53-7.51)}$$

$$-9.93\ GPa \leq C_{13} \leq 9.93\ GPa$$

Although still within the theoretical bounds, the negative value of C_{13} may not represent correctly the actual stiffness coefficient of the medium and be just an evidence of violation of the model assumptions.

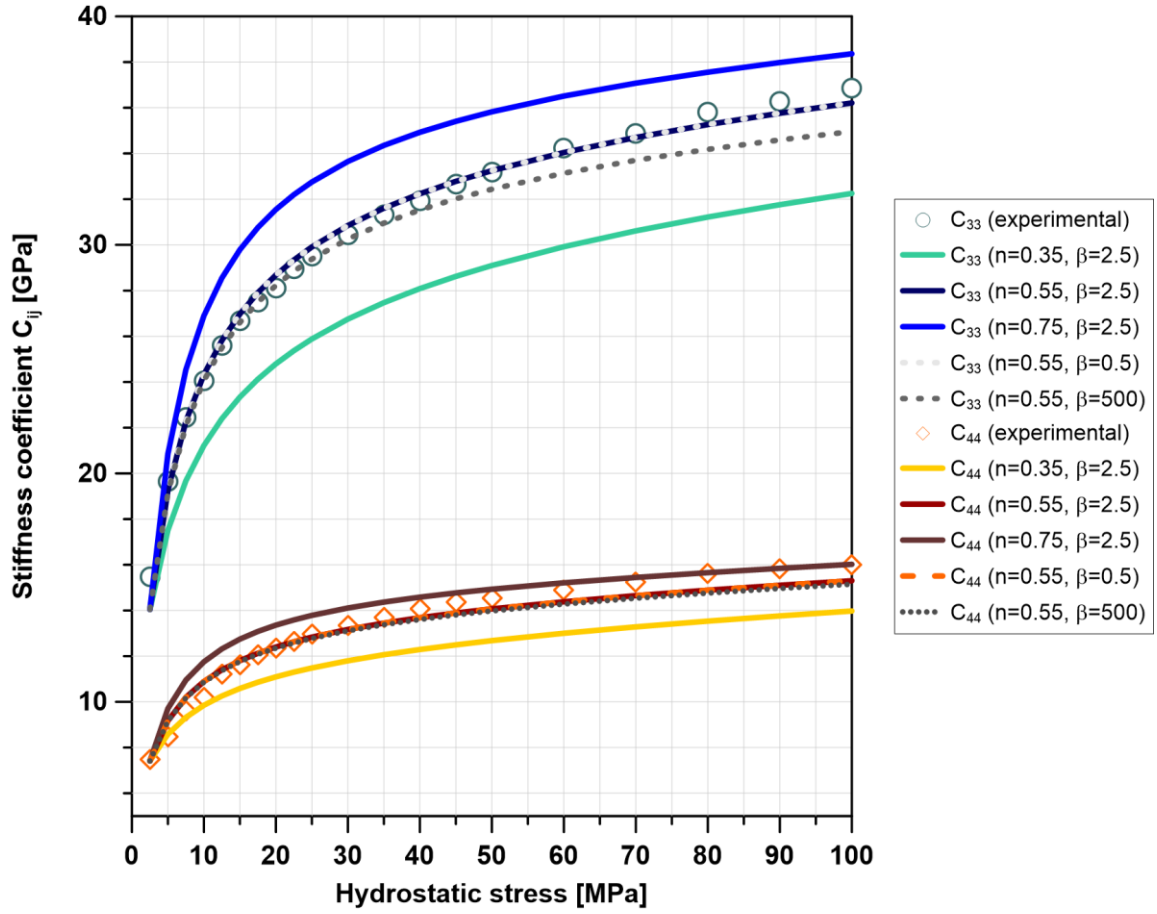

Fig. 4-1. Comparison of inclusion model parameters influence.

Fig. (4-1) shows few variants of the model, each having its own set of parameters n and β, plotted for the purpose of demonstrating the influence of individual parameters on shape of the approximated curve. The parameter n proved to have the most significant impact on the shape of the modelled function. According to the obtained results, it is the only parameter shaping the modelled rock response in the initial part of compression,

which coincides with assumption that n governs the influence of the normal stress on crack closure. When the relation between hydrostatic stress and stiffness coefficients becomes approximately linear, i.e. above 40 MPa, the curves become almost parallel. In this stress range the slope of the modelled C_{33} can be slightly modified with parameter β, steering the stress sensitivity of the rock due to shear deformation. However, for this dataset the best fit is given by models with the smallest β values, which suggest small effect of this deformation mode on rock stiffness. For C_{44} parameter β has hardly any influence on the function shape. In this particular case, the parameter η has negligible impact regardless its value, and thus was not included in the plot. It is worth noticing that one set of parameters n and β does not provide the best fit for both stiffness coefficients, C_{33} and C_{44}, and therefore it is more convenient to compare the sets in terms of misfit error sum or average rather than individual errors of particular coefficients. The most accurate realisation had $\boldsymbol{APE = 2.29}$ % ($APE_{33} = 1.54$ and $APE_{44} = 3.02$ %).

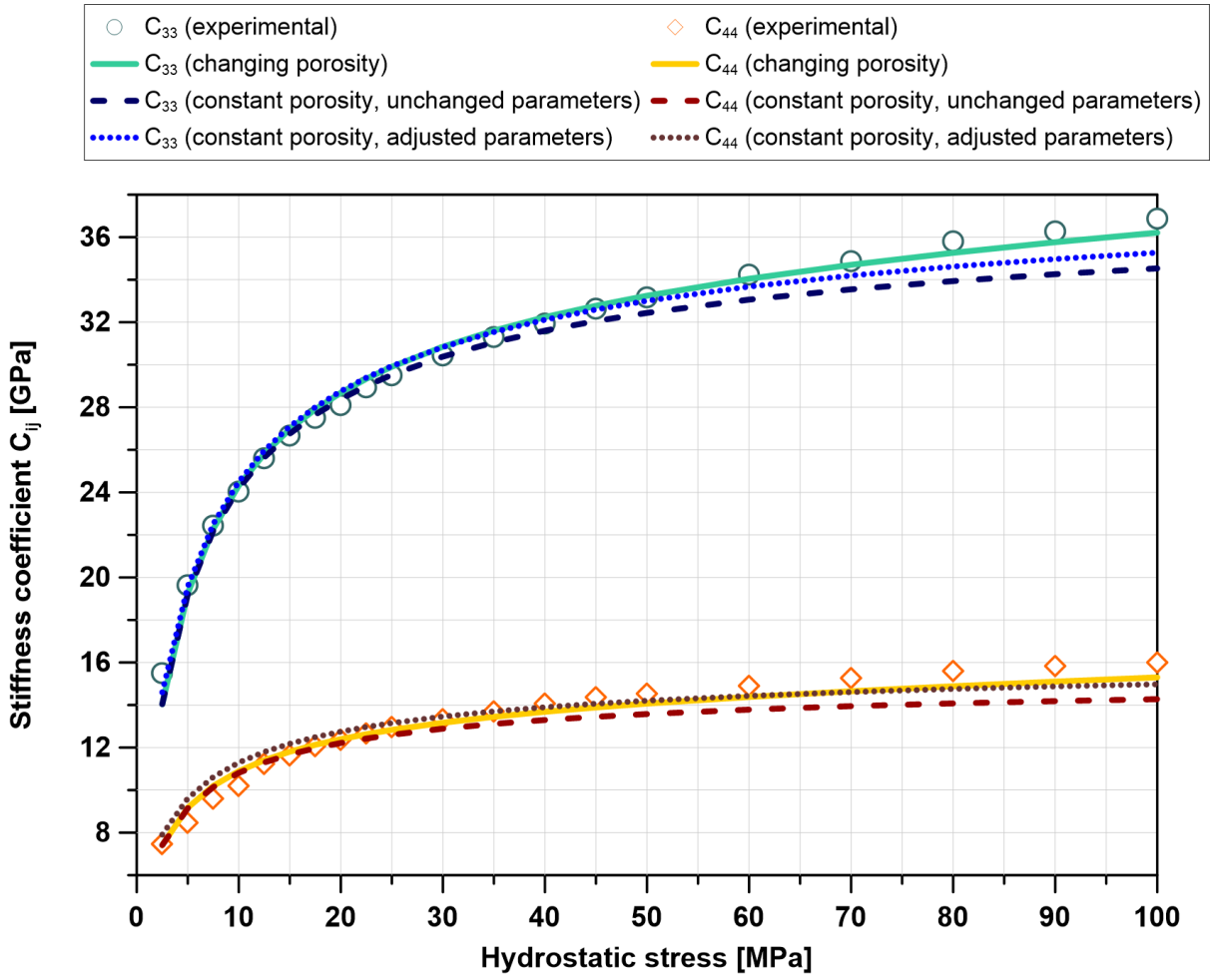

Fig. 4-2. Influence of porosity changes.

The influence of the porosity change on the inclusion model was also investigated. According to the assumptions used to model rock deformation, porosity decreases linearly with increasing hydrostatic stress. It is possible to model stress-related changes in the stiffness matrix used to invert for strains, but it would be very difficult to apply these updates for more complex stress paths with varying principal stresses and lack of constant stress change trends. Fig (4-2) shows an approximation of the stiffness coefficients with the best data fit obtained with changing porosity, another approximation obtained with the same parameters and constant porosity and, finally, one with constant porosity and readjusted model parameters. Parameters providing the best fit for the changing and the constant porosity variants of the model are shown in table 4-1.

Table 4-1. Alternative parametrization and errors (inclusion model, fig. 4-2).

Variant	**Changing porosity** $\phi = 0.178 \rightarrow 0.157$	**Constant porosity** $\phi = 0.178$
H_0 [GPa]	**53.6**	**55.8**
G_0 [GPa]	**24.6**	**26.2**
T_0 [GPa]	**2.3**	**2.4**
v	**0.2**	**0.2**
$\xi_y = \xi_x$	**0.0716**	**0.0713**
ξ_z	**0.0733**	**0.0734**
n	**0.55**	**0.51**
β	**2.5**	**2.5**
Error APE [%]	**2.29**	**3.23**

The difference in the resultant curve shape and the accuracy of approximation between the two approaches is significant. The use of constant porosity value during modelling (without introducing any changes in the model parameters) makes the predicted coefficient values drop, which becomes more and more pronounced with increasing stress, causing increasing deviation of the modelled curve from the experimental data. Excluding the porosity change from the model made the average percent error rise from 2.29 to 3.68 %. An attempt to minimize the misfit by adjusting the model parameters caused a slight improvement in the approximation quality, but cannot be considered successful

(shown in more detail in table 4-1). Compensating the stiffness drop by increasing the initial moduli and modifying n lifted the curve, but did not allow to correctly recreate experimentally observed trends. This proves that in order to provide maximum data fit it is necessary to treat porosity as yet another variable and update its value for each stress state within the cycle.

4.2.2. Macroscopic model – interval selection impact

The initial parameters of the macroscopic model C_{33}^0 and C_{44}^0 (15.49 and 7.48 MPa) were estimated with the use of the experimental data and Thomsen's parameters ε, γ and δ of Berea sandstone in nearly unstressed state (0.20, 0.18 and 0.15, respectively) were taken from Sarkar et al. (2003). Reference points were selected arbitrary depending on the number and width of the selected stress ranges in which the third-order coefficients are constant. The reference point were introduced to the inversive algorithm together with the experimental data giving several combinations of c_{ijk} used for modelling purposes.

The impact of the number of independent third-order tensors on prediction accuracy is shown in fig (4-3). The macroscopic model was computed for 1, 2 and 3 independent third-order stiffness coefficient tensors ("lines"). According to Prioul et al. (2004) it is sufficient to know the stiffness parameters for only two hydrostatic points to successfully invert for c_{ijk} coefficients, but in this study (where no C_{11} and C_{66} are known, nor modelled) all the points were accounted for to provide sufficient number of equation in the system. The third order coefficients defining the slope of the model function are shown in table 4-2. The errors were averaged for all the points except for the reference points, for which squared and percent error are equal to zero. If table (4-3) and fig. (4-3) are analysed together, it becomes apparent that the errors value drops drastically with increasing number of reference points and, consequently, sets of third-order parameters describing the modelled functions.

Table 4-2. Alternative parametrization and errors (macroscopic model, fig. 4-3).

Variant	Reference points [MPa]			c_{111} [GPa]			c_{112} [GPa]			$-c_{123}$ [GPa]			APE [%]
1 line	2.5			3850			1400			2200			17.2
2 lines	2.5	22.5		10150	1550		4350	500		5400	950		3.49
3 lines	2.5	12.5	30	13200	4450	1350	7500	1350	450	6100	2650	800	1.44

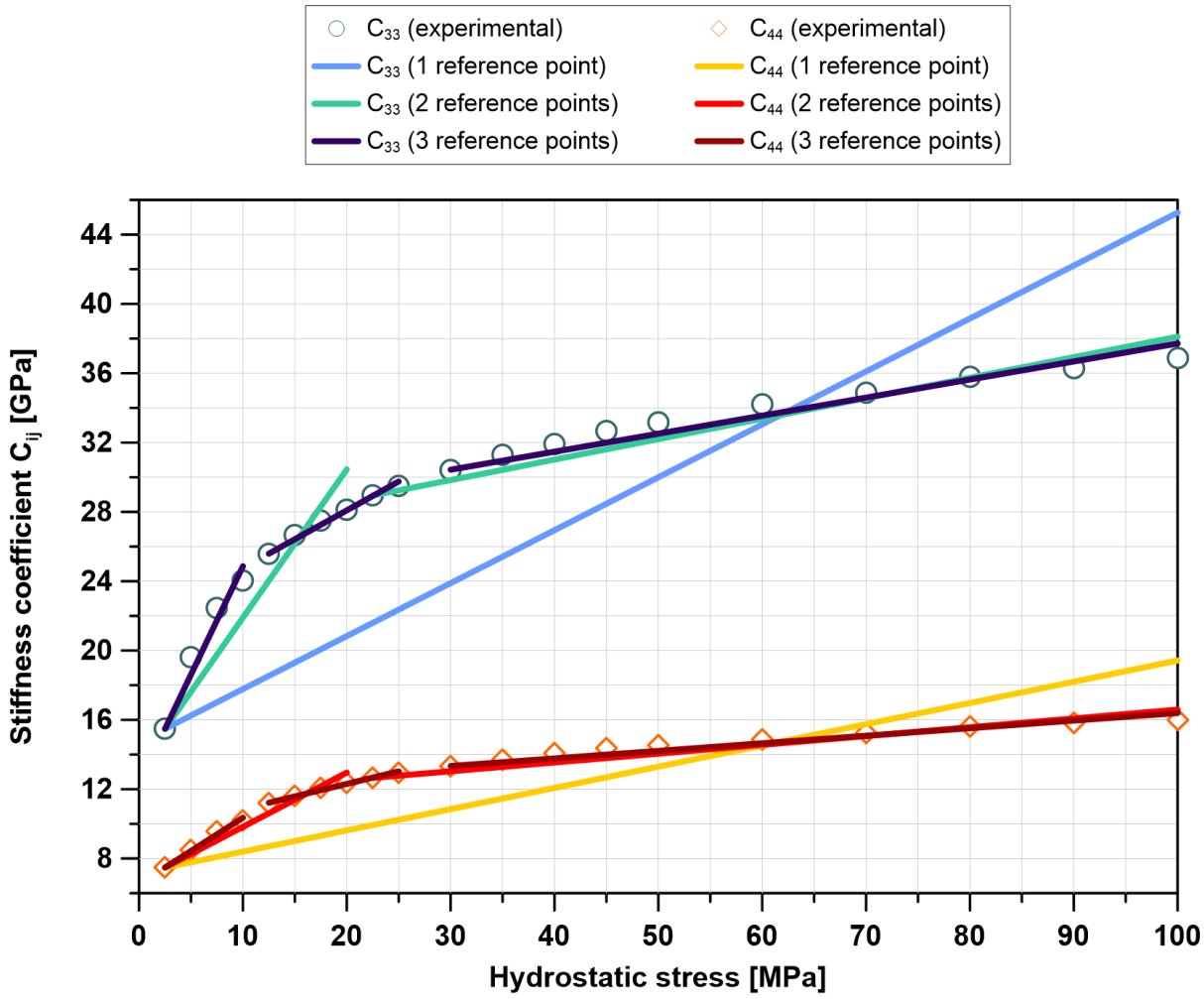

Fig. 4-3. Influence of number of sets of third-order stiffness coefficients.

Using only one third-order tensor for a broad range of stresses does not allow to approximate almost any stiffness coefficient with satisfactory accuracy. Increasing the number of independent stiffness coefficients functions for the dataset is the same as locally minimizing the error, and therefore increases the global accuracy of modelling. The higher number of fitting function, the closer the errors for particular points are to the global average for given stiffness coefficient, i.e. the lower standard deviation of error value. Hence, analysing the standard deviation of local errors in relation to the global error for the selected stiffness coefficient may be a plausible statistical method of defining the minimum number of stress intervals used for modelling. Standard deviation for particular variants of the model are compared in table (4-3). Although the number of intervals has very large impact on the error values, it is not the only factor affecting them – the selection of reference points can have significant influence on the quality of the approximation.

Table 4-3. Standard deviation of error (macroscopic model, fig. ...).

Variant	s_{33}	s_{44}
1 interval	**7.99**	**6.66**
2 intervals	**3.47**	**1.56**
3 intervals	**1.33**	**0.88**

First negative consequences of apparently incorrectly chosen stress intervals can be observed in the plot representing the variant with two stress intervals, fig (4-3), where the last values modelled by the first coefficients approximation ($\sigma_{hydrostatic} = 20\ MPa$) are higher than the very first values given by the second function. This observation is incompatible with the general data trend, and therefore could be used as a direct indicator of incorrect intervals definition. As for the number of independent intervals, also the error value may be used to support the reference points selection. Fig. (4-4) and (4-5) represent two different realisations of the model with the same number of independent stress intervals, but different reference points and, in consequence of that, parametrization.

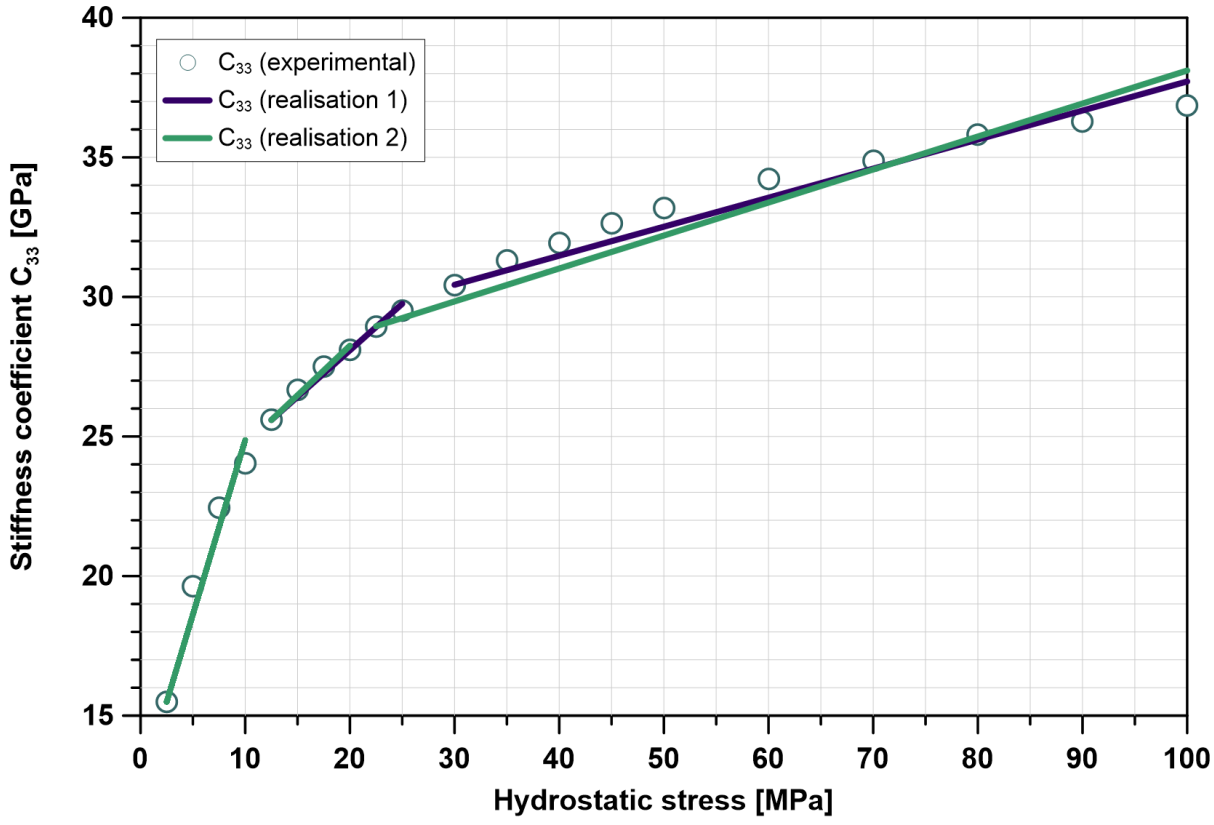

Fig. 4-4. Influence of reference points selection (C_{33}).

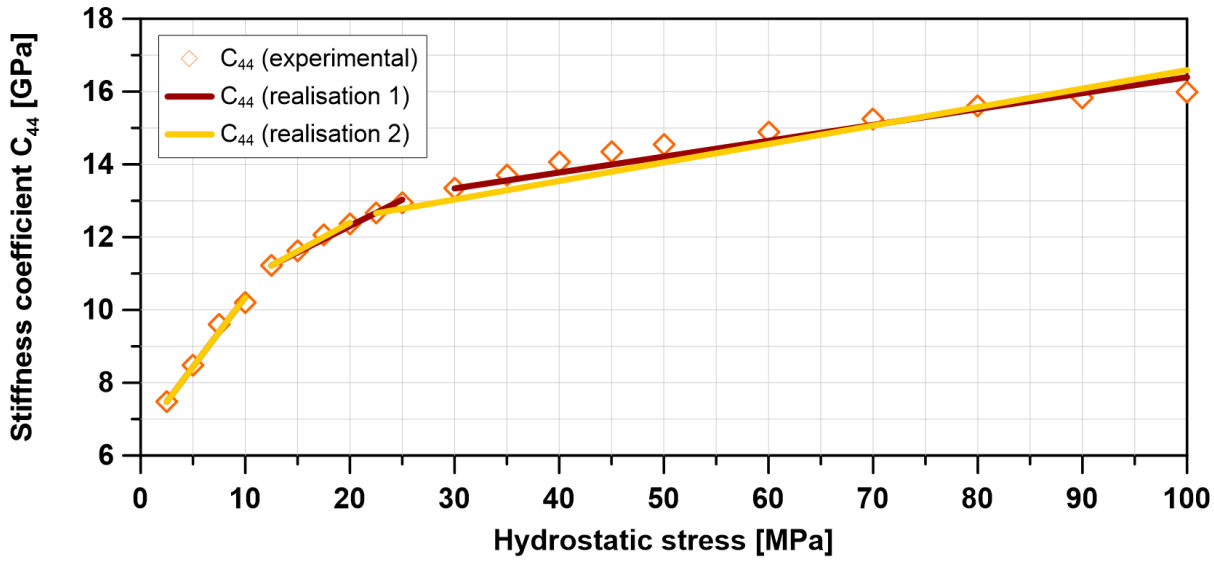

Fig. 4-5. Influence of reference points selection (C_{44}).

The first approximation (realisation 1) has been already described in the comparison of the influence of the number of stress intervals as the realisation giving the best fit to the data, while the second (realisation 2) is the very first one obtained with the script after implementing it in MATLAB. The first stress interval is identical for both realisations. The intermediate stress intervals share common reference point, but differ in length, whereas the last intervals have both different reference points and stress ranges. Consequently, as the input information for the inversive algorithm was different, the parametrization of the model for the second and the third interval also differs. The reference points, the third-order coefficients and error values of realisation 2 of the model are shown in table 4-4. The errors for each modelled coefficient and interval for both realisation are compared in table 4-5.

Table 4-4. Parameters and errors of realisation 2 (macroscopic model)

2nd & 3rd ref. point [MPa]		c_{111} [GPa]		c_{112} [GPa]		$-c_{123}$ [GPa]		APE [%]
12.5	22.5	4800	1550	1400	500	2900	950	2.02

Table 4-5. Comparison of errors for each interval and stiffness coefficient.

Model realisation no.	SE_{33} [GPa^2] interval			SE_{44} [GPa^2] per interval			APE_{33} [%] per interval			APE_{44} [%] per interval		
1	2.23	0.19	2.66	0.06	0.03	0.62	3.93	0.57	1.47	1.34	0.51	1.62
2		0.15	6.83		0.04	1.66		0.58	2.13		0.30	2.42

Comparison of tables 3 and 5 points out slight differences in parametrisation between both realisation of the model, which combined with the choice of different reference points gives origin to the increase of approximation average percent error of $\Delta \boldsymbol{APE} = 0.5\%$. The reference points selection has the largest impact on the final accuracy of the model - they should be chosen with extraordinary caution, after deeper analysis of possible quasilinear trends within the dataset. Shifting the reference point by only few megapascals may have significant consequences, especially for intervals coinciding with regions characterised by fast changes of modelled coefficients. As the model is not referring to any physical phenomena in particular, it is most reasonable to base the reference points selection on experimental observations. It is also worth noting that smaller number of data points within given interval is not automatically accompanied by lower error value, as in the second interval of C_{44} approximation. This behaviour highlights difficulties related to defining the stress intervals and arbitrary character of the selection criterions. Moreover, due to nonlinearity of rock behaviour, it may be very difficult to fit the model regardless the positioning of reference points without further increasing the number of independent (from the modelling point of view) stress intervals.

4.2.3. Model realisations comparison

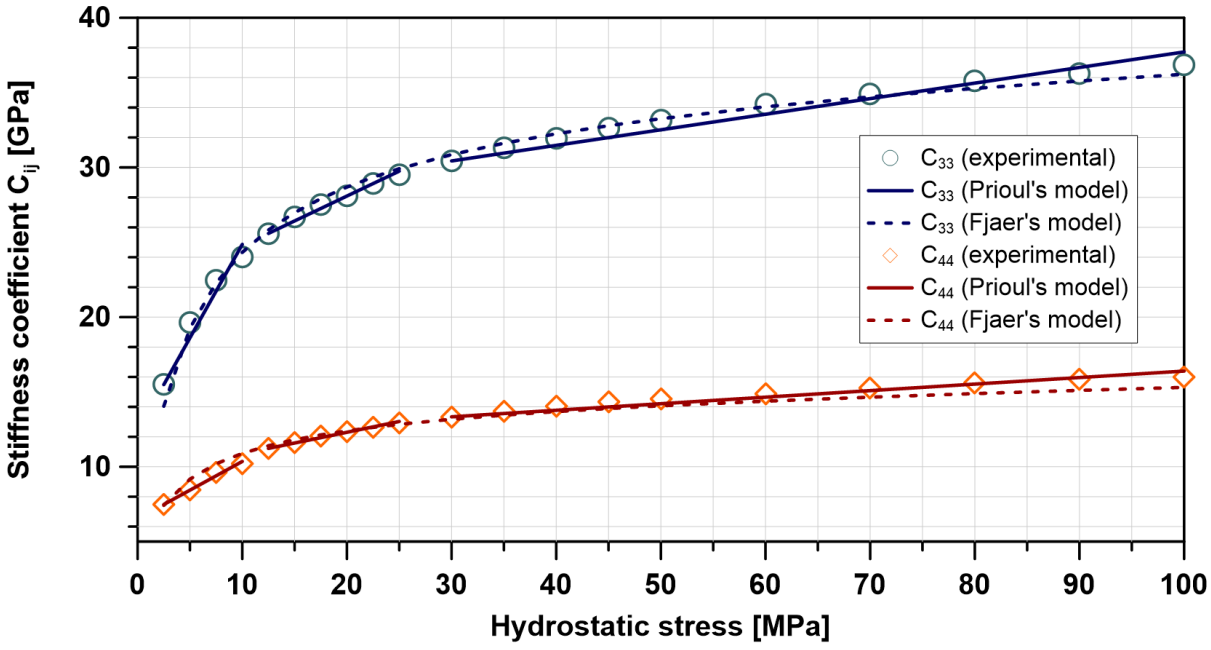

Fig. 4-6. Inclusion and macroscopic models comparison.

The most accurate realisations of the two models are shown together in fig. (4-6). The model described by Prioul et al. (2004) gives smaller misfit error ($\boldsymbol{APE} = 1.44\ \%$ for the macroscopic versus $\boldsymbol{APE} = 2.29\%$ for the inclusion model), but required at least three complete sets of input parameters to achieve the same accuracy as Fjær's inclusion model. The macroscopic model is also characterised by smaller difference of approximation quality between the modelled stiffness coefficients, i.e. the average errors for C_{33} and C_{44} are almost identical. In case of the inclusion model it was necessary to fit one of the parameters with better accuracy than the other in order to minimize the final model misfit. A significant advantage of the inclusion model is that it is able to recreate the trends within the entire stress cycle during an individual modelling procedure, whereas the macroscopic model requires division of the dataset into quasi linear well-defined stress intervals and invert for the model parameters in separate procedures.

4.3. Biaxial stress cycle

In order to compare the models in a more demanding environment, they were both used to approximate results of an experiment carried out on Colton sandstone with the use of a triaxial cell and published by Cruts et al. (1995) and Dillen et al. (1999). The same dataset was used by Prioul et al. (2004) to test the macroscopic model, which gives an opportunity to verify the modelling reliability and check the consequences of numerical inversion of strains.

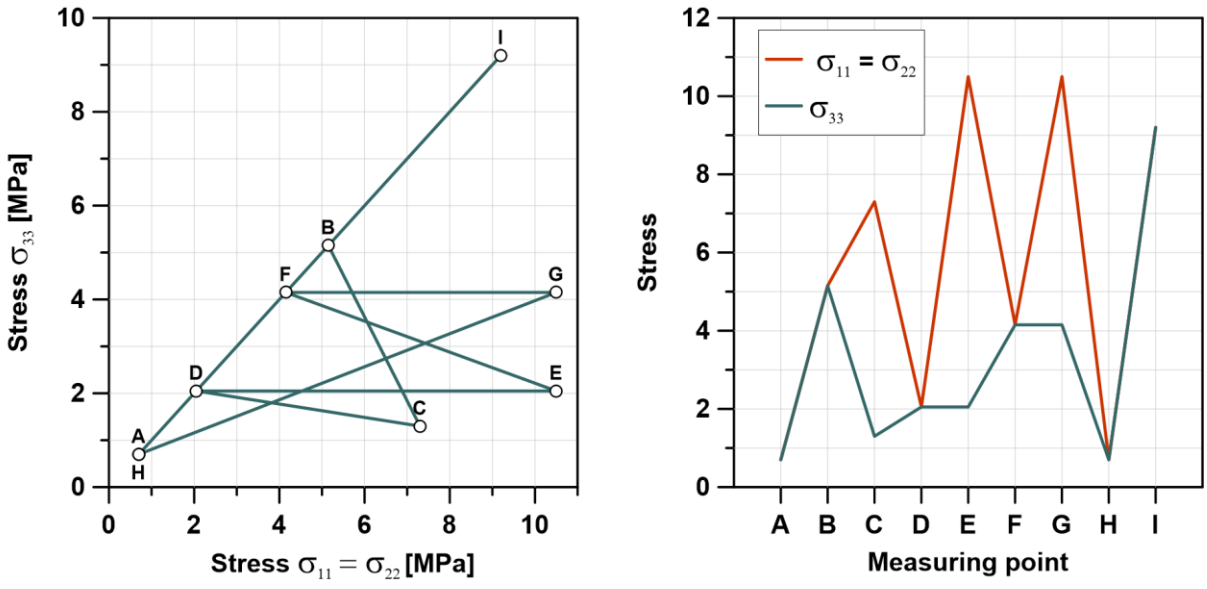

Fig. 4-7. Stress cycle (Cruts et al. 1995).

The measurements were made on cubic block (cube edge length of 205 mm) with porosity $\phi = 13\%$ and bulk density $\rho = 2.38\ g/cm^3$. In order to maintain the VTI anisotropy of the rock, stresses σ_{11} and σ_{22} were equal during the entire stress cycle (shown in fig. 4-7). Due to abundance of experimentally estimated stiffness coefficients (C_{11} estimated from V_{11} and V_{22}, C_{44} from V_{13}, V_{31}, V_{23} and V_{32}, and C_{66} from V_{12} and V_{21} – first index indicates the direction of propagation and the second the polarization direction) inversion were initially carried out with the use of stiffness constants averages.

4.3.1. Inclusion model – impact of error minimization

Smaller maximum stresses ($\sigma_{max} = 10.5\ MPa$) give an opportunity to have a better look into small-scale accuracy of the approximations and discrepancies between the models. In the case of the inclusion model it allowed to investigate various error minimization approaches. First and probably the most obvious way to invert for the model parameters is to minimize the global misfit error, so that the average percent error estimated for all stiffness coefficients has the lowest possible value. Another tested approach was to achieve the lowest equal values of average approximation error estimated separately for stiffness coefficients related to P- (C_{11} and C_{33}) and S-wave (C_{44} and C_{66}) propagation. Finally, the last used inversion criterion was to minimize the misfit error of P-wave- and S-wave-related coefficients independently. The model parameters obtained from each of the mention inversions are presented in table 4-6 (minimized error highlighted with orange background).

Table 4-6. Inclusion model parametrization - influence of the inversion criterions.

Inversion mode	Global error	Equal partial error	Privileged C_{11} and C_{33}	Privileged C_{44} and C_{66}
H_0 [GPa]	90	90	90,1	90
G_0 [GPa]	29,8	29,8	30	29,4
T_0 [GPa]	2,2	2,2	2,2	2,2
v	0,199	0,199	0,199	0,199
$\xi_y = \xi_x$	0,0913	0,0913	0,0913	0,0913
ξ_z	0,0953	0,0953	0,0951	0,0963
n	0,056	0,062	0,054	0,081
β	0.4	0.4	0.4	5.0
$APE_{C_{11}\,\&\,C_{33}}$[%]	1.04	1.74	0.96	4.35
$APE_{C_{44}\,\&\,C_{66}}$[%]	1.96	1.74	2.14	0.88
APE [%]	1.50	1.74	1.55	2.62

All realisations of Fjær's inclusion model are shown together and compared with the experimental results in fig. (4-8). For all the inversion modes the initial moduli (H_0, G_0 and T_0), Poisson's ratios v and crack densities ξ_i are fairly stable and their values differ by less than 2%. The most significant changes can be observed for n parameter denoting the stress sensitivity related to normal stress – it's value changes by 50% between the best approximations of P- and S-wave moduli. Lower values of n parameters improved the fit of P-wave coefficients, C_{11} and C_{33}, slightly decreasing the accuracy of the approximation of S-wave-related constants, C_{44} and C_{66}.

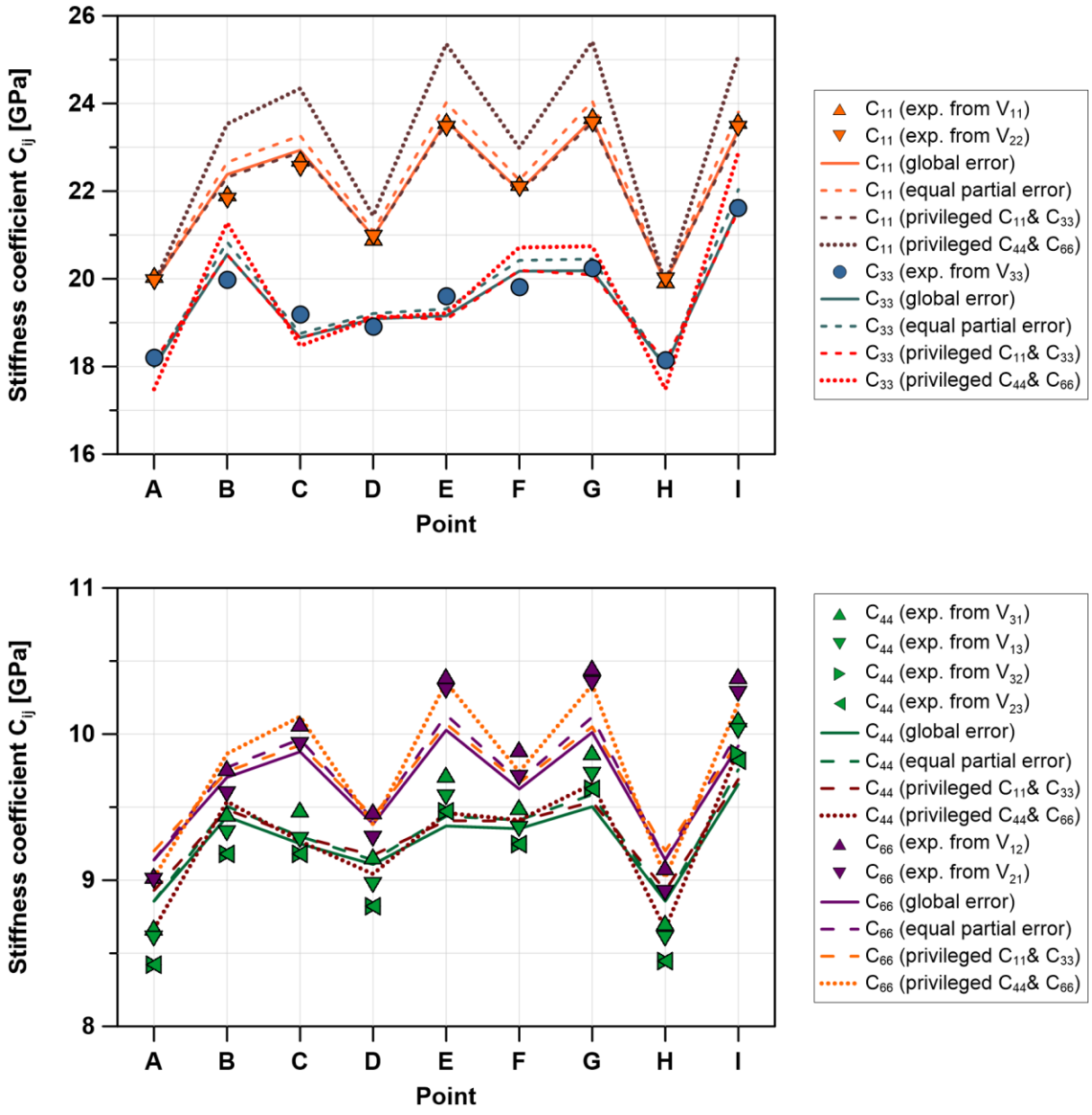

Fig. 4-8. Inclusion model parametrization - influence of the inversion criterions.

The increment of n value, apart from increasing the rate of change of all modelled coefficients, causes an asymmetrical response, slightly improving the fit of S-wave coefficients and provoking a significant drop of C_{11} and C_{33} estimation quality. In consequence, the inversion promoting the C_{44} and C_{66} misfit minimization gives an estimation error of P-wave coefficients exceeding by a factor of 5 the error for the S-wave-related coefficients and produces the largest global error among all fitting algorithms. The results indicate that, for this particular dataset, higher values of the parameter describing the impact of shear deformation on the crack density β allow to obtain better fit for C_{44} and C_{66}. On the other hand, all the other inversion variants gave significantly reduced values of this parameter, highly limiting the impact of the shear deformation mode. Although the results of the inversion privileging C_{44} and C_{66} applied to the model are the only set of parameters giving reasonably good fit for both, lower and higher values of S-wave-related stiffness coefficients, they do not provide good fit for high values of C_{11} and C_{33}. Yet another argument against the inversion favouring the fit of C_{44} and C_{66} coefficients is that the resultant initial parameters violate the bounds shown in equation (79), giving the initial value of $C_{13}^{\sigma=0} = -14.15\ GPa$ and limits:

$$-\sqrt{17.48(19.88-8.67)} \leq C_{13} \leq \sqrt{17.48(19.88-8.67)}$$

$$-14.00\ GPa \leq C_{13} \leq 14.00\ GPa$$

The other three inversions yield very low values of the parameter $C_{13}^{\sigma=0}$, being just at the edge of the ranges given by Holt (2016). As in the case of Berea sandstone, it may indicate the presence of a lithological sources of anisotropy in the sample, and therefore it raises doubts about the fulfilment of the model assumptions. Accordingly to the described above asymmetrical growth of the approximation error for P- and S-wave-related stiffness coefficients in relation to n parameter changes, the minimum global error criterion promotes better fit of C_{11} and C_{33}. The resultant errors of approximation for the two pairs of coefficients differ by a factor of 2. Using the parameter $n = 0.062$ (being the result of the inversion aiming to minimize equal average error of both groups of coefficients), although not providing the lowest global error, gives an equilibrium between overestimated pressure wave and underestimated shear wave coefficients. Hence, this inversive algorithm was used for further comparison with realisations of the macroscopic model.

4.3.2. Macroscopic model – impact of inversive algorithm

The initial values of Thomsen's parameters required to carry out modelling with the use of the macroscopic model were taken from the same publication as the model itself (Prioul et al., 2004) - vertical velocities $V_{P0} = 2.77\ km/s$ and $V_{S0} = 1.89\ km/s$, Thomsen's epsilon $\varepsilon = 0.05$, gamma $\gamma = 0.03$ and delta $\delta = 0.05$. In the case of experimental results published by Cruts et al. (1995)there was no need to apply more than one set of macroscopic model parameters to cover the entire stress interval. Due to the abundancy of the experimental stiffness parameters, inversions were run first on averages of stiffness matrix elements (giving four equations per measurement point - one for each stiffness parameter, i.e. C_{11}, C_{33}, C_{44} and C_{66}) and later with all available stiffness constants (nine equations per measurement point). Prioul et al. (2004) suggested that to invert for the coefficients c_{ijk} it is sufficient to include in the inversive algorithm experimental result from only two measurement points, at which the sample was subjected to a hydrostatic stress field (in here points A and B). The inversive algorithm described in section 4.1.2 and shown in APPENDIX D using coefficients averages did not manage to recreate the results obtained in the original publication, nor achieve comparable estimation accuracy using the parameters obtained under this assumption. Attempts to increase the accuracy of the inversion by computing the third-order coefficients with the use of the experimentally approximated values of all available stiffness coefficients (instead of their averages) improved significantly the fit, and achieved almost the same level of approximation accuracy as obtained by the model Authors. However, its results are characterised with larger misfit difference between the P- and S-wave-related coefficients.

Table 4-7. Macroscopic model parametrization - influence of the measurement points selection.

Inversion mode	Prioul et al., 2004 (points A & B)	Prioul et al., 2004 (points $A - I$)	Two hydrostatic points (A & B)	All measurement points ($A - I$)
c_{111} [GPa]	7700	7400	5800	6900
c_{112} [GPa]	1000	1400	1900	1550
c_{123} [GPa]	-100	- 600	- 1800	- 850
$APE_{C_{11}\ \&\ C_{33}}$ [%]	1.22	1.05	0.70	0.84
$APE_{C_{44}\ \&\ C_{66}}$ [%]	1.03	0.80	1.67	1.05
APE [%]	1.12	0.92	1.19	0.94

An inversion using all the data from six hydrostatic measurement point failed to bring the third-order coefficients closer to the values providing decent fit to the experimental data. After more meticulous investigation it was found that the results of the inversions using experimentally estimated stiffness coefficients from all hydrostatically compressed measurement points violated some of the conditions given by equations (69) - in some cases the relations between c_{144} and c_{155} were not preserved. Finally, an inversive algorithm exploiting data from all measurement points (within hydrostatic and biaxial intervals) managed to achieve required fit quality without breaking the constrains of the model, but still did not manage to outscore the original parameter set proposed by Prioul et al. (2004). The third-order stiffness coefficients obtained from the inversions using all available stiffness coefficients from a short hydrostatic interval and all measurement points are presented in table 4-7. The resultant second-order stiffness coefficients are shown in fig (4-9) and (4-10).

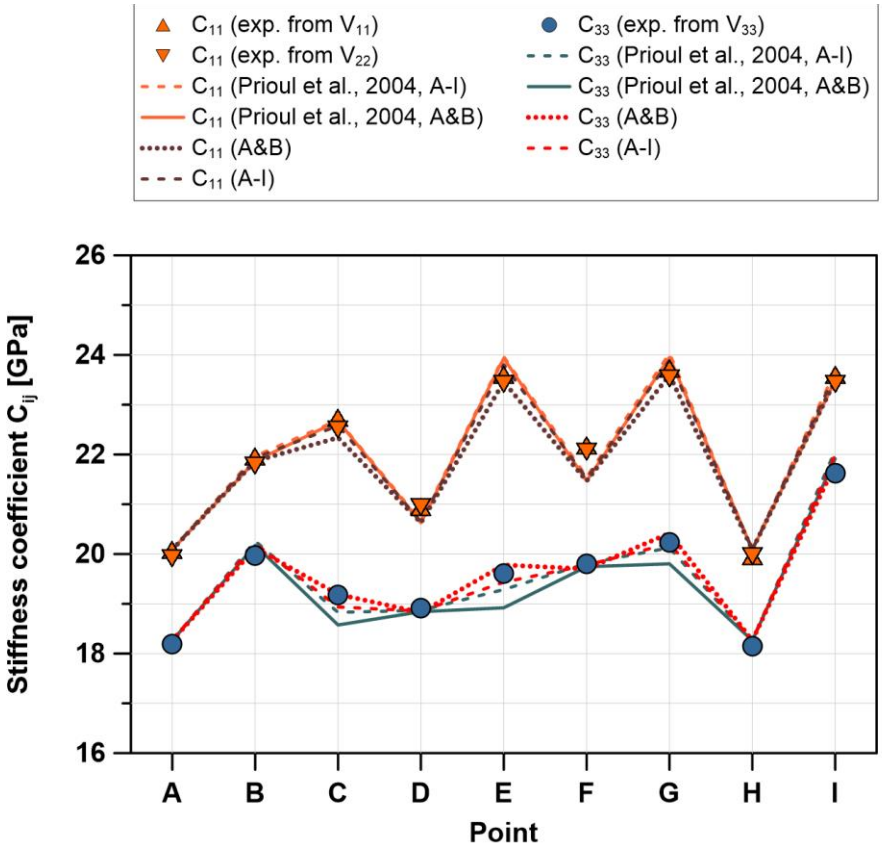

Fig. 4-9. Macroscopic model parametrization - influence of the measurement points selection (C_{11} and C_{33}).

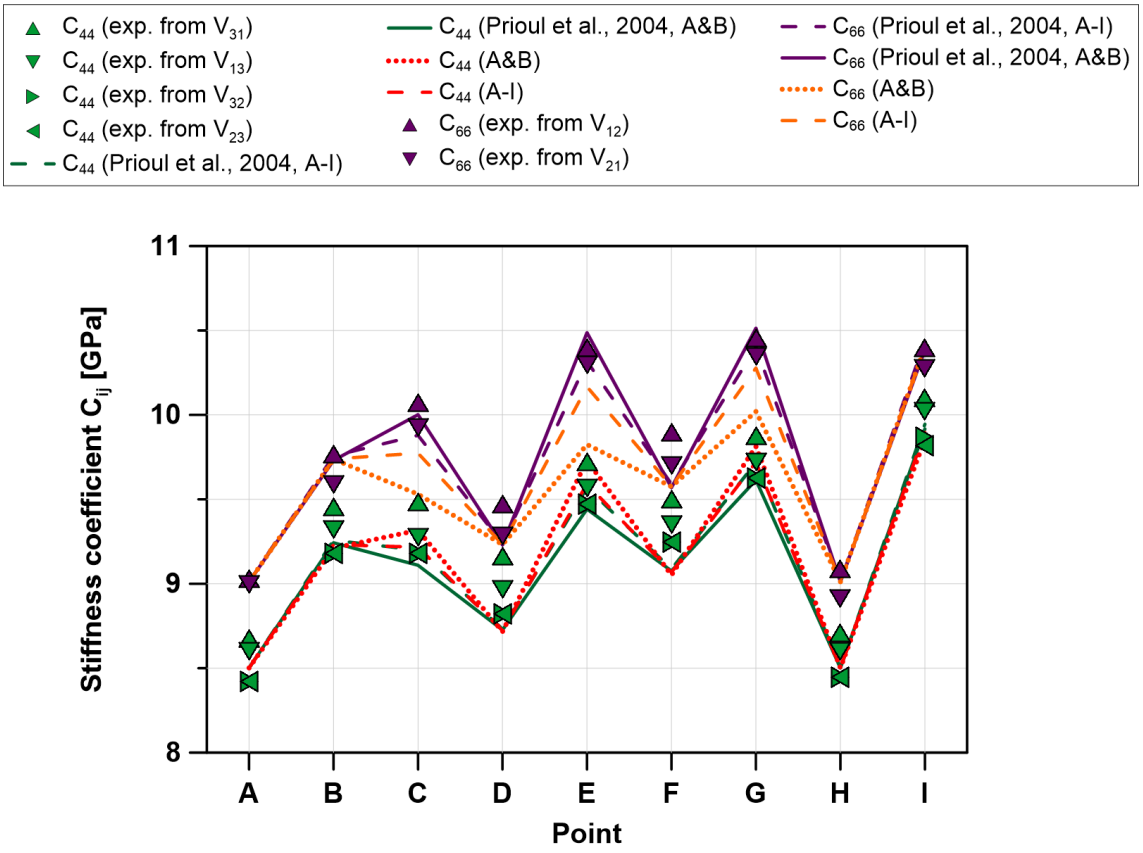

Fig. 4-10. Macroscopic model parametrization - influence of the measurement points selection (C_{44} and C_{66}).

All of the analysed sets of third-order stiffness coefficients succeeded in approximating the trends and the exact values of C_{11} coefficient. In the case of C_{33}, the models using c_{ijk} parameters estimated from a pair of hydrostatic measurement points manage to recreate the stiffness parameters for all hydrostatic points, but were further from the experimentally estimated values for biaxial stress intervals - the model using parameters estimated from points A & B given by Prioul et al. (2004) underestimated the values of C_{33} by almost 0.7 GPa. The differences between the approximations are significantly more pronounced for the parameters C_{44} and C_{66}. The third-order stiffness tensors provided by the model Authors gave better approximation of the coefficient C_{66}. The parameter set estimated from two hydrostatic points, behaving similarly to the analogical set given by Prioul et al. (2004) in the case of C_{33}, underestimated C_{66} and failed to recreate the change trends for all points within biaxial stress intervals. However, all the sets gave a reasonable fit for C_{44}, which could be related to the high number of equations for C_{44} (4 out of 9 for each point) implemented in the inversive algorithm.

A certain level of discrepancies between the inversion results and the third-order stiffness tensor proposed by Prioul et al. (2004) was expected due to the inaccessibility of the original strain records. One of the possible causes of such large differences in the parameter values and approximation quality could be the use of different numerical operators used to minimize the error between the experimental results and modelled data. Moreover, the misfit in the built-in MATLAB functions is defined as non-normalised difference between the predicted and the experimentally estimated stiffness coefficients (in a similar way as the squared error $\boldsymbol{SE}$ used to preliminarily assess model accuracy) - initially it was assumed to be irrelevant and was identified as a possible cause of the algorithm dysfunction in the final phase of the project.

4.3.3. Model realisations comparison

The realisation of the inclusion model giving an equal value of average estimation error for both pairs of coefficients (C_{11}&C_{33} and C_{44}&C_{66}) and the results of macroscopic modelling obtained with the use of the parameters from inversion including all available stiffness coefficients from the entire stress cycle are compared in fig. (4-11). Although both models are characterised with the approximation error below the uncertainty of measurement, assumed by Prioul et al. (2004) to be 2% of the estimated second-order stiffness parameter value, the difference in modelling quality is significant. The coefficients $C_{11}$and C_{66} are approximated better by the macroscopic model, which outdoes the inclusion model in terms of the error value and trends reconstruction. In comparison to the macroscopic approach, the inclusion model tends to overestimate C_{11} and does not capture the subtle changes of C_{33} between the measurement points C and G. This differences are well reflected in the estimation errors of C_{11} and C_{33} coefficients of the macroscopic and the inclusion model given in tables 4-6 and 4-7 (0.84% and 1.74%, respectively). Even clearer differences can be observed in the part of fig (4-11) showing the approximations of C_{44} and C_{66} ($APE_{44\&66}^{macroscopic} = 1.05\%$ and $APE_{44\&66}^{inclusion} = 1.73\%$). Although both approaches give an opportunity to reconstruct the trends of coefficient changes fairly accurately, the inclusion model underestimates their amplitude giving "averaged" values of the stiffness constants – it underestimates the high coefficients values (points A, D and H) and overestimated the low ones (points E, G and I). Similar approximation quality can be achieved only if inclusions model parameters are computed separately for P- and S-wave-

related stiffness coefficients, as shown in fig. (4-8). However, it is worth noting that the differences between the minimum and maximum values of stiffness coefficients are relatively small (between 13.6 and 15.8%), and therefore a model using general physical properties of the rock, and not statistically extracted macroscopic parameters, may be expected to face serious problems in approximating the entire matrix of stiffness parameters within such a short interval in a relative low-stress regime.

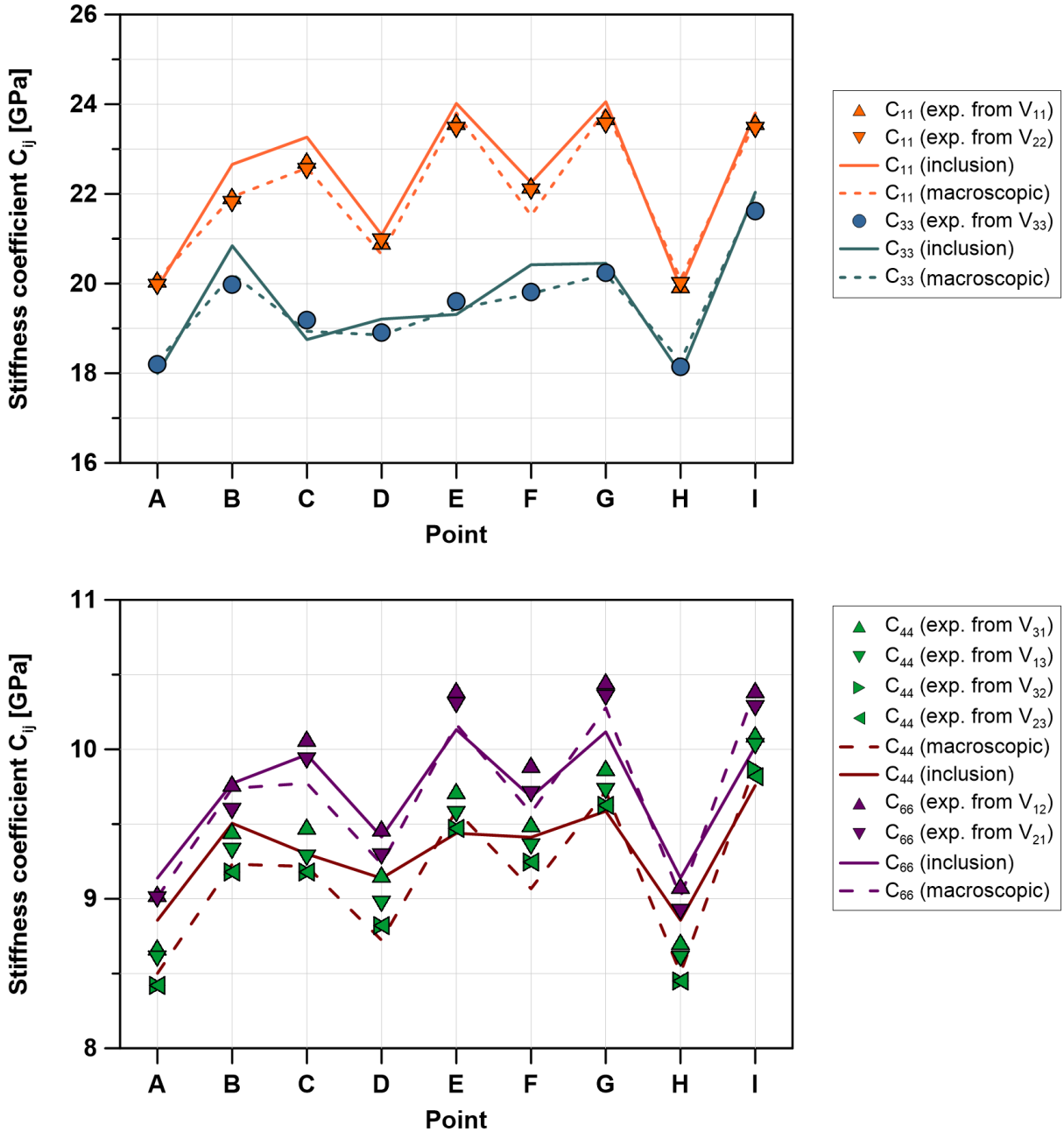

Fig. 4-11. Models comparison.

5. Theory & numerical modelling - summary and conclusions

In order to set up a basis for understanding different approaches to describe the anisotropy and estimate its impact on the experimental results, the anisotropy concept and various possible anisotropy sources were introduced. Two main types of anisotropy, i.e. *intrinsic* and *extrinsic*, were defined, as well as the mechanisms responsible for their creation (which affect the manner of their physical analysis and mathematical description).

Describing the general form of Hook's law, used to explain the stress-strain relationship, supported by introduction of the elastic stiffness coefficients, normal and shear components of stress and strain vectors, allowed to present the most common anisotropy classes (orthorhombic and transverse isotropy). Their characteristics, most popular applications and influence on the shape of the stiffness matrix were described. To simplify the indexing system of the elastic stiffness matrix elements, Voigt's notation was also introduced.

To establish a link between the experimental results and the theoretical description of anisotropy, seismic velocities of P- and S-waves in isotropic and anisotropic medium were defined. An alternative parametrization of an anisotropic body, so called Thomsen's parameters, was shown and the relations between the parameters and the shape of a propagating wavefront were explained.

Different classes of the rock models, used to model the response of the rock to external stresses, were introduced. The granular approach, originating from the analysis of the interactions between individual grains within the medium, was described. Various stages of the granular model complexity (simple linearly elastic grains deformation analysis gradually gaining additional terms responsible for lateral displacements, slipping and the influence of cementation on the contacts stiffness) were shown. The inclusions models, based on the analysis of the influence of pores and cracks on the effective rock parameters, were introduced. Different types of inclusions, varying in shape and orientation, and their impact on the mathematic apparatus of this class of models were described. Crack density and fracture impact coefficients, together with parameters responsible for different modes of rock deformation, were defined and introduced into the model. Finally, the macroscopic rock model using only the effective characteristics of the rock was described. In contrast to the previously mentioned model classes, this approach is not based on any particular

physical phenomena and its parametrization is defined through statistical analysis of the rock behaviour within selected stress interval.

The final stage of this part of the thesis was to compare two from the described models in terms of approximation accuracy and general trends reconstruction. The inclusions model presented by Fjær (2006) and the macroscopic model published by Prioul et al. (2004) were selected for the comparison. The models represent different model classes, but both of them use strains to approximate the effective stiffness coefficients, which allow to model the behaviour of a transversely isotropic rock under hydrostatic and non-hydrostatic stresses. MATLAB software was used as a main platform for model implementation, parameters inversion and approximation error estimation. Initially, the models were supposed to be tested with the use of stress, strain and ultrasonic data collected with the true-triaxial apparatus from Formation Physics Laboratory (SINTEF Petroleum Research). Due to the technical problems described in Chapter 6, it was necessary to introduce significant changes in the thesis structure and its objectives, and use the data published by other authors. At first, the models were tested using the data from hydrostatic measurements carried out on Berea sandstone with stresses varying between 2.5 and 100 MPa (Coyner, 1984).

The second test was performed with the data from biaxial stress cycle with minimum stress value of 0.7 and maximum of 10.5 MPa with the use of a sample of Colton sandstone (Cruts et al., 1995). Because of the lack of the original strain data (in both cases only the stress and the ultrasonic velocity measurements were available) it was necessary to linearize the stress-strain relationship and invert for strains numerically – this could have significant influence on the final results of modelling, and therefore was taken into consideration as one of the possible factors responsible for deviations of the models from the experimentally obtained values of the stiffness parameters. Apart from direct comparison of the results given by both models, various parametrizations, model elements, parameter inversions modes and error minimization methods were investigated.

The inclusion model, using the uniaxial compaction strength H_0 and the shear modulus G_0 of the rock unaffected by pores and cracks, the initial crack densities in each of the principal directions ξ_i^0 , the initial porosity ϕ_0, the tensile strength parameter T_0 and Poisson's ratio v as the initial parameters, was used to estimate the effective stiffness parameters, within the entire stress cycle, with an individual model realisation. The

inversion for the model parameters n, β and η scaling the impact of sensitivity of the rock and cracks to normal and shear deformation was performed by minimization of the percent error of approximation of particular stiffness coefficients or their averages. The initial stiffness coefficients (at stress state $\sigma_x = \sigma_y = \sigma_z = 0$, no influence of cracks and pores) were estimated directly from H_0 and G_0. The impact of inclusions was introduced with the use of the initial porosity ϕ_0, the initial crack densities ξ_i^0 and the impact factor Q. During modelling, the porosity and crack densities were updated according to stresses and strains experienced by the rock and the parameters n, β and η. The model was computed by introducing the updated values of porosity and crack densities into the equations for the effective stiffness coefficient, in each selected stress state. The initial parameters were also updated in order to minimize the misfit between the estimated and the experimental stiffness coefficients.

One of the first difficulties was to estimate the initial values of moduli H_0 and G_0, representing the parameter of a solid material. These value cannot be directly measured and should be approximated together with other model parameters, so that the stiffness coefficients in the point under the lowest hydrostatic stress are approximately equal to the experimentally obtained values. It should be also taken into account, that the relationship between the solid material moduli (H_0 and G_0) and the initial stiffness coefficients is based on the assumption that anisotropy of the rock originates only from the extrinsic sources. In the case of intrinsic anisotropy this relation could be inaccurate, and therefore the initial stiffness coefficients values should be controlled during the entire modelling process. One of the possible control mechanism is to test the stiffness coefficients against theoretical bounds (Holt, 2016). It could be also argued that the initial crack densities are significantly affected by the drilling and coring processes, and hence they have very limited relation with the in-situ conditions experienced by the rock. Both tests indicated that the most prominent model parameter is n, reflecting the influence of the normal stress on crack density. The impact of the parameters β and η (scaling the influence of shear deformation and crack stress-sensitivity, respectively) on the results of the both tests was very limited, but it should be assumed that it could be more pronounced under different experimental conditions. According to the tests run on different variants of Fjær's inclusions model it was concluded that updating the porosity values, regardless of the amplitude of changes, helps to obtain better fit with the experimental data, and therefore should not be neglected. Using a unique set of parameters (based on the physical properties of the rock)

allows to employ the inclusion model for the entire experimental interval and extrapolate the stiffness coefficients beyond it. As shown in the hydrostatic example, the inclusion model is very accurate in recreating the trends and the rate of change within very broad stress ranges. On the other hand, it was also observed that the set of parameters providing the best global fit does not estimate the P- (C_{11} and C_{33}) and S-wave-related parameters (C_{44} and C_{66}) with equal accuracy. The low-stress regime was identified as the zone with the highest discrepancies in the approximation quality. The difference between the n parameter values giving the best fit for the mentioned coefficients pairs was as high as 50% (at the same time the initial parameters values were changed by less than 2%), which could suggest that it would be beneficial to introduce an additional scaling factor or parameter differentiating between the modelled stiffness coefficients. Nevertheless, despite the possible assumptions violation (presence of the intrinsic anisotropy) the inclusion model manages to recreate the experimental results with relatively high accuracy.

The macroscopic model requires Thomsen's parameters (or the stiffness coefficients) of the rock at the reference hydrostatic stress state as input. The third-order stiffness coefficients c_{111}, c_{112} and c_{123}, governing the impact of the deformation of the rock on the effective stiffness coefficients, are computed with the use of an inversive algorithm using experimental results from various points within the analysed interval. In case of broad experimental intervals it is convenient to use more than one reference point, and therefore also a set of model parameters. Selection of the reference points and the interval length is theoretically unrestricted.

As the third-order stiffness coefficients are not directly related to a particular physical phenomena (e.g. grain contact stiffening, crack closure or opening), nor to any of the rock moduli, they cannot be estimated *a priori*. Moreover, Prioul and Lebrat (2004) suggested theoretical bounds for the c_{ijk} coefficients, which define only some relative relationships between the coefficients - there are no clear limits of the third-order tensor elements values, and hence the ability to control the model parameters before running the simulation is limited. Due to the statistical character of the third-order stiffness coefficients, they are highly dependent to the numerical inversion method, and therefore they are vulnerable to any changes introduced to this algorithm. The number of experimentally estimated stiffness coefficients used as the input for the inversion plays a crucial role in limiting the estimation error – the third-order stiffness coefficients obtained for a single pair of measurement points

differed significantly from the coefficients obtained with the use all available data points and the results of analogical inversion published by the model Authors. The results suggest that the number of independent estimations of each stiffness coefficient (depending on the types, propagation and polarization directions of ultrasonic waves recorded on each measurement point) used during the inversion affects the accuracy of approximation of particular C_{ij} coefficients. In that case, the predictive power of the model would be directly dependent to the abundance of the experimental results. The assumption that the third-order stiffness coefficients denote constant gradients in the strain-stress coordinates forces fragmentation of the model in case of wide stress intervals. Although the initial stiffness coefficients can be extracted easier than in the inclusion model, they have to be estimated separately for each of the modelling intervals, which increases the number of required parameters significantly. Moreover, because of the local character of the model parameters, it may be risky to extrapolate the data outside the analysed interval. Due to the arbitrary character of the selection of number and length of the modelling intervals, the accuracy of the model may depend greatly on the choices made by the interpreter. However, it was concluded that interval selection can be assessed objectively by comparing standard deviation of errors in particular intervals with standard deviation of all partial errors. Furthermore, comparing the extreme values of any neighbouring intervals allows to avoid under- or overestimation of the stiffness coefficients on the interval edges. Despite all potentially harmful features, the macroscopic model flexibility (in terms of coefficients values and intervals position) allows to obtain precise approximation within selected stress interval – the macroscopic model managed to achieved better approximation accuracy in both test.

In summary, despite significant differences in parametrization, model parameters inversion routine and application range, they can both be successfully used to model the elastic stiffness parameters of VTI media in hydrostatic and non-hydrostatic stress states. Both models were able to estimate the stiffness coefficients of the rock with accuracy error below 2% (which can be treated as a reasonable experimental error value). Due to the dissimilarities in the very basic model assumptions, the models can be interchangeably applied, depending on the modelling purpose – the inclusions model can be used as a reasonable approximation of stiffness parameters values and their change rates within

wide stress ranges, whereas the macroscopic model can be more successful in short intervals (well constrained by the experimental results intervals).

6. Technical report

6.1. Apparatus general description

The true-triaxial apparatus located in SINTEF Petroleum Rock Physics Laboratory was originally constructed and operated by Royal Dutch Shell. It was first described briefly by Sayers et al. (1990). The apparatus consists of two perpendicular sets of steel beams being a frame for the entire measurement setup. On the opposite sides of the frame there are Enerpac RSM-300 hydraulic jacks installed, one pair for each axis. This particular actuators placement reduces possible shear stress component which could affect orientation of a sample. Rock samples are installed in the central point of the space created by the frame, in the crossing point of axes given by the actuators. It is positioned with the use of steel-made acoustic transducer holders (element SP2) and an aluminium frame (element SP1) designed to facilitate the process by keeping the sample and the other elements of the system tightly together. When hydrostatic stress of around 0.5 MPa is applied the frame can be removed. The apparatus and SP1 frame are presented in fig. (6-1).

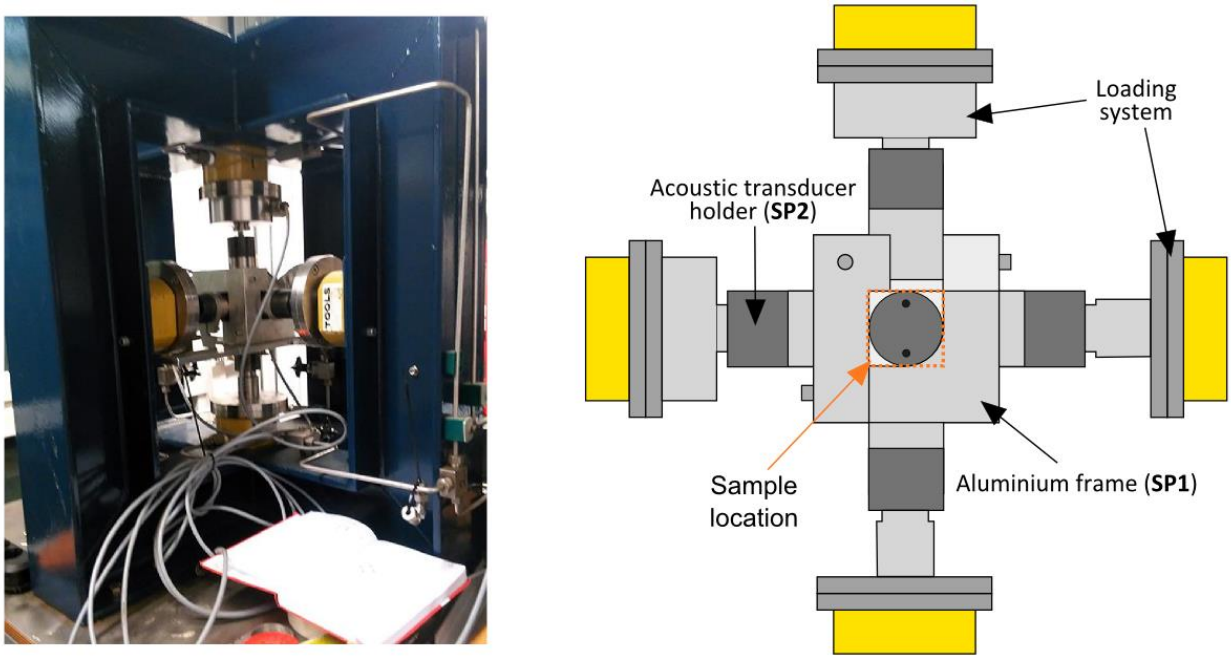

Fig. 6-1. Sample placement in the apparatus.

In order to create pressure inside the actuators, they are connected to a hydraulic system consisting of several hand and electronic pumps, located below the apparatus table. In purpose of measuring forces exerted by the actuators, each axis is equipped with a load cell produced by HBM, model C2, characterised by maximum measurable force of 200 kN and accuracy of 0.2 %. To transmit force from the actuators to a sample, a set of holders (elements SP2) was used. Each holder consists of two steel elements (one being in direct contact with the actuators and the other having a hole dedicated to host an acoustic transducer inside) and an exchangeable contact platen (element SP3, fig. 6-2). To improve the contact between the transducer and the platen, an metal string was inserted inside the holder.

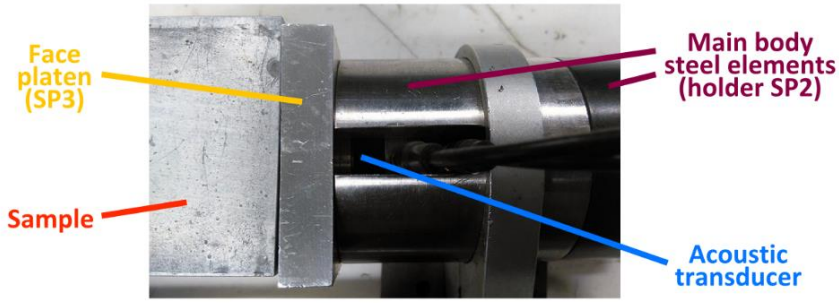

Fig. 6-2. Transducer holder.

Strain along each of the main axes was originally measured with the use of linear variable displacement transducers (LVDT) produced by SANGAMO Schlumberger attached to the SP2 steel holders. An individual "column" of the setup is presented in fig. (6-3).

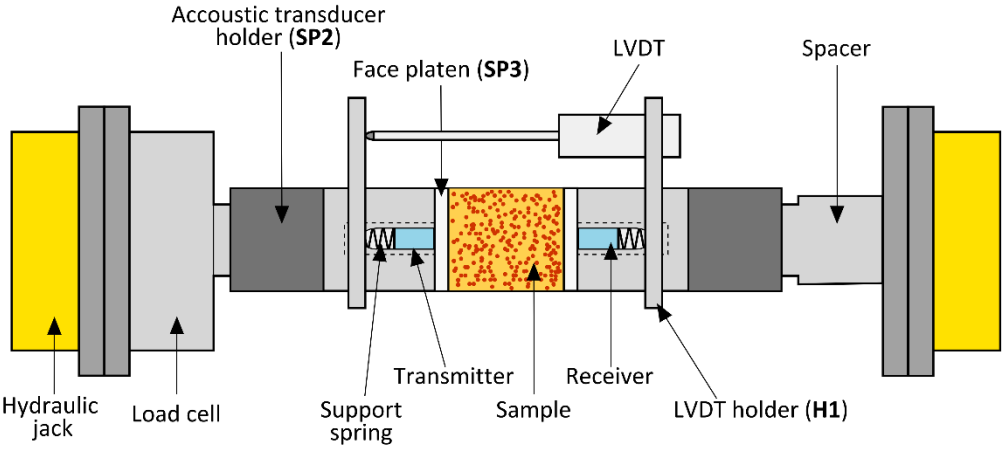

Fig. 6-3. Measuring system elements and sample placement in the apparatus.

The face platens, providing contact between the acoustic transducer holders (SP2) and a sample, were originally made with aluminium. SP1 frame, used to mount samples into the apparatus, required three pairs of platens of dimensions of *47x47*, *47x50* and *50x50* mm, making it necessary to use a different force-stress relationship for each of the pairs.

The apparatus has not been used for several years, and therefore it required maintenance work, elements quality control and multiple modifications to be introduced. As there was no instruction, nor technical specification available, each of the elements had to be investigated and tested separately in order to verify how to operate them correctly.

6.2. Sensors modification and calibration

One of the first modifications introduced to the apparatus was to exchange connectors of all LVDTs and load cells. Original 7-pin connectors were exchanged with 15-pin versions to allow plugging them in QuantumX MX840A amplifier.

The distance between the elements of the loading system elements made it impossible to insert a reference sensor without an additional support. In order to carry out calibration of the load cells it was necessary to manufacture an additional steel-made reference transducer adapter (element C1), as shown in fig. (6-4). Due to the weight of the adapter, an additional support was necessary. The PVC supporting element (C2) is shown in fig. (6-5) together with the entire calibration setup. More detailed plans of these elements are presented in APPENDIX E

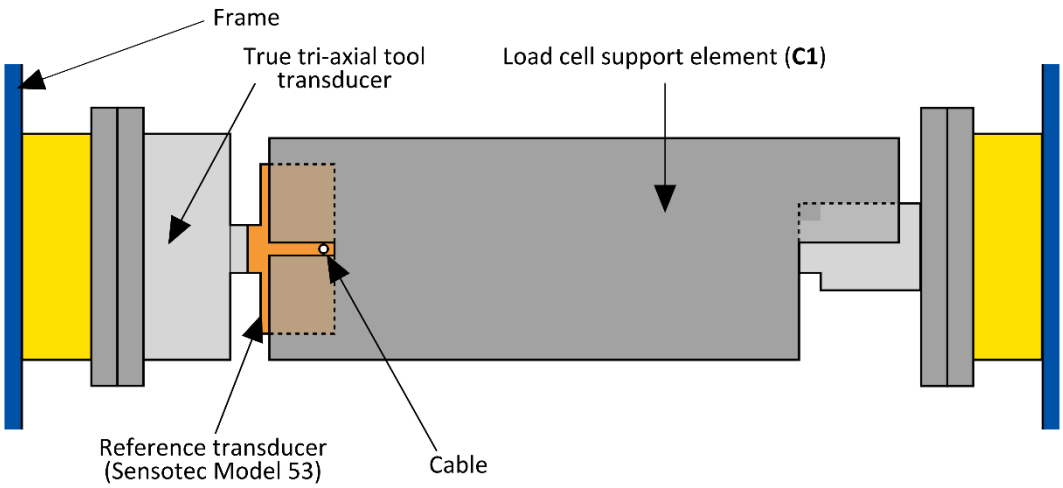

Fig. 6-4. The reference load sensor placement.

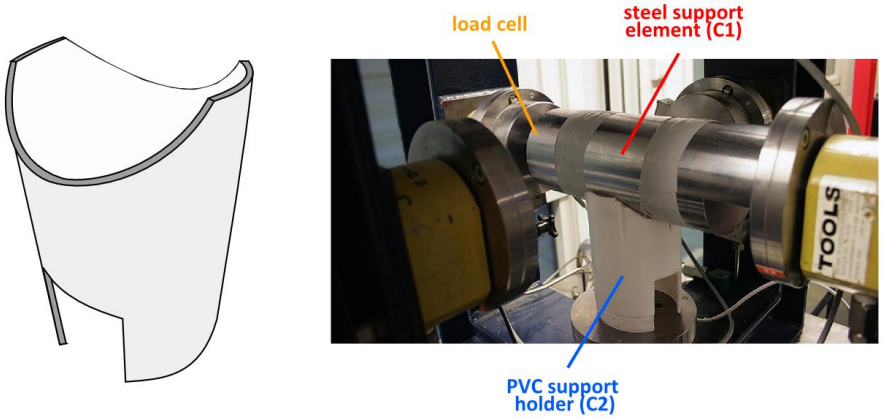

Fig. 6-5. PVC supporting element C2 (left) and the calibration process (right).

In the case of Sensotec Model 53 (reference transducer) and HBM C2 load cells, a two-point calibration scheme was used for a force range extremes of approximately 0 and 160 kN, and later verified with a supplementary test carried out during loading and unloading process. Results of both tests are presented in fig. (6-6) and, in more detail, in APPENDIX F.

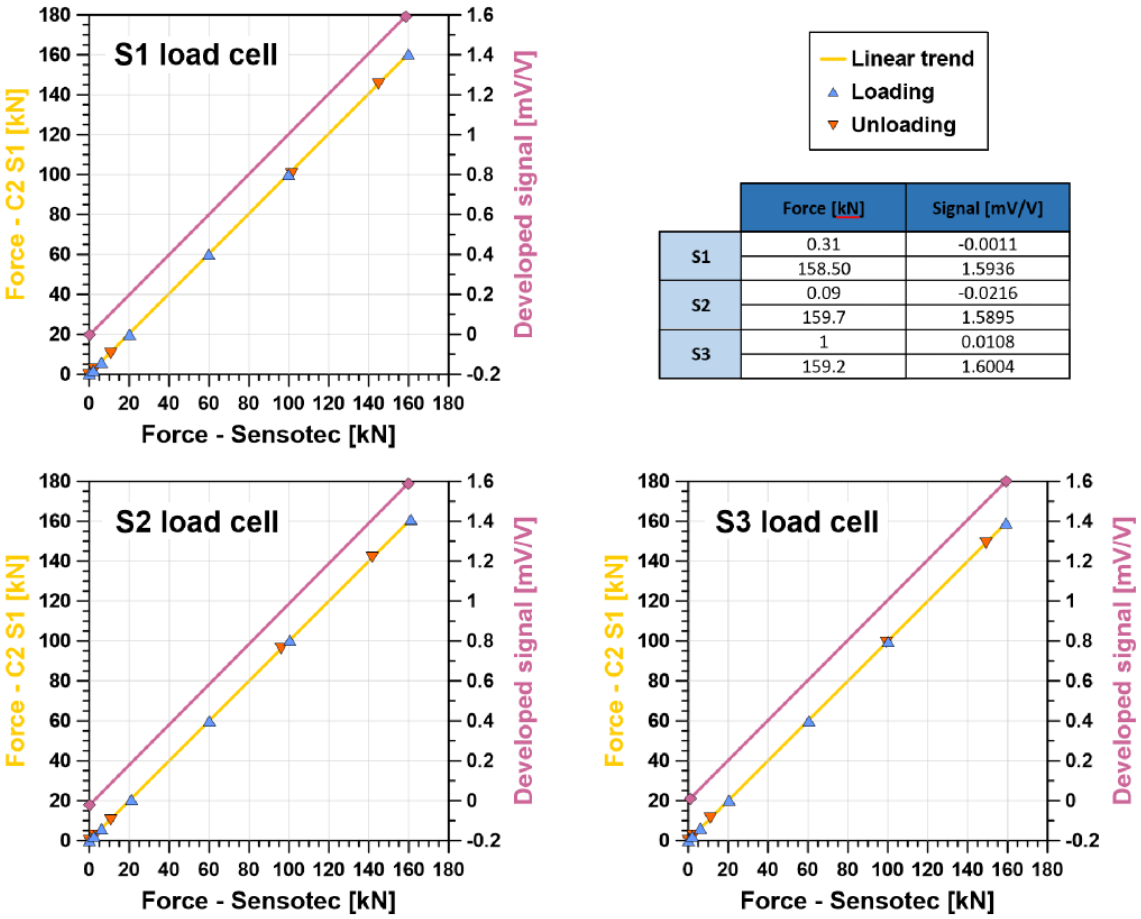

	Force [kN]	Signal [mV/V]
S1	0.31	-0.0011
	158.50	1.5936
S2	0.09	-0.0216
	159.7	1.5895
S3	1	0.0108
	159.2	1.6004

Fig. 6-6. Load cells calibration results.

All loading cells exhibited highly linear and repeatable behaviour, and therefore they were declared as fit to use in forthcoming tests.

Calibration of LVDTs was carried out using the multipoint method. It allowed not only to define a relationship between the observed voltage and the resultant displacement, but also to estimate a range of linearity for each of the sensors. Extremes of the measurement range are indicated by abrupt increase of deviation from the linear trend, and should be individually used to verify any experimental results obtained with the displacement sensors. According to the producer, the LVDTs were expected to give linear relationship within the range of *5 mm*. In order to provide accurate and precise displacement measurements during the procedure, a digital micrometre was used. The results of calibration are presented in fig. (6-7).

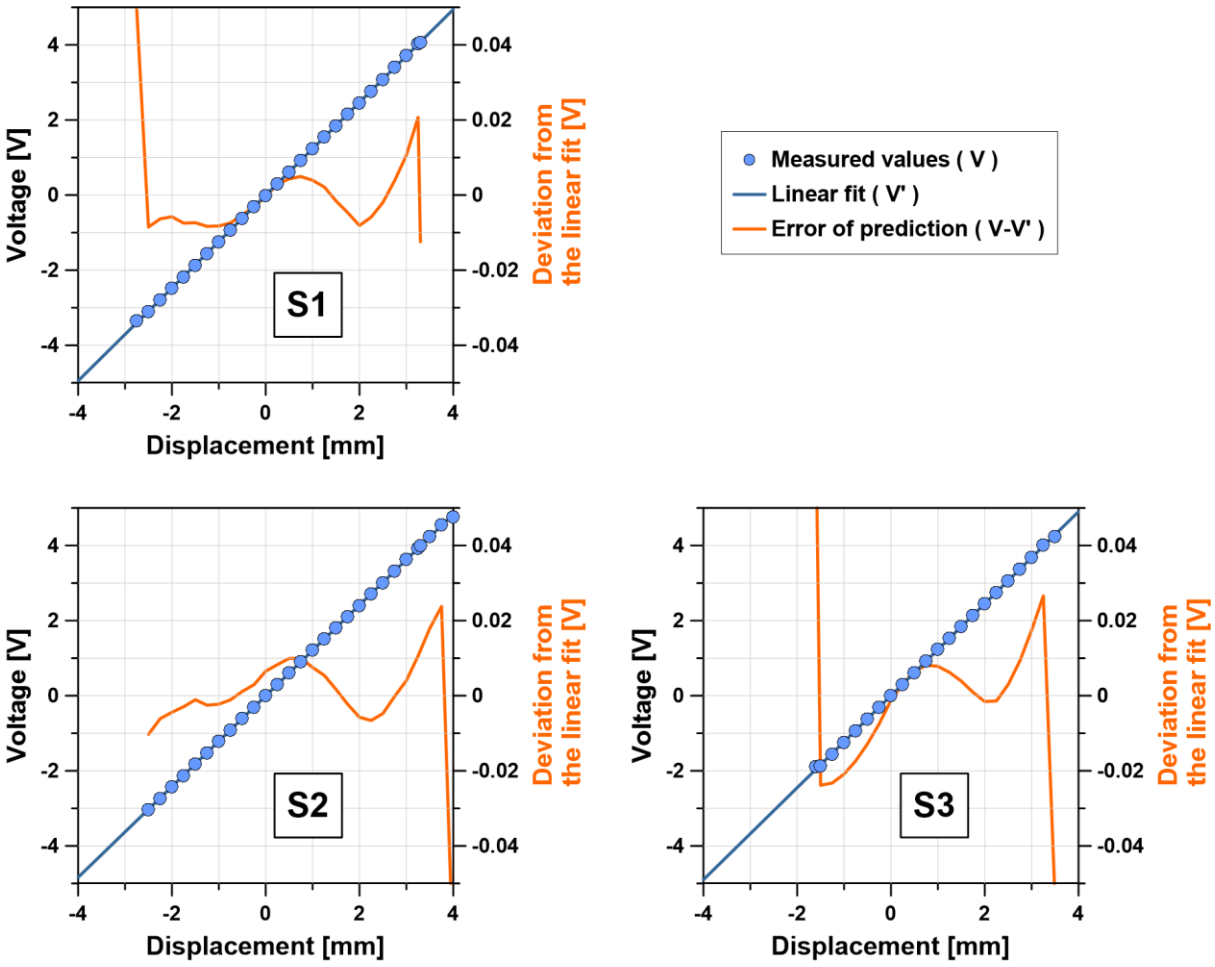

Fig. 6-7. LVDTs calibration results.

Transducers S1 and S3 are characterised with well-defined linearity extremes on both ends of the measuring range, meanwhile transducer S2 does not have a clear extreme for negative displacement values. Furthermore, for S2 and S3 the linearity ranges are highly unsymmetrical and are shifted towards the positive displacement values (compression). It could be related to individual characteristics or damages experienced by the sensors.

6.3. Hydraulic system modification

In the original form, the hydraulic system consisted of a set of three electric pumps supported with an additional set of two handpumps and three rotary pumps, as presented in fig (6-8). Each of the electric pumps was connected to a particular subsystem, supported with an individual rotary pump, responsible for providing hydraulic pressure to a particular pressure actuator mounted in the apparatus frame. The hand pumps were installed in a more universal manner, allowing to control the horizontal and vertical pressure separately. All the subcircuits could be cut off from the hand pumps with the use of control valves, and therefore they can be operated separately using the electric and the rotary pumps.

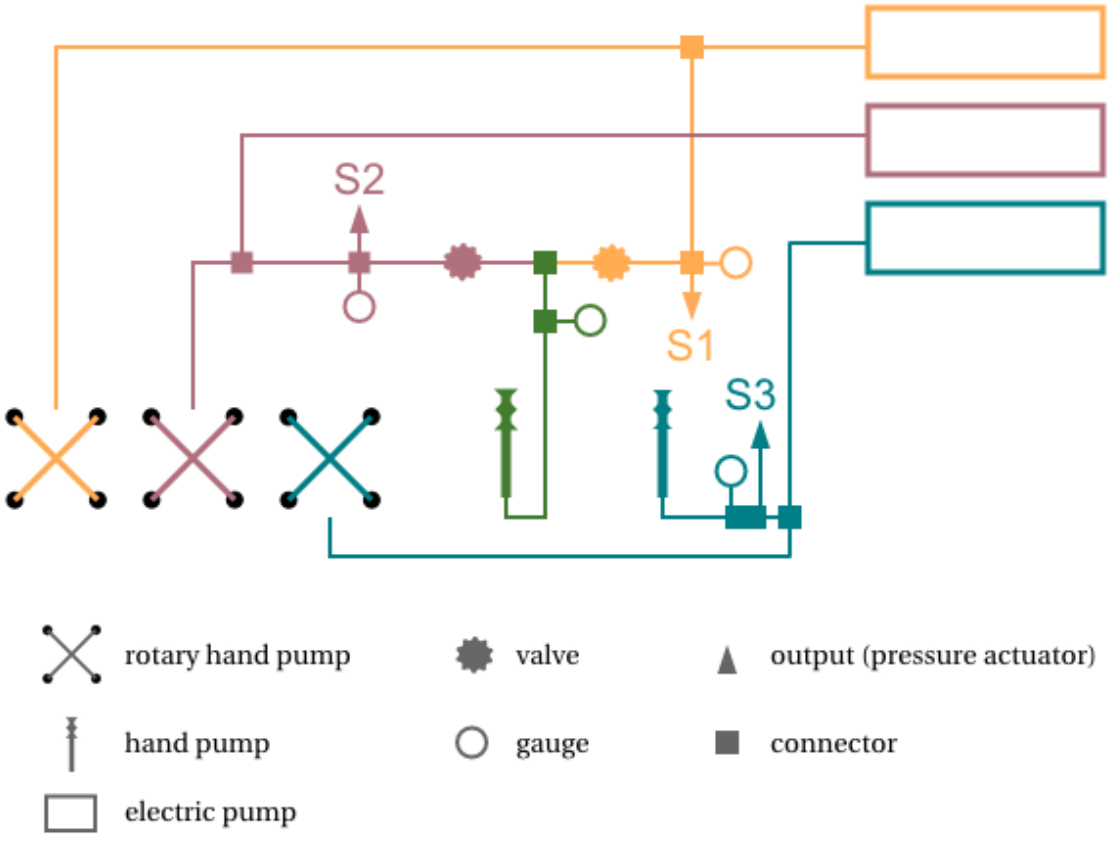

Fig. 6-8. Original hydraulic system.

As there was no software for the electric pumps available, a decision to detach the electric system to limit possible costs and time of preparation of the apparatus has been made. For further simplification, one of the hand pumps was also detached, and the other was connected to all three actuator subsystems. Hence, it could be used to build hydrostatic stress on a sample without the need for equilibrating the fluid pressure between the subsystems. The rotary pumps were unaltered, as they provided excellent conditions for controlling pressure differences when valves between the main hand pump and actuators were closed. In order to have a full control over the pressure after modifying the main pump- and rotary pump-operated subsystems, some of the valves were relocated, so that each of the subsystems could be monitored and operated separately. The original elements were kept in place even after they were detached from the hydraulic system – all of the above alterations were carried out by modifying the high-pressure piping network and adding or removing valves and plugs. The final configuration of the hydraulic system is presented in fig. (6-9). The entire system was designed and constructed to sustain a pressure of 20 000 psi (≈ 1380 bar).

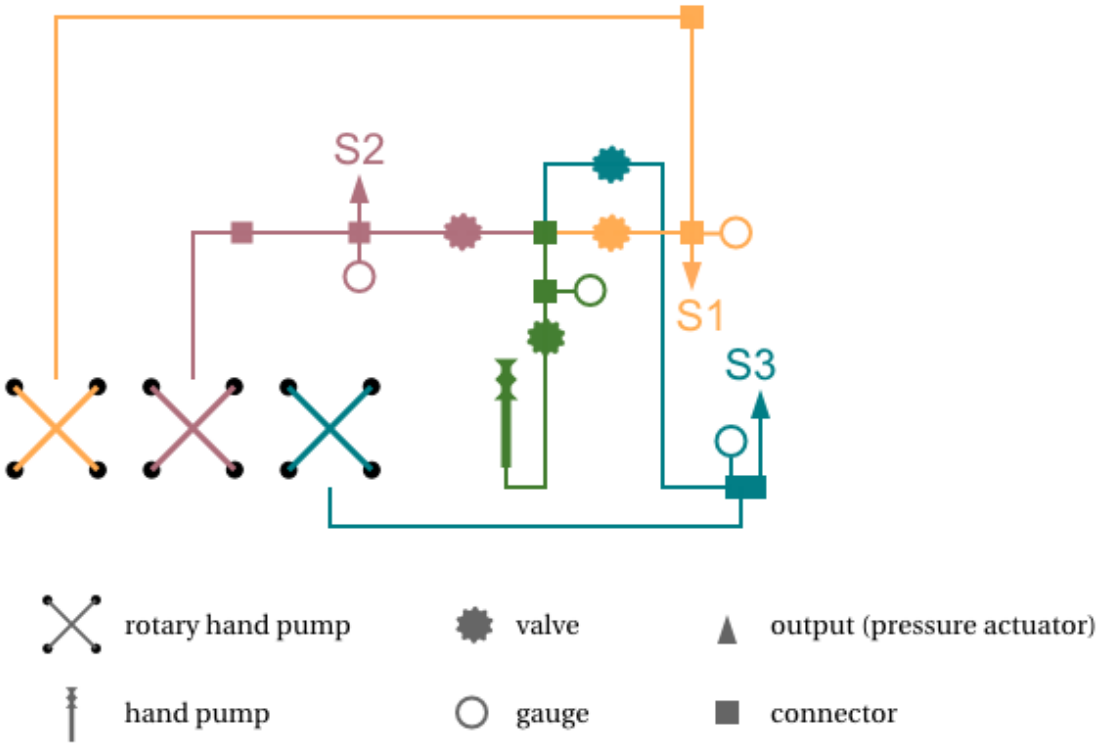

Fig. 6-9. Hydraulic system after modifications.

6.4. Initial tests of the apparatus

The very first step towards reliable experimental results was to carry out initial tests on standard cubic samples made with aluminium and PEEK, and to determine an error limit characteristic for the apparatus. Initial tests carried out in the true triaxial conditions, according to a very plain stress paths, as the one presented in fig. (6-10), aroused suspicion that the measuring setup does not function correctly.

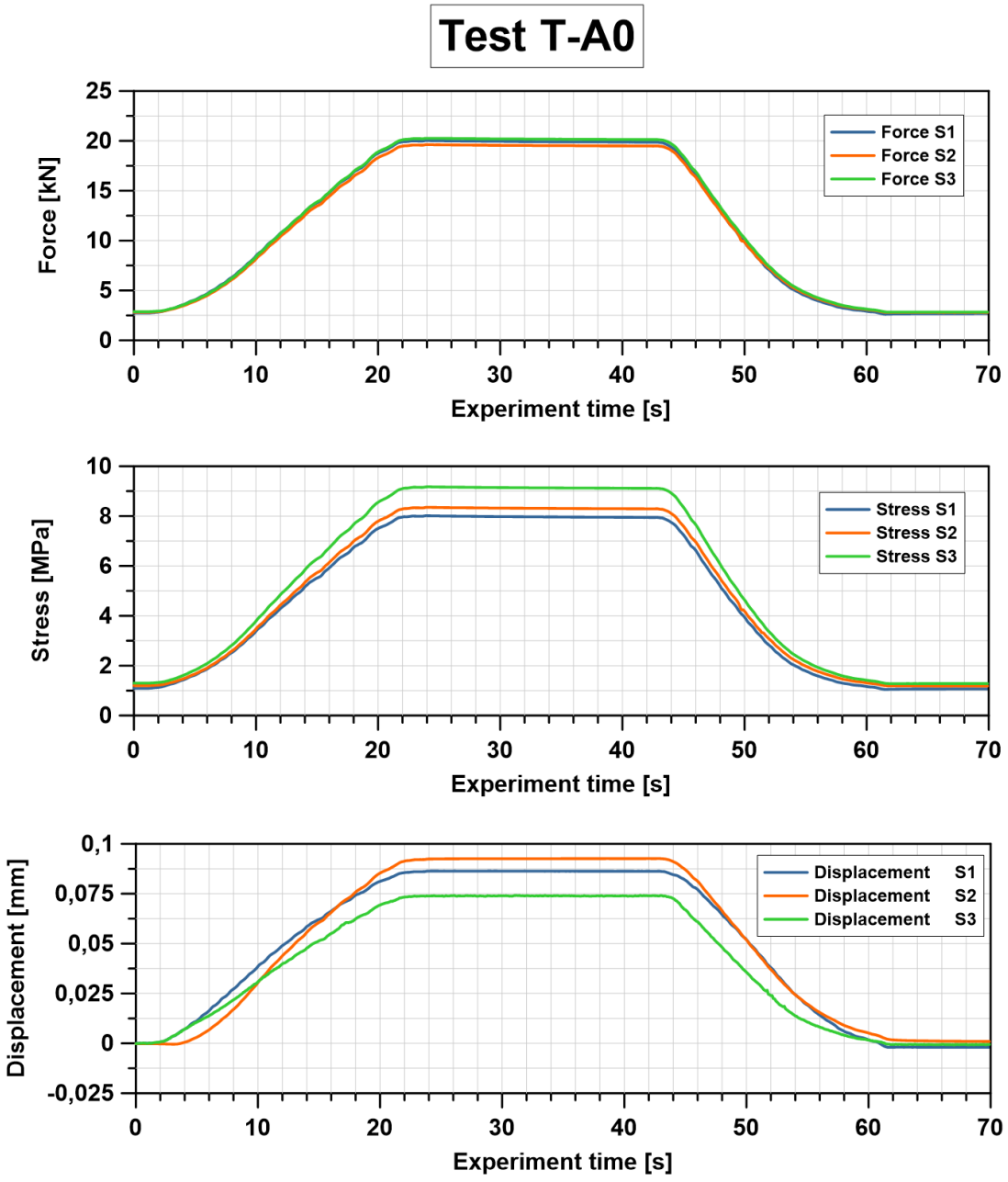

Fig. 6-10. True triaxial initial test.

Test T-A0 was conducted in conditions of equal forces exerted by the actuators on SP2 holders. As the face platens attached to the holders differ in size, it was expected that the resultant stress experienced by the sample would be varying depending on the axis, which could affect the value of strain in particular directions. Surprisingly there was no correlation between the theoretically calculated stresses (according to the platens surfaces) and the readings of the displacement sensors. In order to identify the source of this behaviour more detailed test had been initiated.

At first, both samples were tested in conditions of uniaxial compaction in terms of deformation along the axis parallel to the stress direction. In between the measurements (54 in overall) the samples were rotated, and LVDTs and their holders were exchanged, which aimed for identification of errors originating from these elements. The magnitudes of discrepancies were noted and compared to identify the most prominent error source. The described arrangement was schematically depicted in fig. (6-11).

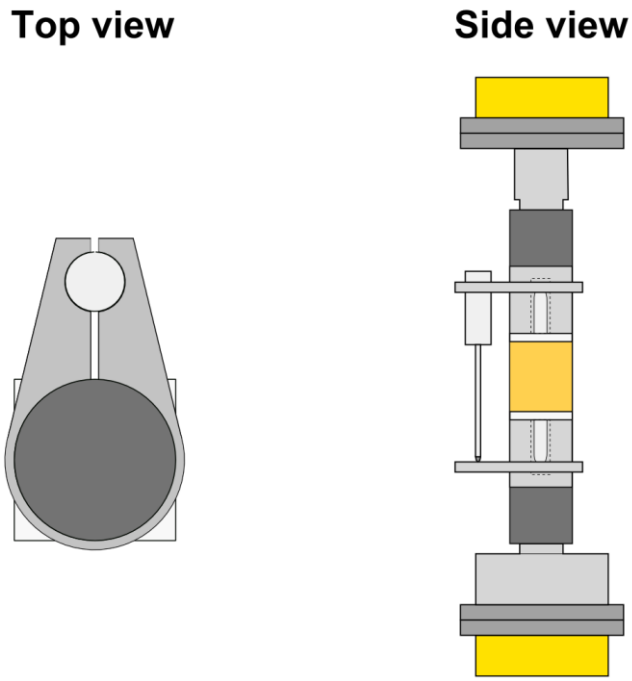

Fig. 6-11. Uniaxial measurement setup.

The results showed large discrepancies depending on the number of experiment repetitions (within the force limits where anelastic deformations were not expected), SP2 holders selection and sensor positioning. Some of the most distinctive tests are presented in fig (6-12).

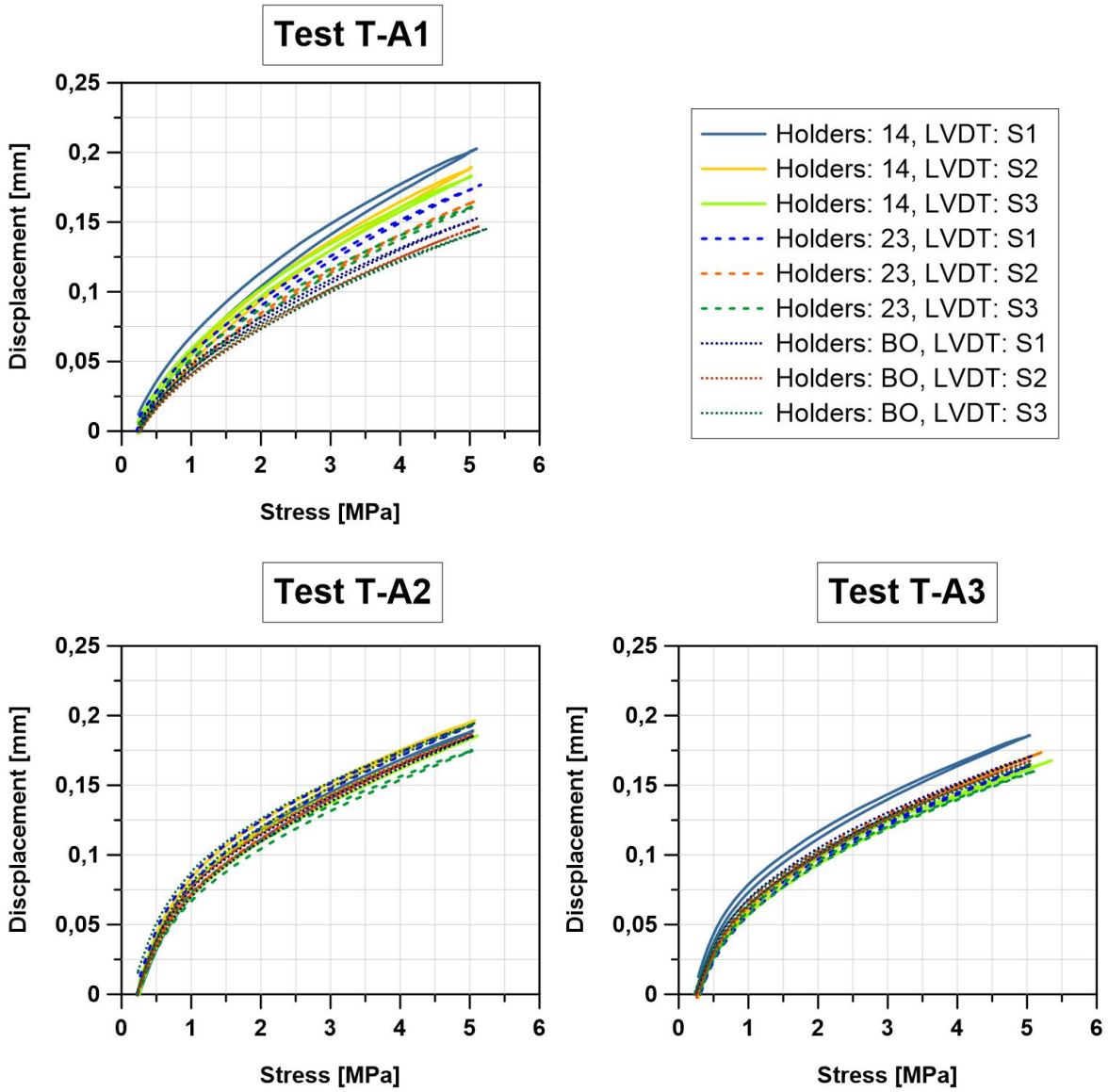

Fig. 6-12. Uniaxial tests of PEEK standard sample. Holders were marked with numbers from 1 to 4, and B and O letters indicating originally corresponding force actuator, whereas the LVDTs symbols refer to a originally corresponding axis of measurement.

In the plot representing test T-A1, being the very first test in the entire series, it is clearly visible that displacement magnitudes were changing from one measurement to another. As the maxima were decreasing with each test it was possible to relate this effect with deformation of a teflon foil used as a bedding between the face platens and the samples. Before further tests, the foil was exposed to a long term stress in order to ensure full development of the creeping effect. Furthermore, the order of measurements of particular holder-sensor combinations was being changed to eliminate any other time-related effects, which could affect the results. In test T-A2, the differences between the measurements are

significantly less pronounced, although some discrepancies are still present – the values of displacement obtained for stress of *5 MPa* have a standard deviation of *0.0062 mm* from an average of *0.187 mm*. In the last of the presented plots, T-A3, one of the measurement (Holders:14, LVDT:S1) differs significantly from the others in this measuring series, which could be most likely explained by a random disturbance of the system during the sensors and holders exchange. The value of standard deviation in test T-A3 is still relatively low (*0.0076 mm*). More importantly, the average of the sensor reading for a stress of *5 MPa* is lower by more than *10%* (*0.168 mm*) than in test T-A2, although the measurements were taken in theoretically identical conditions. This results suggested that there may be some additional effects related to the location of the sensor (which during an individual measurement series was installed in the same place in relation to the tested cube) and sample alignment.

To verify and possibly specify the above conclusions, another round of uniaxial measurements was carried out with three LVDTs mounted on the tested column, as shown in fig. (6-13). The increased number of sensors aimed to capture any possible heterogeneity in the sample behaviour, and additionally establish a reliable force-stress function for each pair of contact platens.

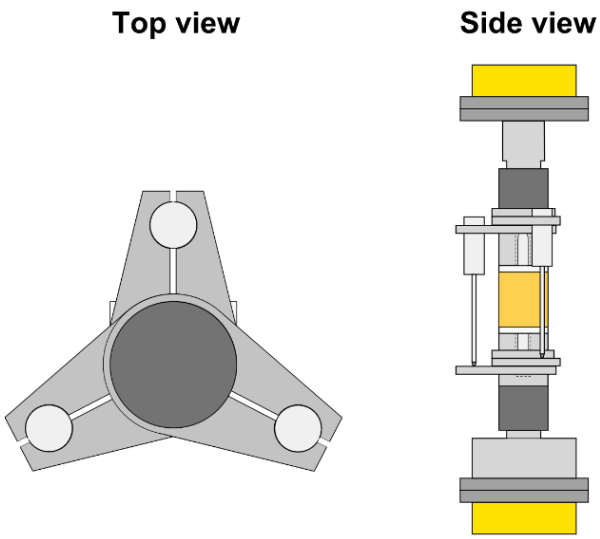

Fig. 6-13. Uniaxial test with three LVDTs.

Some of the most distinctive results (from 13 tests in overall) are presented in fig. (6-14). The measurements revealed significant variations in the sample behaviour, changing from one part of the sample to another.

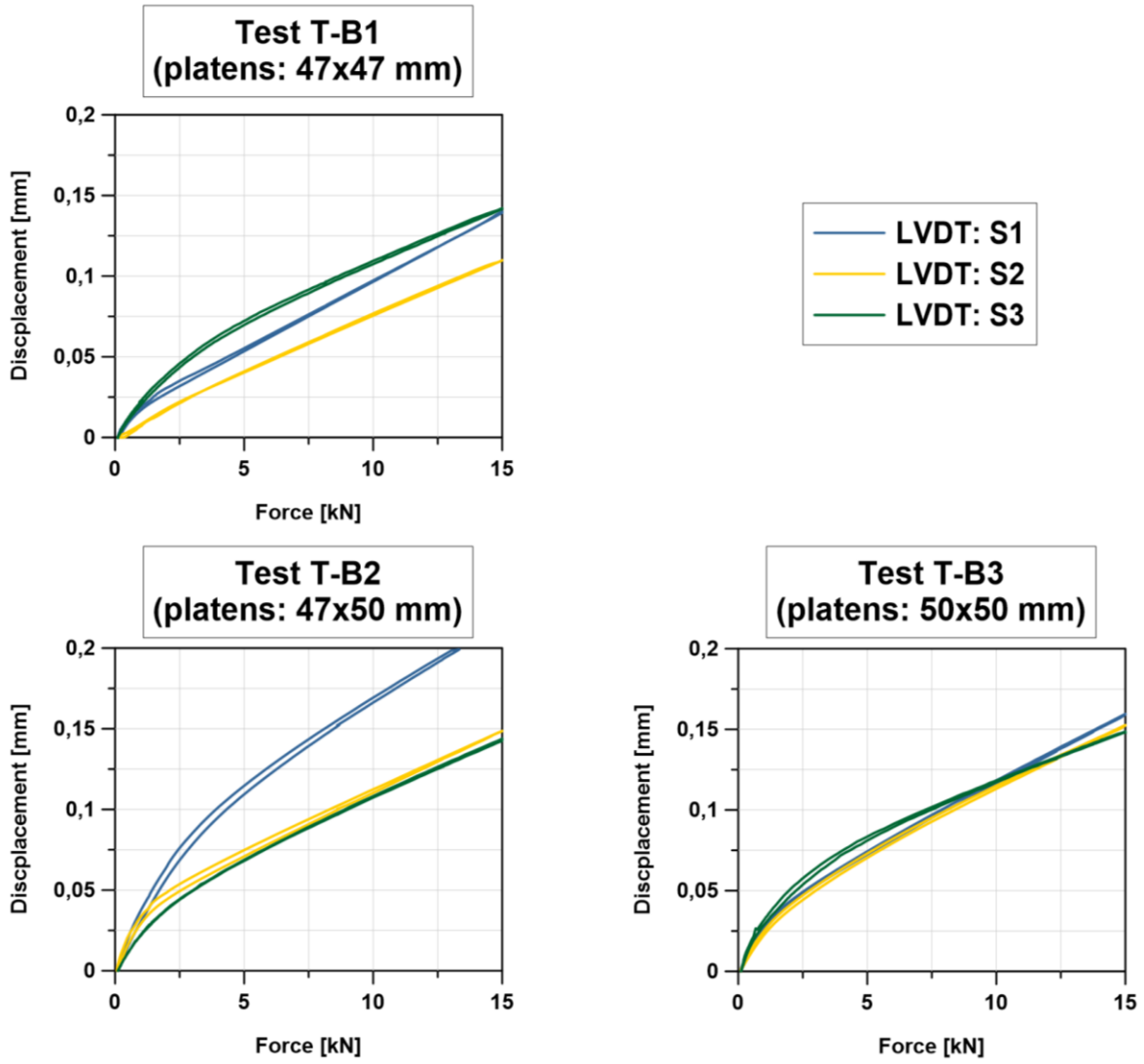

Fig. 6-14. Uniaxial tests of PEEK standard sample with use of three LVDTs simultaneously.

Average values of displacement (for force of *15 kN*) and their average standard deviations are presented in table 6-1. The tests, carried out using a pair of the intermediate (in terms of dimensions, *47x50 mm*) platens, are characterised with the highest standard deviation, followed by the results obtained with a pair of the smallest ones. The biggest platens, the only ones that cover the entire surface of the sample, provide the most homogeneous results, suggesting the most uniform stress exertion. At the early stage of compression the deformation of the system was not linear in relation to the exerted force. This range of non-linearity differs for each of the sensors suggesting that not only the sample compressed, but there were also another heterogenous factors contributing to the shortening of the column, such as sample rotation, contact improvement, etc. Computation of the average values of displacement (giving an estimate of strains, and therefore allowing to approximate

the stresses exerted by the platens on a sample) provided interesting, but highly unexpected results.

Table 6-1. Processed results of the uniaxial test with simultaneous use of three LVDTs.

Platens size [mm]	**47 x 47**	**47 x 50**	**50 x 50**
Average displacement [mm]	**0,132**	**0,168**	**0,155**
Average standard deviation of displacement [mm]	**0,015**	**0,036**	**0,011**

As all the readings were taken at the same compressive force level and as the deformation of the sample is assumed to be governed by isotropic form of Hook's law (equation 1), the resultant displacement d(related to strain as $\varepsilon = d/sample\ length$) was expected to be inversely proportional to the surface of the platens s, according to equation (81).

$$\sigma = \frac{F}{s} \tag{80}$$

$$\varepsilon = \frac{F}{Cs} \tag{81}$$

where: $C - stiffness\ coefficient\ (elastic\ moduli), F - force, s - surface.$

The experimental data indicates that the smallest platens produced the smallest strain, while the highest values were observed when the intermediate platens were mounted. This observations stand against equation (81), indicating serious flaws of the measuring system. After a more profound analysis of the data, the most probable causes for this abnormalities within the sample placement subsystem were determined:

- Wrong LVDT calibration;
- Sample-platens misalignment (causing heterogenous compression);
- LVDTs out of the stress axis (causing decrease in measurement accuracy).

For the purpose of defining the main causes standing behind the tests results, calibration of the displacement sensors was carried out again (and proved that the original calibration was correct). A side effect of the tests and the recalibration of the sensors was that

one of the LVDTs was found drifting and had to be replaced with a more modern transducer produced by HBM (which required an additional adapter H2 – APPENDIX K). To test the alignment of the system, the PEEK sample was installed into the cube holder (SP1) with FUJI Pressure Measurement Film (two sheets – a colour-forming and a colour-developing layer) in between its walls and the contact platens, as shown in fig (6-15). When exposed to stress, microcapsules on the colour-forming sheet break releasing ink on the underneath developing layer, giving an estimate of the stress value and distribution on a tested surface.

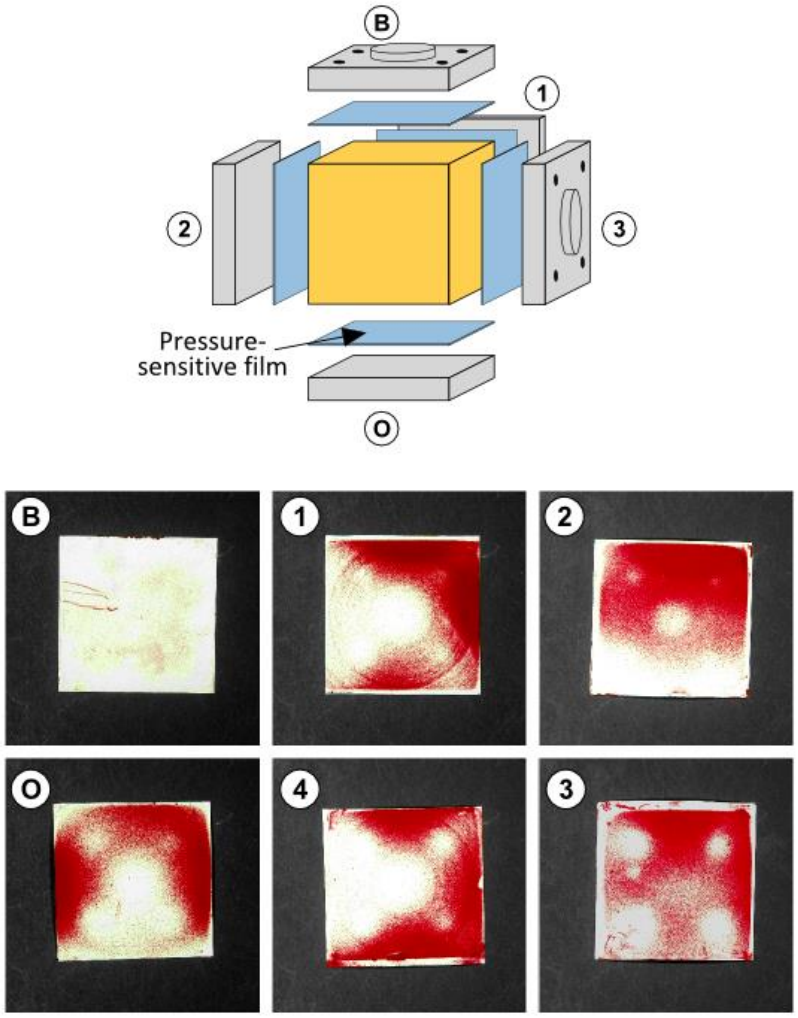

Fig. 6-15. Pressure measurement film placement and test results. Films were marked with numbers from 1 to 4, and B and O letters indicating originally corresponding force actuator.

Performing alignment tests in the true triaxial mode ruled out free-column effects which could have caused system rotation during the uniaxial tests, when sides of the sample were not supported. After introducing the sample into the apparatus, the stress exerted on

the sample was monotonously increased for 2 minutes up to around *7 MPa* (stress estimates were made with use of the load cells readings divided by the surface of the platens), and after reaching that level it was kept constant for another 2 minutes. The colour-developing sheets used in the test are presented in fig (6-15).

As observed in the pressure-sensitive film images, stress distribution within the system was highly uneven. All the films (apart from film B, which will be discussed later) bear similar ink pattern. In the central part of the films, there is a blank circular area corresponding to an empty space created by the acoustic sensor bed located in the centre of the steel holders (SP2). Blank spots observable on the diagonals of the films, in between the central point and their corners, result from the presence of M5 screw threads used to attach the platens to the holders. In addition, each of the films reveal weakly painted zones not related to the features of the platens. Left side of sheets 1 and 4, as well as the bottom parts of films 2 and 3, indicate hardly any effects of pressure, which is a direct evidence of sample-to-platens misalignment. The vertical axis (films B and O), despite being tested with only one correctly developed film, indicates an irregular stress distribution likewise (faulty development of the film was caused by incorrect placement of the colour-forming sheet). According to the colour scale included in the instruction, the stress experienced by different regions of the platens may be extremely different, below *2.5 MPa* in the weakly coloured areas and exceeding *10 MPa* in the strongly painted ones. There were no attempts to repeat the test, as even partial results confirmed serious misalignment of the measurement system.

Any possible errors introduced by misalignment could have a significant impact on the reliability of the experimental results. Due to highly uneven force distribution, it would be almost impossible to determine average stress experienced by the sample, which is used as a parameter in rock model. Furthermore, the true triaxial apparatus design allows to install only one LVDT per axis, and therefore, in case of large stress heterogeneity, there would be no means to determine the error value and a discrepancies range. Consequently, displacement measurement would not provide reliable value of strain, making it impossible to correct the acoustic measurement results for sample shortening and to test experimental results against the strain-based rock models. In the face of strong evidence of serious flaws of the measuring system, a decision to postpone tests on rock samples was made until solving the alignment-related problems.

The most obvious countermeasure to any possible deviation of the LVDTs from the measurement axis would be to replace them with strain gauges attached directly to

the sample. Unfortunately, this is impossible as the face platens are in contact with most of the sample surface. In order to limit the LVDT misalignment effects, a new set of sensor holders (SP3) was manufactured. They are characterised with larger contact surface between the acoustic transducer holder (SP2) and the displacement sensor which should allow to limit LVDT deviations. The comparison of the original and the modified set is presented in fig. (6-16). More detailed plans can be found in APPENDIX J .

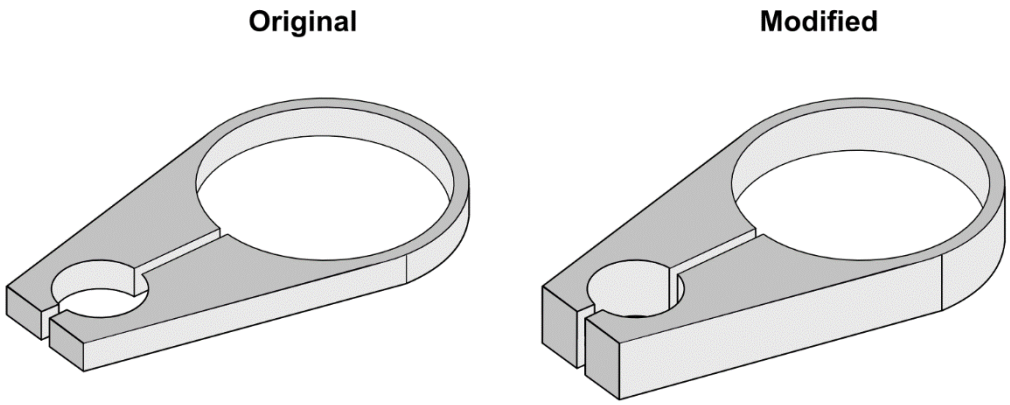

Fig. 6-16. Original and modified LVDT holder (element H1).

6.5. Sample placement system (elements SP1-4) modification

In order to minimise the misalignment effects, it was decided to redesign the sample positioning system, so that it was adapted to a new set of six identical contact platens instead of previously used three pairs of different dimensions. The new platens dimensions were perfectly matching the size of a sample (*50 x 50 mm*), which made it easier to evaluate placement accuracy and alignment before starting the test. Moreover, the modification removed free space between the platens and SP1 frame elements, and accordingly decreased chances of platens rotation during sample placement in the apparatus. In addition, using one set of platens of the same dimensions made it possible to establish an unique, more reliable force-to-stress function. To allow the system to accommodate during sample contraction, the edges of the platens were cut off, as shown in fig (6-17). In order to decrease the acoustic impedance contrast between the platens and samples, and therefore boost amount of wave energy transmitted from the transducer to the cube, another set of platens was manufactured with PEEK. Detailed drawings of the described parts can be found in APPENDIX H .

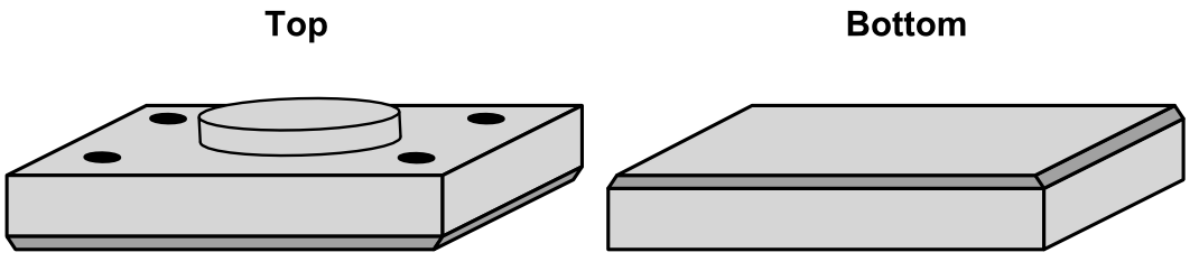

Fig. 6-17. Platens (SP3) with cut off edges to accommodate sample contraction.

New SP1 aluminium frame had to be manufactured. In order to adjust it to the uniform size of the platens, its internal construction was slightly simplified. Internal dimensions of the original frame were adjusted to the radius of SP2 transducer holders and in the direct proximity of the sample were regulated by additional limiting elements, responsible for reducing displacement and rotation of the platens. Using six platens of the same dimensions, matching both, the sample and the acoustic transducer holders size, allowed to remove all the limiting elements. External dimensions and features were kept exactly as in the original design. Technical drawings of the new frame elements can be found in APPENDIX G .

At first, the new frame was tested according to a procedure similar to the one used in test T-A0. In order to minimize sheer stresses and make it easier for the cube to adjust its position to the system elements, the PEEK sample was wetted with paraffin to facilitate slipping (Dillen et al., 1999). It was later covered with teflon foil and placed inside the aluminium frame SP1 with more paraffin in between the foil and the face platens. During mounting, all elements of the new sample positioning system seemed to fit almost perfectly, leaving no space for platens to rotate. At the same time it was possible to move the cylinders SP2 back and forth, which made it easier for the system to adapt to exerted force during mounting. The frame was placed in the central position of the apparatus using an additional aluminium bar. Circular markings were made on the outer contact surface of SP2 cylinders in order to facilitate their proper placement in relation to the hydraulic actuators. In consequence, the risk of misalignment between the main frame of the apparatus and the sample positioning system was reduced. Before dismantling SP1 frame, the system was first kept under pressure of 0.5 MPa for about half of hour. Between dismemberment of the frame and initiation of the main part of the test, the hydrostatic stress was increased up to 2 MPa and decreased back to 0.5 MPa several times, allowing the cube to adjust its

position (schematically presented in fig. 6-18). Results of one of the first tests carried out with the use of SP1 frame are shown in fig. (6-19).

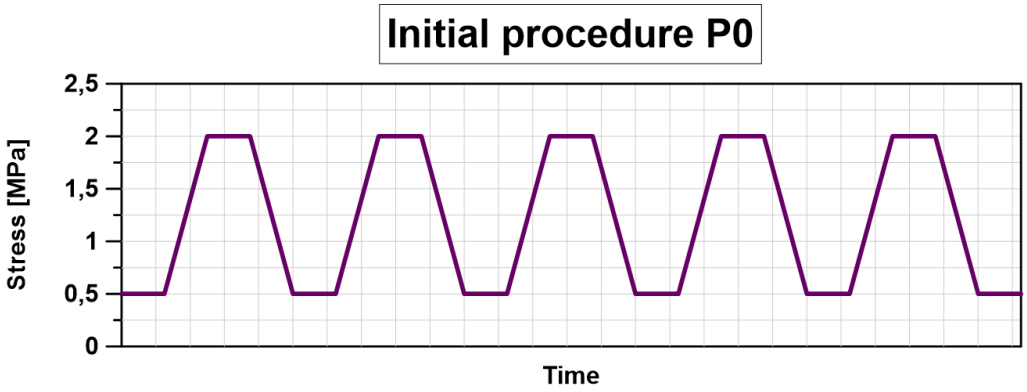

Fig. 6-18. Procedure for sample stabilization.

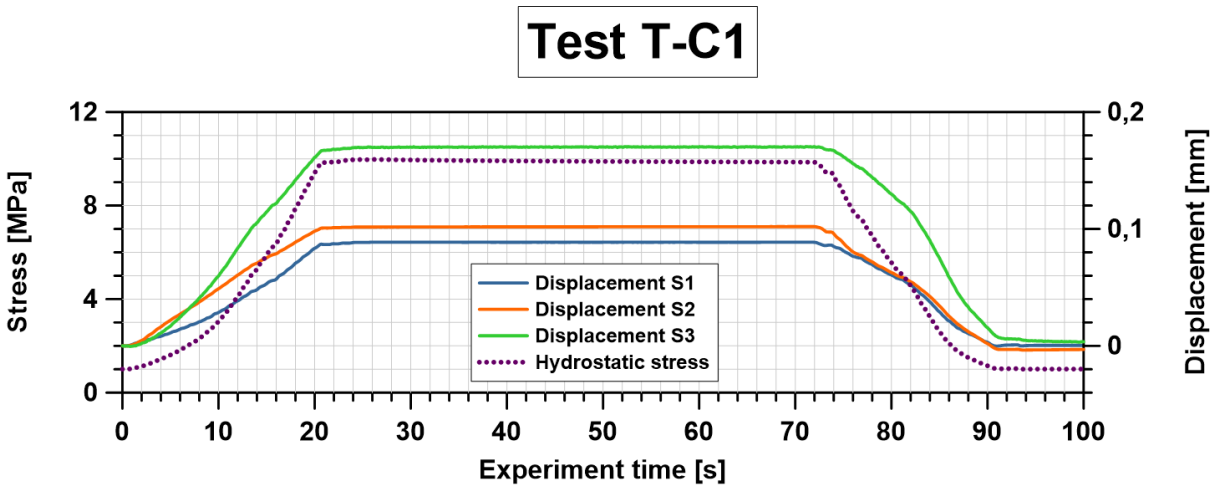

Fig. 6-19. True triaxial test - new SP1 frame.

As the platens were of the same size, and therefore the force-stress relation was assumed to be identical for all of them, only one stress function was plotted. It is clearly visible that the displacements differ significantly from one axis to another. The difference between the readings of LVDTs installed along S1 and S3 axes reaches 48% under hydrostatic stress of 10 MPa (0.089 and 0.170 mm, respectively). The results came as a surprise, as the frame and the face platens should have limited alignment-related problems within the sample placement system; therefore, the reading had been expected to be more uniform in comparison with the previous tests. To rule out some of the time-related effects, the sample was kept inside the apparatus under pressure of around 3 MPa (it was slightly changing due to a leak in the hydraulic system) for almost 16 hours before further tests. It was assumed

that the sample may have had not enough time to equilibrate within the system before the previous tests and it was still tilted in relation to the face platens – leaving it for a long time under stress, with all surfaces covered with a film of paraffin, may have solved the problem. The results of the repeated test are shown in fig. (6-20). In the repeated tests the difference between the readings was slightly limited (down to 42%), but still could not be taken as satisfactory.

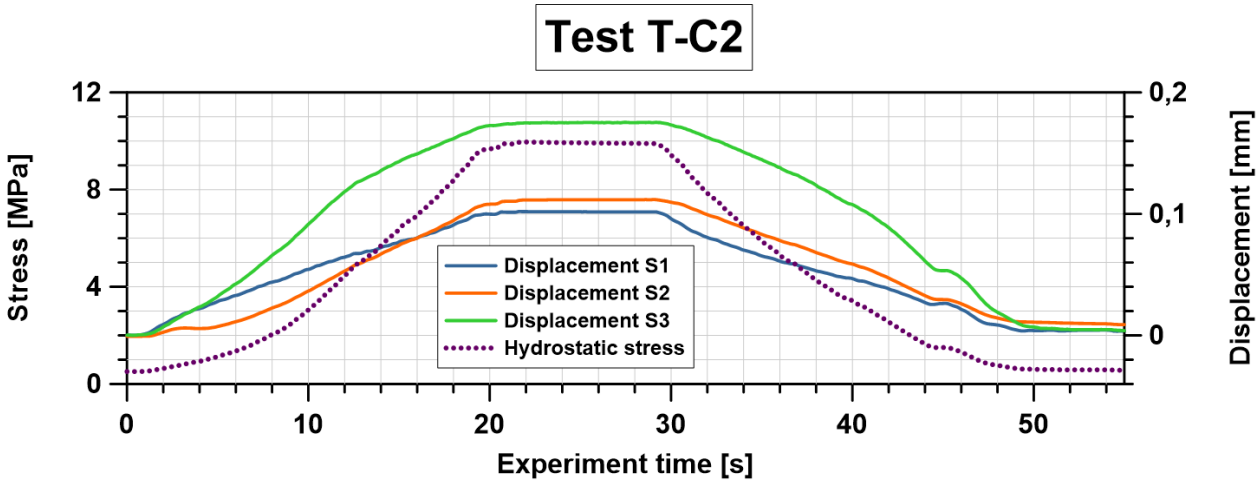

Fig. 6-20.True triaxial test - new SP1 frame (repeated after 16 hours).

In the light of the above results, the decision to carry out more advanced analysis of deformation along only one of the axes under hydrostatic stress conditions was made. The tests procedure was similar to the one used in tests T-B1, T-B2 and T-B3. In this case the free-column effects should not be present – the test was performed with all three sets of the SP2 cylinders in contact with actuators, exerting pressure on the sample from all directions. The main point of the measurements was to determine if the sample exposed to hydrostatic stress is deforming uniformly in particular directions. Hence, it could be determined whether the discrepancies observed in the previous tests were related to unequal stresses on the particular axes. Else, if the sample was deforming heterogeneously along one axis and the readings were dependent on the placement of the sensor, it would mean that the observed displacement values are not representative, and should not be directly used to describe the behaviour of the sample. After minor modifications of the LVDT holders, the transducers were installed on SP2 cylinders on S3 axis. The measurements were preceded by the procedure P0 presented in fig. (6-18). Between the tests, the sample was not removed from the system, but positioning of the LVTDs was changed, so that the results could be matched both to the transducer itself and to the transducer location. A simplified apparatus

drawing with marked LVDTs placement positions is shown in fig. (6-21).The results are shown in fig. (6-22).

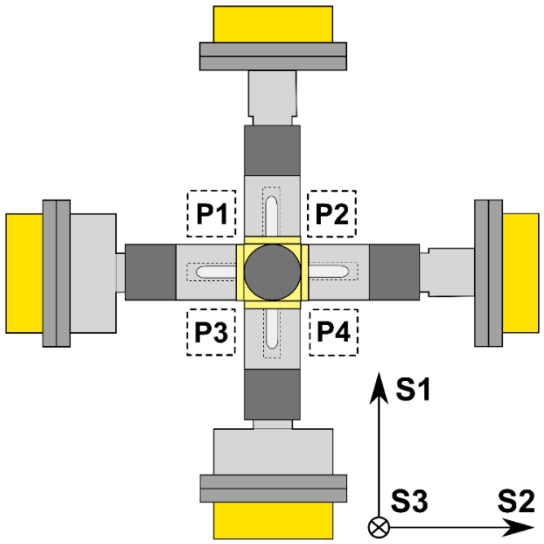

Fig. 6-21. LVDTs localization during tests T-D1, T-D2 and T-D3 (positions 1-4).

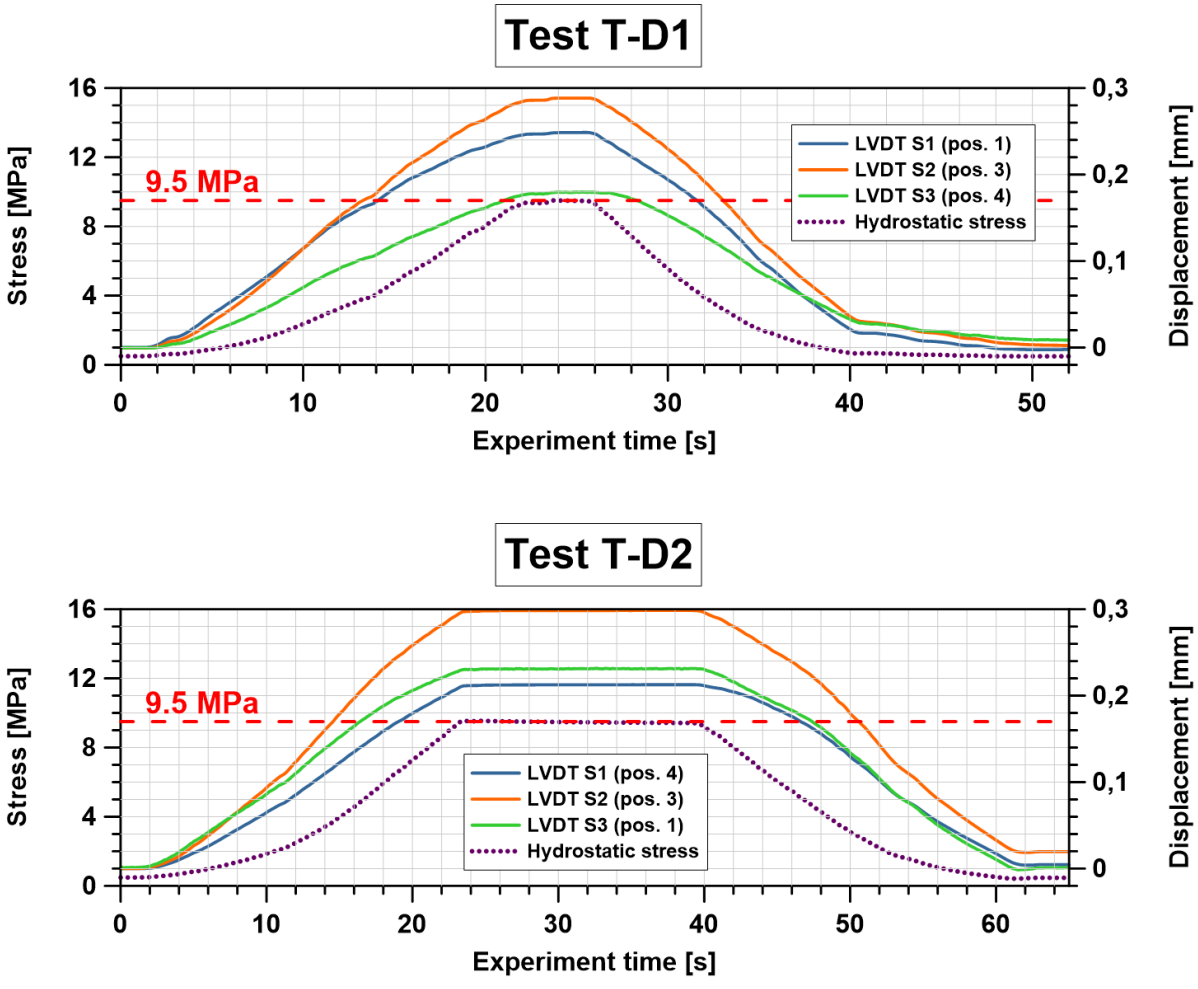

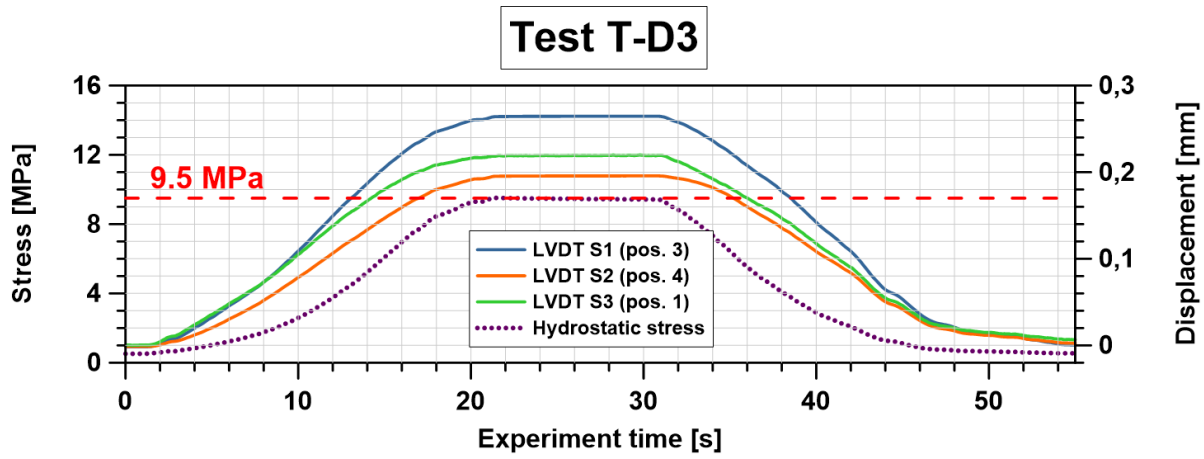

Fig. 6-22. True triaxial tests – new SP1 frame (all LVDTs on S3 axis).

All the readings from T-D measurement series, are characterised by clearly visible heterogeneity in the recorded system behaviour. Although the sample was always exposed to the same maximum stress, the highest value of displacement is changing for each of the sensor positions. The recorded deformations of the system along S3 axis tend to get closer to their average with each further test (standard deviation of the maximum values given by the LVDTs decreases – *0.055, 0.045* and *0.035,* respectively).

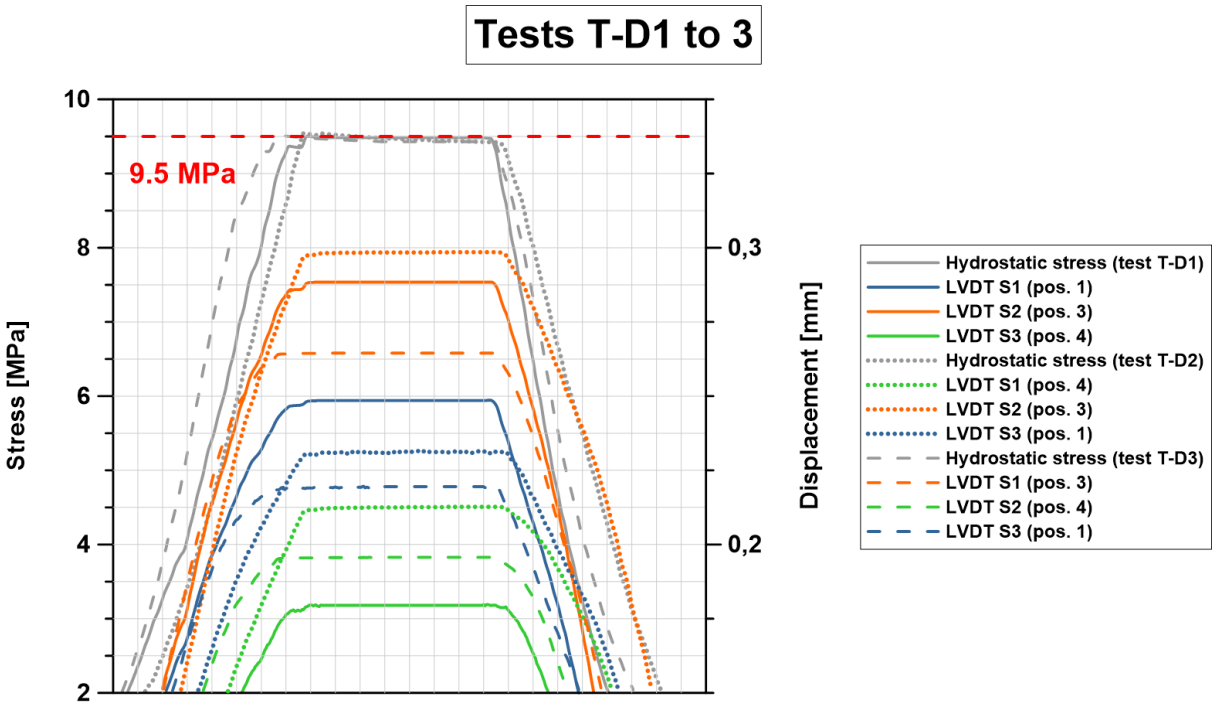

Fig. 6-23. Cumulative plot of T-D test series (colour code: blue – LVDT position 1, orange – LVDT position 2, green – LVDT position 4)..

As repeated loading of rock samples could introduce changes in their internal composition, it should not be treated as a possible sample stabilizing procedure. To visualise more clearly the recorded behaviour of the system as a function of the LVDT position, a cumulative plot was made (fig. 6-23). In order to make the comparison clearer, time relations between the measurements were not preserved (the results were scaled horizontally). Moreover, the colours were set to match the position of the LVDT and not the sensor itself. As observed in the cumulative plot, the character of deformation of the system is repetitive. It may suggest that this behaviour does not result from random fluctuations – it may be caused by sample placement, system misalignment or uneven stress distribution on the contact between the sample and the face platens. In order to discriminate possible sources of discrepancies, the LVDT-based measurements were supported with yet another employment of the stress-sensitive film. The measurement procedure is exactly the same as the one used in the previous test with FUJI film. The resulting images, spatially organized to recreate the PEEK cube (markers indicate corresponding SP2 holders), are presented in fig. (6-24).

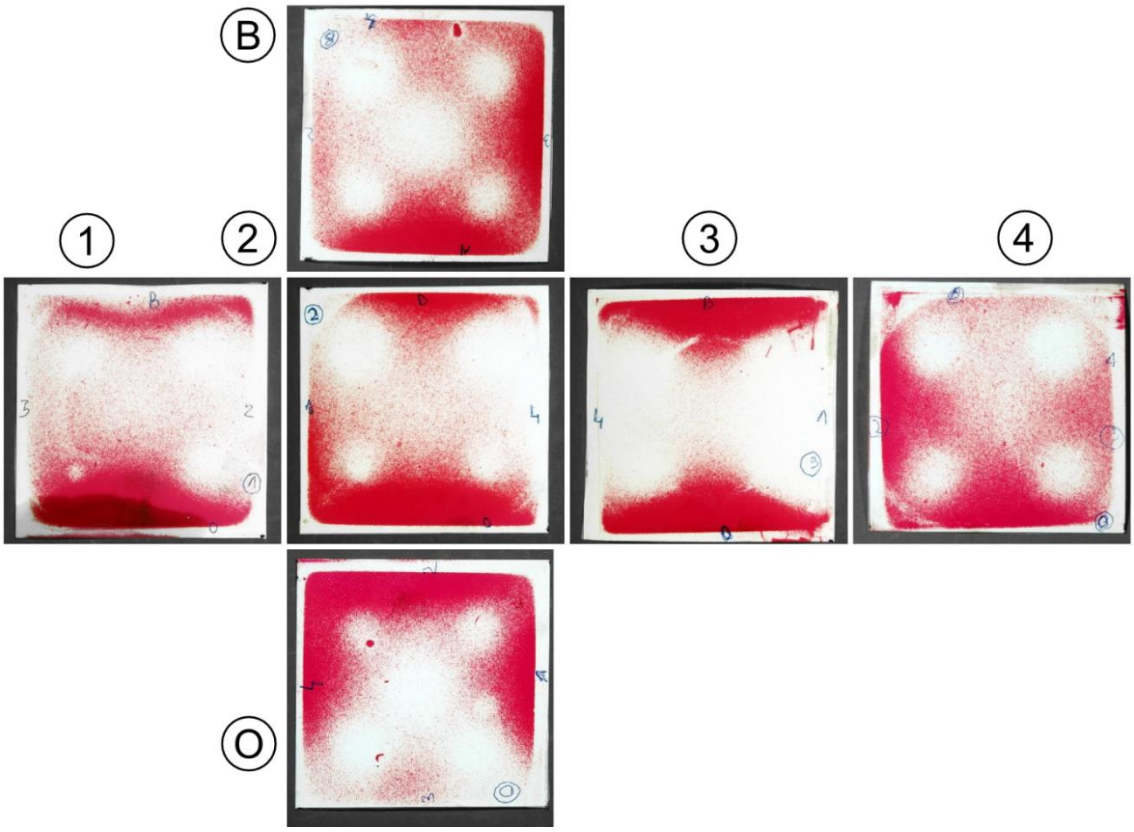

Fig. 6-24. Stress-sensitive film after true-triaxial test.

The results, compared with the previously obtained images, indicate more uniform stress distribution. Platens 1 and 3 are exceptions, as the films show that in their case stress was concentrated mostly close to the upper and lower edges. Having in mind that the intensive red colour indicates stresses of around 10 MPa and white of less than 2 MPa, it may be concluded that this irregularity can be responsible for the observed uneven sample deformation. All the platens were initially treated with very fine sandpaper (P1200), as they were assumed to have been flattened during manufacturing. After closer inspection of the contact surfaces of new SP3 elements (especially number 1 and 3), it was decided to polish them once more with the use of coarser sandpaper (P300 and P600) in order to remove larger irregularities. This time, the lower part of an SP2 cylinder was attached to the platens to provide some additional weight and to lower the centre of gravity preventing tilting. During polishing, minor manufacturing flaws were spotted (platens were locally melted, which could result from using high-speed milling tool) and were partially removed.

An attempt to test each set of SP3 platens and SP2 cylinders separately before and after polishing in a MTS uniaxial load frame was made, but the results indicated that the frame itself introduces an additional error. Face platens of the uniaxial frame exerted force heterogeneously – it could be concluded that the initial heterogeneities propagated into measurements carried out with PEEK sample alone, with a set of SP2 holder and with SP3 platen as shown in fig. (6-25). Observed disparity should not affect smaller cylindric samples usually tested in the machine, but made it impossible to draw unambiguous conclusions about the quality of platens surfaces, as the stress was distributed mostly on the edges of the SP2 cylinders and it was very likely to cause a slight tilt of all elements. Eventually, the platens were checked with the use of a calliper, as there were no more non-invasive testing tools available.

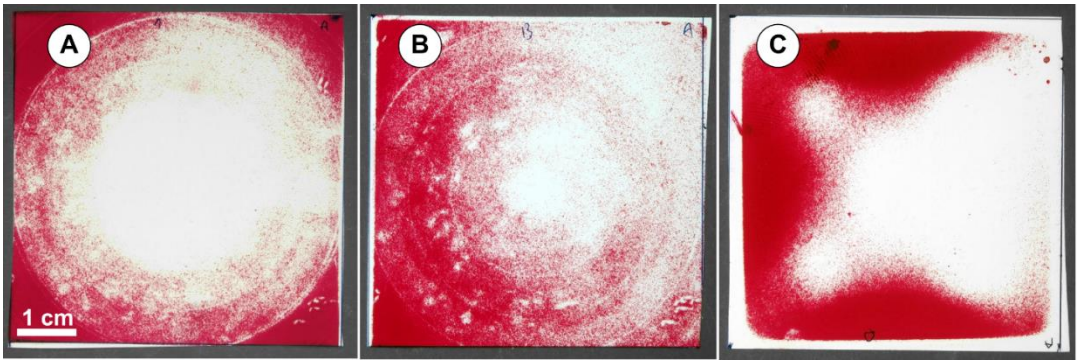

Fig. 6-25. Stress-sensitive film - tests performed on MTS uniaxial load frame. A - MTS frame built-in upper face platen against lower face platen, B - MTS frame built-in upper face platen against PEEK sample, C - SP3 platen against PEEK sample.

As a means to increase measurement reliability, there were further changes made in the true triaxial apparatus and the measurement procedure. Misalignment of the sample placement system in relation to the outer frame and the hydraulic actuators was identified as yet another of the possible factors causing heterogeneous behaviour of the sample. So far, the contact between SP2 holders and the actuators could not be precisely controlled, and therefore there could be some deviations of the centre of the contact area from the centre of the holders. This could cause uneven force exertion and tilting of the holders, introducing further heterogeneities in stress distribution within the system and provoke uneven deformations of the sample. Hence, in order to promote more precise and repetitive positioning of the SP2 holders and the force actuators, additional aluminium rings were inserted in the contact area (shown in fig. (6-26) and in more detail in APPENDIX I).

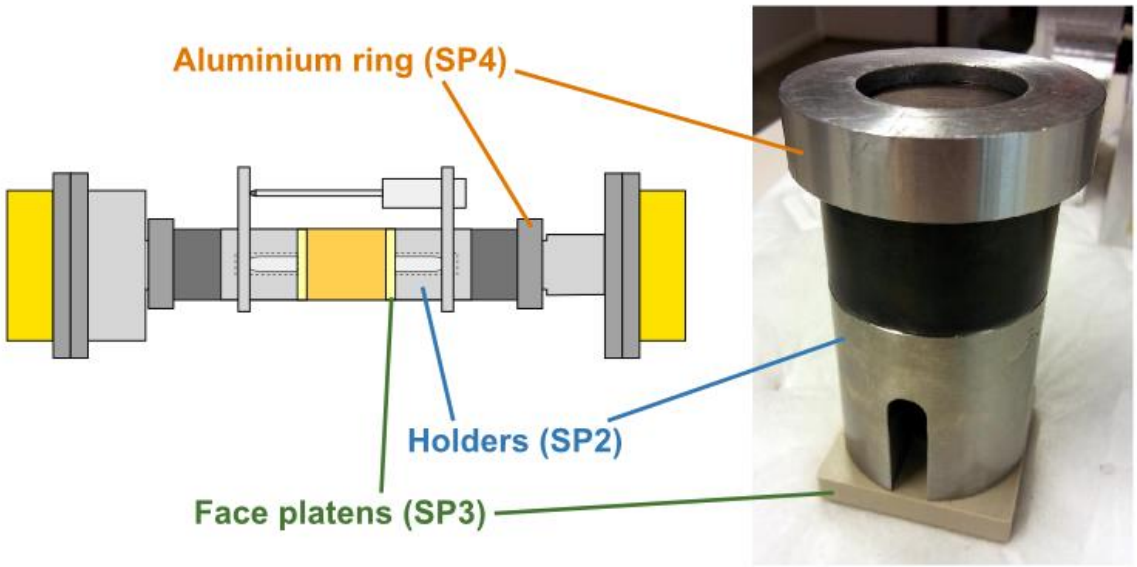

Fig. 6-26. Aluminium ring (SP4) installed on the SP2 holder.

Radii of the bigger and the smaller holes in the rings match the dimensions of the holder and the actuator endings, respectively. The rings work both as a “sighting” device and a guideway for the endings of the actuators, which move through the smaller hole on the top of the rings before making contact with the holder surface. When mounted on all six holders, the rings increase accuracy of positioning of the entire sample placement system significantly. To verify whether polishing and the rings had an impact on the stress distribution, another test with the use of the stress-sensitive film was carried out. Results,

presented in fig. (6-27), indicate more heterogenous stress distribution than observed in the previous tests. The obtained images suggest that surfaces of the platens is significantly smoother – the biggest improvement was observed in films corresponding to platens no. 1 and 3, which finally do not exhibit lack of contact between the central part of the platen and the sample. Furthermore, the stress disturbance zones around the M5 screw threads are significantly smaller than in the previous tests for all platens on the lateral axes (no. 1 – 4). Notwithstanding, heterogeneity of the stress distribution shown by the test was still considered insufficient to provide fully reliable results. Also, the repeated test proved that the melted zones observed during polishing were affecting stress distribution – one of the discoloured spots could be directly associated with an anomaly marked on the film from platen no.3. However, the anomaly is relatively small, and therefore should not have significant impact on sample loading.

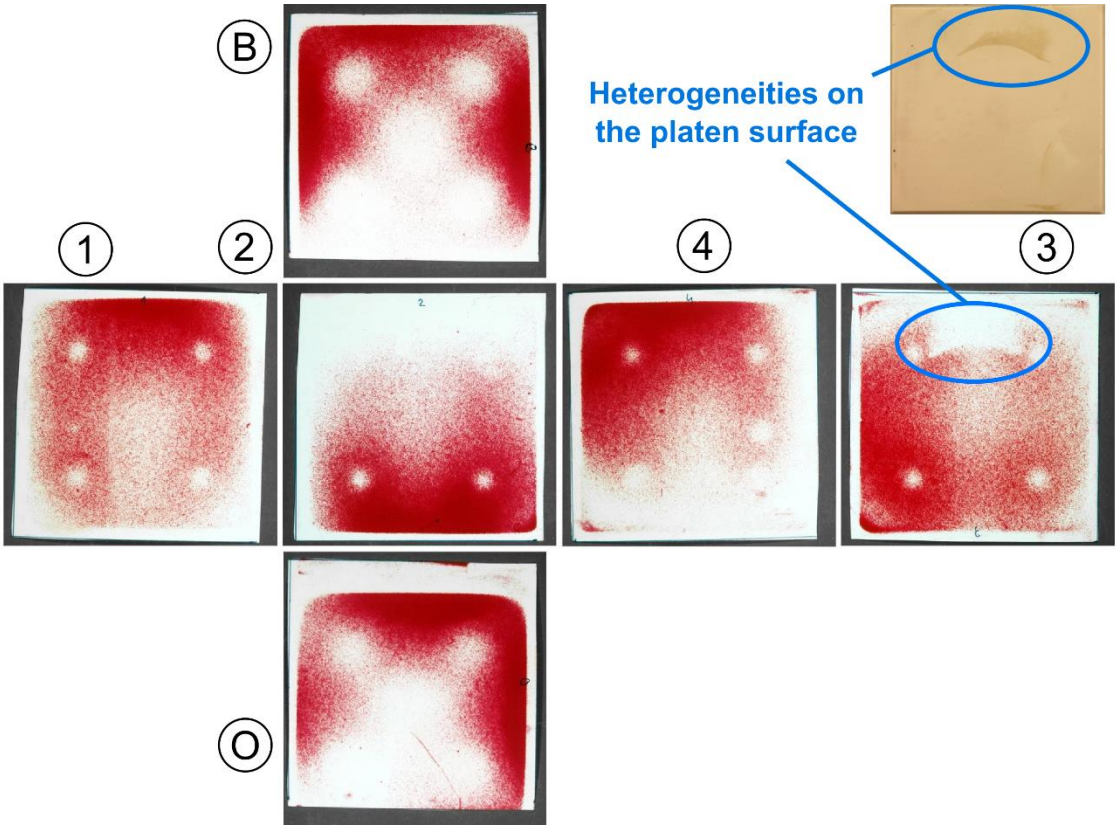

Fig. 6-27. Stress-sensitive film after true-triaxial test (after polishing) and a picture of the surface of face platen no. 3.

Moreover, the measurement procedure was modified according to SINTEF Petroleum Research employees recommendations. It was suggested that stress loading rate could be too high, and might not allow the sample to accommodate to the exerted force. This could introduce additional time-related effects and affect homogeneity of deformation. It is worth noting that the procedure described by the stress-sensitive film producer assumed high stress loading rate - in case of slower stress increment those irregularities may not be so pronounced and the stress distribution may be much closer to heterogeneous (than indicated by the developed films). Therefore, in the further tests loading was applied at a constant rate of 0.05 MPa/min. This value results from a trade-off between giving providing more time to accommodate and necessity to operate the hydraulic pumps manually during the entire procedure, which makes longer tests burdensome.

The first presented test, T-E1 shown in fig. (6-28), was performed with LVDTs on each of the apparatus axes. During the test, the cubic PEEK sample was loaded up to 10 MPa. From the very beginning of the test, heterogenous behaviour of the sample is well visible. Two of the LVDTs, S1 and S3, indicate almost identical deformation character in response to the hydrostatic pressure applied to the sample. Initially steep curve, probably due to closing of empty space in between the apparatus elements, gradually flattens out. From the stress value of 3 MPa, stress-displacement relation registered along S1 and S3 axes is almost linear.

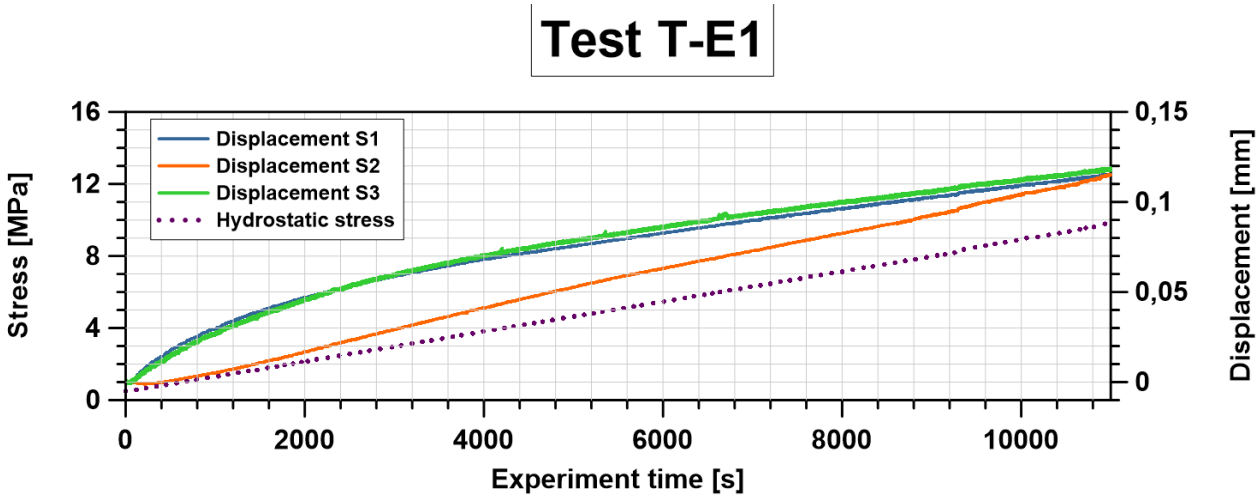

Fig. 6-28.True triaxial test - decreased loading rate.

The sensor installed on S2 axis reacts to the applied stress with certain delay, initially indicating even slight extension of the system. Shortening in this direction starts when hydrostatic stress exceeds 0.3 MPa, and it has approximately linear character up to

the maximum stress value, where its amplitude finally equals the values indicated by S1 and S3 sensors. However, directly after the end of registration of T-E1 test, stress was further increases at much higher rate causing displacement to diverge once again. In order to better visualise the difference in reaction to exerted force, deformation was presented as a function of stress in fig. (6-29). To facilitate comparison of the stress-deformation relations, the displacement along S2 axis was corrected to match the value of the other displacements at the stress value where all of them exhibit linear behaviour. After shifting the curve upwards, it is clear that the sample deforms heterogeneously, but it still remains unknown whether the deformation is uniform or heterogeneous along individual axes, as it was observed in the previous experiments carried out with high loading rate.

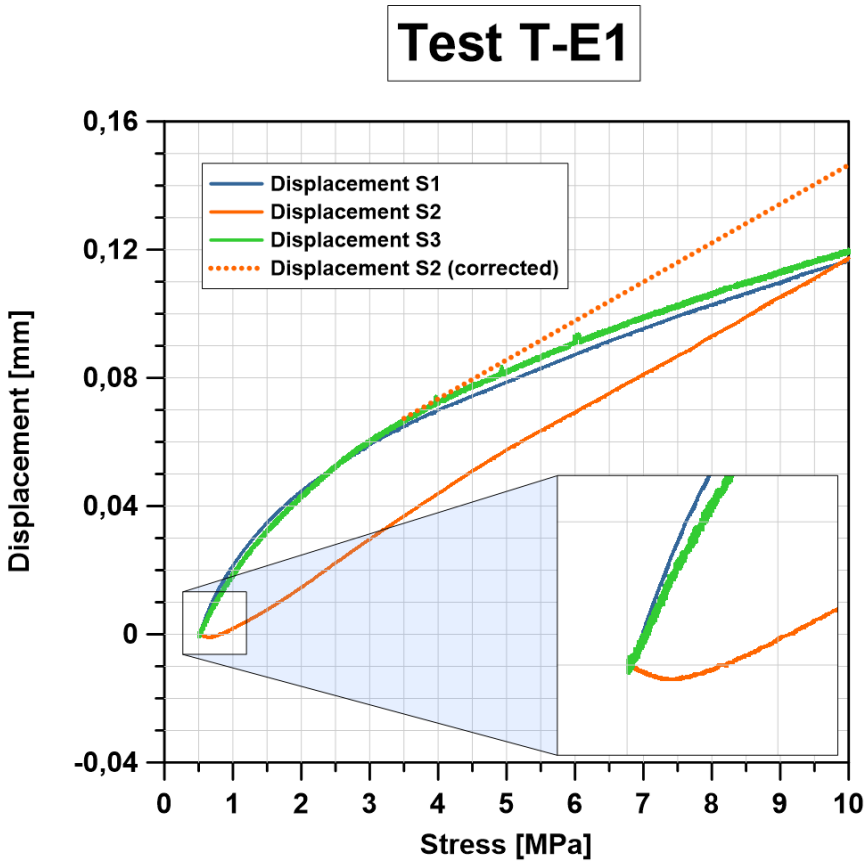

Fig. 6-29. True triaxial test - decreased loading rate & displacement correction.

In order to clarify whether the modifications (face platens polishing, rings and slow loading rate) limited the heterogenous stress distribution, observed as uneven deformation of the sample, another true triaxial experiment was carried out. In between the tests, LVDTs were transferred to S3 axis, but the position of the sample was not changed. Test T-E2, shown

in fig. (6-30), was conducted according to the same outlines as T-E1 in order to recreate deformation of the sample observed in the previous test.

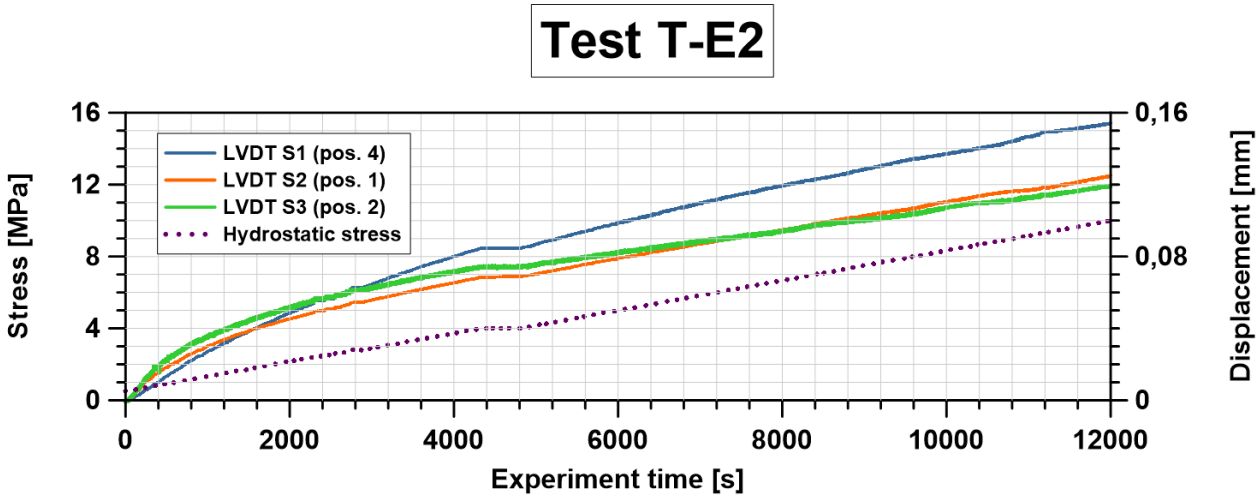

Fig. 6-30. True triaxial test - decreased loading rate (all LVDTs on S3 axis).

An attempt to recreate the conditions was successful as the readings of LVDT S3, which position in relation to the sample was the same during T-E1 and T-E2 tests, are almost identical along the entire loading cycle (as shown in table 6-2).

Table 6-2. LVDT S3 readings comparison (tests T-E1 and T-E2).

Stress [MPa]	**3,73**	**6,66**	**10,0**
Displacement - test T-E1 [mm]	**0,0694**	**0,0963**	**0,1194**
Displacement – test T-E2 [mm]	**0,0718**	**0,0942**	**0,1193**
Difference [%]	**3,45**	**2,27**	**0,08**

In order to remove any possible long-term time effects, test T-E2 was repeated 15 days later. Between the tests, the PEEK sample was kept under pressure of 3 MPa. Combined results of tests T-E2 and T-E3, presented in fig. (6-31), indicate that the discrepancies between the readings are still high, although the amplitude of recorded deformations changed. This effect was probably causes by creeping of the setup elements.

To gain a better insight into time-delayed deformations, loading was stopped at 5.5 MPa and stress was not increased for almost half an hour during T-E3 test. It was assumed that any displacement difference would be a result of creep of the system, and therefore

(if significant) would indicate that the loading rate is still too high for the sample to equilibrate. The recorded displacement amplitude shift was of around *0,0005 mm* for all LVDTs, as shown in fig. (6-32). However, after a more detailed study of the registered stress values it was concluded that the pressure within the system kept changing although the pumps were not used, making the described results questionable.

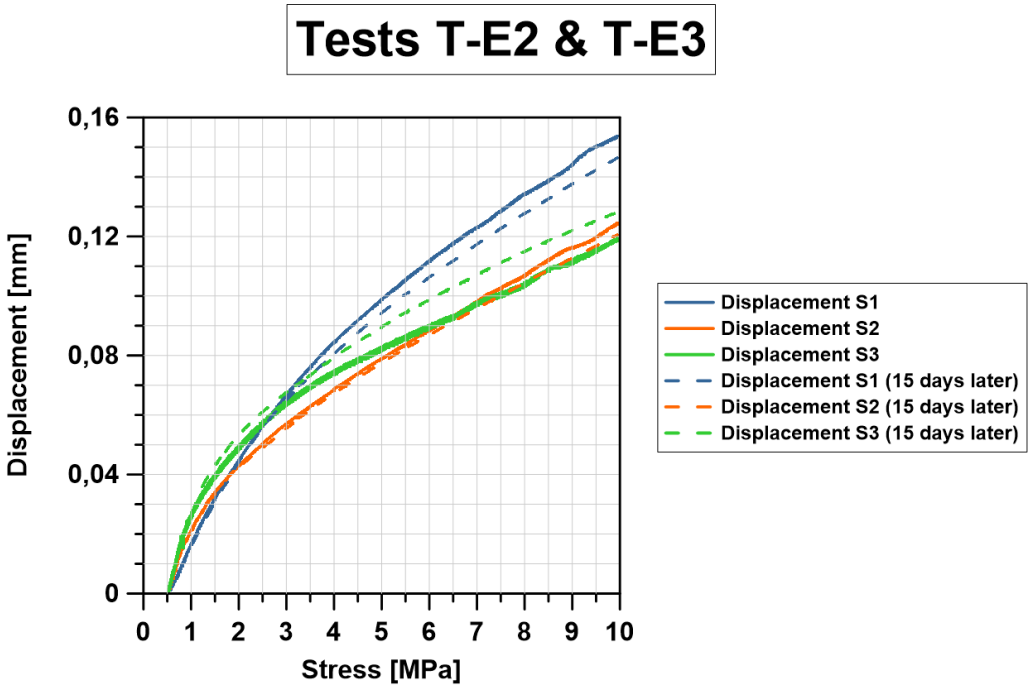

Fig. 6-31. True triaxial tests - comparison of T-E2 and T-E3 tests.

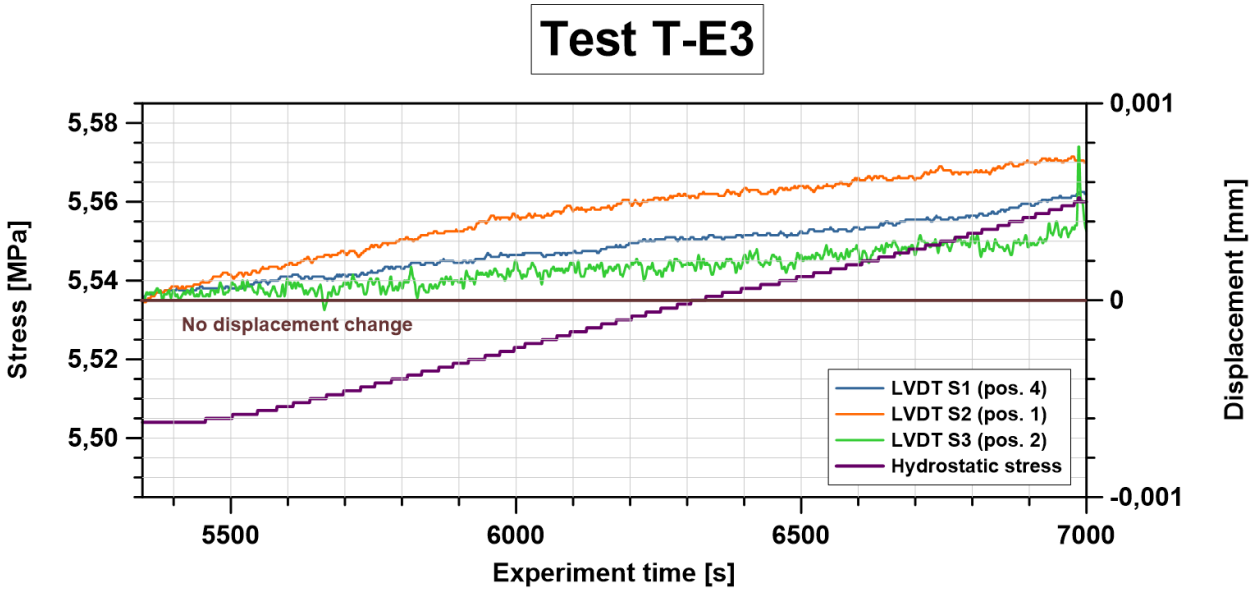

Fig. 6-32. True triaxial tests - deformations without active loading.

Tests T-D1-3 and T-E2-3 prove that deformation of the system was not sufficiently controlled in the original setup, where each axis was equipped with an individual displacement sensor. In the light of the evidence from the most recent experiments, it could be concluded that similar readings of displacement observed along S1 and S3 axes during test T-E1 could be more a result of random factors (mostly of the sensor position) than of similar characteristics of deformation. This also shows that the attempt to limit the heterogeneity of deformation of the sample under hydrostatic stress was unsuccessful despite all changes and modifications. It could be suspected than the reliability of measurements would only worsen in case of more complex stress paths. It would be impossible to distinguish between the effects of randomly heterogenous stress distribution within the system and of purposeful stress differences between particular axes.

As the main goal of using true triaxial apparatus was to investigate anisotropy of rocks, which requires strict control of stress and strain values, it was decided that the apparatus in the current technical condition should not be used for experiments on rock samples. Due to technical and time limitations, further modifications were not performed and ultrasonic setup was not plugged into the apparatus.

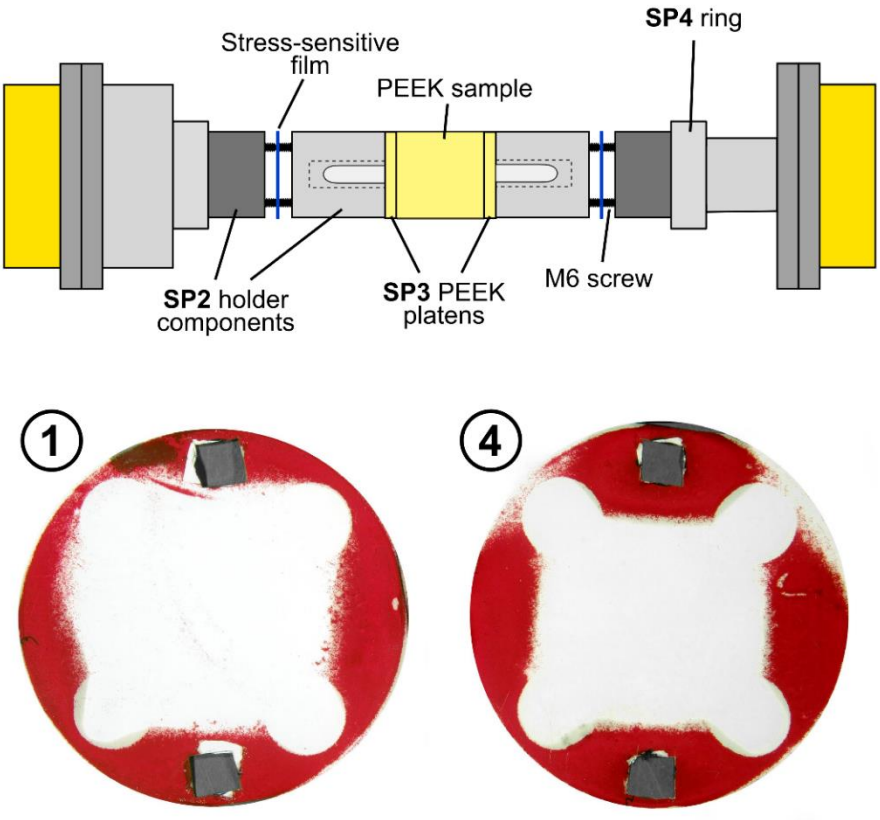

Fig. 6-33. Stress-sensitive films placement (top) and test results (bottom).

Despite the decision to cease any further modification, the last attempt to shorten the list of possible causes of the heterogenous behaviour was made. In order to investigate stress distribution in the outer pars of the sample placement system, the stress-sensitive films were placed inside the SP2 holders, in between steel components of cylinders 1 and 4 on S3 axis. The main purpose of the test was to indicate whether the stress heterogeneities appeared on the sample – platen contact or they were already present in the outer parts of the measurement column and later transferred (and probably magnified) to the sample. The stress-sensitive films placement was schematically shown (together with the test results) in fig. (6-33). The test was carried out according to the previously described standard procedure, but in this case the maximum stress was limited to 6 MPa.

The results show highly heterogenous stress distribution on the contact surface inside the SP2 holders. According to the developed films, force is transmitted almost completely by the outer part of the cylinders where the stress exceeds 10 MPa, whereas the central part of the holders experiences stresses smaller than 2 MPa. It is impossible to tell the exact values, as both observed colours are outside the colour scale provided by the film producer. Some minor anomalies (white spots) are observable in both films, but their dimensions allow to neglect them in the analysis. Shapes and areas of the central zones (not participating in stress transfer) are different for both holders which is very likely to strengthen the stress deviations and may be a result of misalignment of the entire system in relation to the actuators. The results may indicate that the central parts of the cylinder components are actually not in contact with each other. Lack of force transmission in this part of SP2 cylinders could cause so-called arching effect, decreasing the stress in the centre of theoretical contact area and increasing the stress concentration in the outer parts of the cylinder.

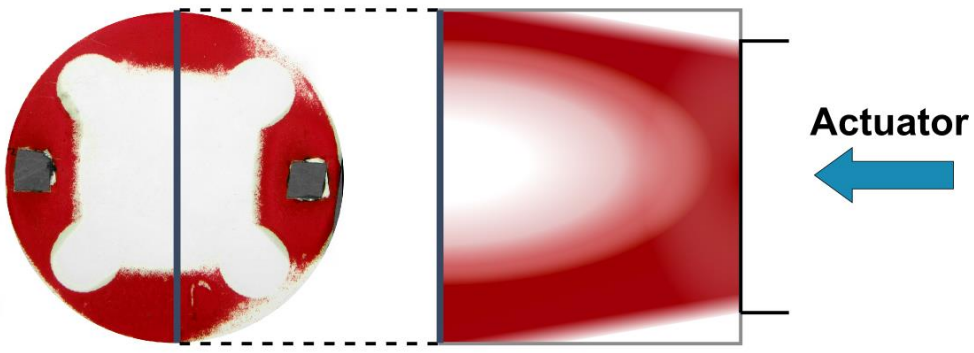

Fig. 6-34. Probable stress distribution in cross-section of SP2 cylinder.
- cross-section (right) oriented perpendicularly to the contact surface (left).

A graphical representation of the possible stress distribution inside the cylinder was shown in fig. (6-34). This effect could have significant influence on loading tests and their results, making it even more difficult to control the stress value and distribution during the measurements. To determine the source of the differences between the "white" zones it would be necessary to carry out yet more tests with the stress-sensitive films on the SP2 cylinder – actuators contacts. Unfortunately, it was determined to be impossible due to stress-sensitive film characteristics and contact location and area.

6.6. Technical report summary and conclusions

Chapter 6 was dedicated to describe all the modifications made to the true-triaxial apparatus and the tests carried out to assess the technical condition of the device. It is worth noting that in September 2016 the apparatus was prequalified for use and was assumed to require only minor alterations and maintenance work - none of the encountered complications had been expected, and hence the initial work schedule outdated almost immediately (followed by author's hopes for a successful ending much later). Therefore, in order to give a better insight into the modification process and reflect author's growing awareness of apparatus limitations and flaws, all the changes introduced in each one of the subsystems were described chronologically.

In the course of the last two months of autumn semester and the entire spring semester 2016/2017 all of the true triaxial apparatus original subsystems were modified. A total of 34 elements were manufactured to support or substitute original parts of the device, and further 25 were modified to a various extent (complete list in APPENDIX L). The hydraulic system was reshaped to bypass out-of-order electric pumps and to provide more heterogenous pressure distribution in the actuators during hydrostatic stages of loading cycle. The displacement sensors and load cells were modified to be compatible with available amplifiers. New LVDT holders were manufactured in order to limit misalignment of the transducers. Faulty sensor was substituted and dedicated adapter was made. Both loading cells and LVTDs were recalibrated multiple times to ensure high measurement quality. The sample placement system was completely reconstructed – new frame (SP1), face platens (SP3) and additional "sighting" rings (SP4) were inserted. All these new elements of the sample placement system were made for the purpose of limiting system rotation, and therefore limit heterogeneities of stress distribution on sample walls.

Despite all these changes, it was still impossible to carry out reliable measurements of stress-strain relation in the standard PEEK and aluminium cubic samples. Results of almost all tests indicated heterogenous deformation of the sample, under both uniaxial and hydrostatic stress. As the standard samples were very unlikely to have any form of anisotropy, it was a sufficient evidence of device malfunction. The discrepancies were observed for different axes and for different sensor positions along an individual axis using displacement sensors and stress-sensitive films. The registered displacements did not depend solely on force exerted by the actuators, but also LVDTs positioning. When analysed together, the data indicates that during the measurements the sample remains misaligned in relation to the stress axes. Consequently, it was not possible to reliably estimate the shortening of the sample, which is required to correct experimentally estimated ultrasonic velocity. Moreover, heterogenous deformation did not allow to prove correctness of the force-stress relations used to estimate stresses experienced by the sample. Furthermore, the original arrangement of the apparatus elements does not provide enough space for more than only one LVDT per axis during a standard triaxial experiment, making it impossible to have sufficient control over stress distribution heterogeneities. In the current technical condition of the apparatus, the error introduced by the device was too large for reliable interpretation of static and dynamic data. The shortcomings would have significant consequences on tests quality and anisotropy parameters computations, and therefore no experiments on rock samples were performed.

There are many factors that could cause heterogenous stress distribution. Due to large number of elements, interactions between them (also captured by the sensors) and spatial limitations of the obtained data it was very difficult to select the main elements responsible for the deviations of the sample. During data interpretation it was impossible to distinguish between shortening of the sample and of the entire column – LVDTs readings also captured deformation of the platens and the Teflon foil on the surface of the sample. The effects related to free space closing at the sample-SP3 platen and at SP3 platen-SP2 cylinder contacts were also observed. The described heterogeneities could as well be a result of imperfections of the system outside the measuring area of the sensors.

An attempt to identify and neutralize an individual flaw of the system was unsuccessful, nevertheless it allowed to shorten the list of possible causes. The observations from the tests carried out using LVDTs and stress-sensitive films were supported with lack of improvement despite all the modifications of particular elements of the system. All sensors were tested in

large number of various tests and their readings were found to be sufficiently precise, accurate and repeatable. Introduction of new SP1 frame, significantly reducing free spaces between the frame elements and the face platens, allowed to rule out the rotation of the platens in relation to the sample. Usage of face platens of standardized dimensions eliminated incorrect force-stress relationship as a source of discrepancies. Quality of the surface of SP3 platens have been controlled multiple times since the first imperfections were spotted. Moreover, all SP2 cylinders were precisely measured and no deviations were observed. The aluminium rings (SP4) significantly limited inaccuracy and increased repeatability of the sample placement inside the apparatus outer frame.

The most probable causes of the discrepancies, according to the author, is misalignment of the hydraulic actuators, which is later transferred to the measuring column and the sample. Deviation from the axis could be provoked by a construction defect of the outer frame (too "soft" construction, faulty element junctions, elements tilting, etc.), inaccurate actuators mounting or heterogeneous stroke of the pistons. The last of the possible reasons, although not obvious, may also play a role as the ENERPAC actuators are relatively old and were originally produced for general industrial applications where precise stroke control was not necessary. Tilting may be also caused by lack of sufficient control over the contact zone between the actuators and the sample placement system elements. Although SP4 rings limited inaccuracy of positioning of SP2 holders, a question regarding the quality of the contact is unanswered. Due to relatively small dimensions of the actuator contact surface (diameter of *32 mm*), any irregularities on its face platen may be translated into significant effects for the entire system.

The author has come up with several proposals to improve the apparatus performance. First and the most important one is to carry out detailed study of the actuators alignment. In case of proving construction defects, the actuators should be repositioned and/or substituted, preferably with devices of larger face platens dimensions (matching the dimensions of SP2 holders contact surface or bigger). Increase of the contact surface between these two elements would allow to transmit the force from actuators to the measurement column in more controllable and stable manner. Moreover, according to Cruts et al. (1995) equipping the platens with spherical seats could increase the flexibility of the system by allowing small rotations of the sample. Furthermore, it could be beneficial to adjust the entire system to larger sample dimensions. Bigger sample and larger face platens surface could significantly limit the influence of small deviations occurring in the column

and reduce the need for exceedingly precise elements placement. In order to exercise more control over the course of experiments, it would also be of great use to introduce additional displacement sensors, as the number of one LVDT per axis has been proven to be insufficient. Due to spatial limitations, it would not be possible to increase the number of standard displacement sensors around the sample. As nearly the entire surface of the sample is in contact with the face platens, it is neither possible to mount strain gauges on the sides of the specimen. An alternative solution is to install a set of at least three optical sensors (e.g. interferometers) in the current position of LVDTs on the acoustic transducer holders (SP2). Having more data on deformation of the system would allow to estimate more representative values of strain (for further static and dynamic data processing and analysis) and to control the quality of measurements more strictly. Finally, plugging working electrical pumps into the hydraulic system would give an opportunity to increase possible duration of experiments, to customize loading rate (most importantly to lower minimum feasible rate of stress change) and to limit unwanted pressure deviations. All of the above may improve the apparatus performance by further limiting time-related effects.

References

ADAMS, L. H. & WILLIAMSON, E. D. 1923. On the compressibility of minerals and rocks at high pressures. *Journal of the Franklin Institute,* 195**,** 475-529.

BACHRACH, R. & AVSETH, P. 2008. Rock physics modeling of unconsolidated sands: Accounting for nonuniform contacts and heterogeneous stress fields in the effective media approximation with applications to hydrocarbon exploration. *GEOPHYSICS,* 73**,** E197-E209.

BACKUS, G. E. 1962. Long-wave elastic anisotropy produced by horizontal layering. *Journal of Geophysical Research,* 67**,** 4427-4440.

BHUIYAN, M. H. & HOLT, R. M. 2016. Anisotropic parameters of dry and saturated sand under stress. *GEOPHYSICS,* 81**,** C229-C241.

BUDIANSKY, B. & O'CONNELL, R. J. 1976. Elastic moduli of a cracked solid. *International Journal of Solids and Structures,* 12**,** 81-97.

COYNER, K. B. 1984. *Effects of stress, pore pressure, and pore fluids on bulk strain, velocity, and permeability in rocks.* PhD, Massachusetts Institute of Technology.

CRAMPIN, S. 1990. ALIGNMENT OF NEAR-SURFACE INCLUSIONS AND APPROPRIATE CRACK GEOMETRIES FOR GEOTHERMAL HOT-DRY-ROCK EXPERIMENTS1. *Geophysical Prospecting,* 38**,** 621-631.

CRUTS, H. M. A., GROENENBOOM, J., DUIJNDAM, A. J. W. & FOKKEMA, J. T. 1995. Experimental verification of stress-induced anisotropy. *SEG Technical Program Expanded Abstracts*

DIGBY, P. J. 1981. Effective elastic moduli of porous granular rocks. *Journal of Applied Mechanics, Transactions ASME,* 48**,** 803-808.

DILLEN, M. W. P., CRUTS, H. M. A., GROENENBOOM, J., FOKKEMA, J. T. & DUIJNDAM, A. J. W. 1999. Ultrasonic velocity and shear-wave splitting behavior of a Colton sandstone under a changing triaxial stress. *GEOPHYSICS,* 64**,** 1603-1607.

FJÆR, E. 2006. Modeling the stress dependence of elastic wave velocities in soft rocks. American Rock Mechanics Association.

FJÆR, E., HOLT, R. M., RAAEN, A. M., RISNES, R. & HORSRUD, P. 2008. *Petroleum Related Rock Mechanics : 2nd Edition,* Burlington, Elsevier Science.

HERTZ, H. 1882. Ueber die Berührung fester elastischer Körper. *Journal fur die Reine und Angewandte Mathematik,* 1882**,** 156-171.

HOLT, R. M. 2016. Bounds of elastic parameters characterizing transversely isotropic media: Application to shales. *GEOPHYSICS,* 81**,** C243-C252.

HUDSON, J. A. 1981. Wave speeds and attenuation of elastic waves in material containing cracks. *Geophysical Journal of the Royal Astronomical Society,* 64**,** 133-150.

MAKSE, H. A., GLAND, N., JOHNSON, D. L. & SCHWARTZ, L. 2001. The apparent failure of effective medium theory in granular materials. *Physics and Chemistry of the Earth, Part A: Solid Earth and Geodesy,* 26**,** 107-111.

MAVKO, G. M. & NUR, A. 1978. The effect of nonelliptical cracks on the compressibility of rocks. *Journal of Geophysical Research: Solid Earth,* 83**,** 4459-4468.

MINDLIN, R. D. 1949. Compliance of elastic bodies in contact. *ASME Journal of Applied Mechanics,* 16**,** 10.

MUELLER, M. C. 1991. Prediction of lateral variability in fracture intensity using multicomponent shear-wave surface seismic as a precursor to horizontal drilling in the Austin Chalk. *Geophysical Journal International,* 107**,** 409-415.

NORRIS, A. N. & JOHNSON, D. L. 1997. Nonlinear Elasticity of Granular Media. *Journal of Applied Mechanics,* 64**,** 39-49.

NUR, A. & SIMMONS, G. 1969. Stress-induced velocity anisotropy in rock: An experimental study. *Journal of Geophysical Research,* 74**,** 6667-6674.

PRIOUL, R., BAKULIN, A. & BAKULIN, V. 2004. Nonlinear rock physics model for estimation of 3D subsurface stress in anisotropic formations: Theory and laboratory verification. *GEOPHYSICS,* 69**,** 415-425.

PRIOUL, R. & LEBRAT, T. 2004. Calibration of velocity-stress relationships under hydrostatic stress for their use under non-hydrostatic stress conditions. *SEG Technical Program Expanded Abstracts,* 23**,** 1698-1701.
RASOLOFOSAON, P. 2006. Stress-Induced Seismic Anisotropy Revisited. *Oil & Gas Science and Technology,* 53**,** 679-692.
SARKAR, D., BAKULIN, A. & KRANZ, R. L. 2003. Anisotropic inversion of seismic data for stressed media: Theory and a physical modeling study on Berea Sandstone. *GEOPHYSICS,* 68**,** 690-704.
SAYERS, C. M. 1994. The elastic anisotrophy of shales. *Journal of Geophysical Research: Solid Earth,* 99**,** 767-774.
SAYERS, C. M. & KACHANOV, M. 1996. Microcrack-induced elastic wave anisotropy of brittle rocks *Journal of Geophysical Research* 100**,** 4149–4156.
SAYERS, C. M., VAN MUNSTER, J. G. & KING, M. S. 1990. Stress-induced ultrasonic anisotrophy in Berea sandstone. *International Journal of Rock Mechanics and Mining Sciences and Geomechanics Abstracts,* 27**,** 429-436.
SINHA, B. K. & KOSTEK, S. 1996. Stress-induced azimuthal anisotropy in borehole flexural waves. *GEOPHYSICS,* 61**,** 1899-1907.
THOMSEN, L. 1986. Weak elastic anisotropy. *GEOPHYSICS,* 51**,** 1954-1966.
THURSTON, R. N. 1974. Waves in solids. *In:* TRUESDEL, C. (ed.) *Mechanics of Solids: Waves in Elastic and Viscoelastic Solids.* Berlin: Springer-Verlag.
TSVANKIN, I. 1997. Anisotropic parameters and P-wave velocity for orthorhombic media. *GEOPHYSICS,* 62**,** 1292-1309.
VERNIK, L. 1993. Microcrack-induced versus intrinsic elastic anisotropy in mature HC-source shales. *GEOPHYSICS,* 58**,** 1703-1706.
WALTON, K. 1987. The effective elastic moduli of a random packing of spheres. *Journal of the Mechanics and Physics of Solids,* 35**,** 213-226.
WHITE, J. E. 1983. *Underground sound : application of seismic waves,* Amsterdam, Elsevier.
WILD, P. 2011. Practical applications of seismic anisotropy. *First Break,* 29**,** 117-124.
ZOBACK, M. D. 2007. *Reservoir geomechanics,* Cambridge, Cambridge University Press.

Appendices

APPENDIX A - Fjær (2006) model (MATLAB script)

```
%% INPUT

clear

H=X;                    %plan wave modulus of rock without cracks or
pores
G=X;                    %shear modulus of rock without cracks or pores
n=X;              %model parameters
B=X;
m=X;
Cr_11_0=X;              %Initial crack density x-axis
Cr_22_0=X;              %Initial crack density y-axis
Cr_33_0=X;              %Initial crack density z-axis
Ten=X;                  %Parameter related to tensile strength [MPa]
v=X;                    %Poisson's ratio
fi_0=X;                 %porosity [0 - 1.0]
rho_b=X;                %solid density [g/cm3]
rho_s=rho_b/(1-fi_0); %bulk density
D=1;                          %drainage parameter
% Initial stresses [at the reference state, MPa]
T_11_r=X;         %x-axis
T_22_r=X;         %y-axis
T_33_r=X;         %z-axis
% Stresses
T_11=[X X X X X];
T_22=[X X X X X];
T_33=[X X X X X];
%Stiffness matrix elements of rock without cracks or pores
%- according to relations given by Fjaer et al.2006
c_33_r=H;
c_44_r=G;
c_11_r=H;
c_66_r=G;
c_13_r=H-2*G;
c_12_r=H-2*G;
%% Q-factors
Q_11=(16/3)*(v^2/(1-2*v))*D;
Q_33=(16/3)*((1-v)^2/(1-2*v))*D;
Q_13=(16/3)*((1-v)^2/(1-2*v))*D;
Q_12=(16/3)*((v*(1-v))/(1-2*v))*D;
Q_44=(16/3)*((1-v)/(2-v));
Q_66=0;
Q_11_p=(1/2)*(((1+v)/(1-2*v))+10*((1-2*v)/(7-5*v)));
Q_33_p=(1/2)*(((1+v)/(1-2*v))+10*((1-2*v)/(7-5*v)));
Q_13_p=((1-v)/(2*v))*(((1+v)/(1-2*v))-10*((1-2*v)/(7-5*v)));
Q_44_p=15*((1-v)/(7-5*v));
Q_66_p=15*((1-v)/(7-5*v));
%% Stress vector
d_T_11=T_11-T_11_r;
```

```
d_T_22=T_22-T_22_r;
d_T_33=T_33-T_33_r;
d_T=zeros(length(T_11),6);

for i=1:1:length(T_11)

d_T(i,1)=d_T_11(i);
d_T(i,2)=d_T_22(i);
d_T(i,3)=d_T_33(i);

end

d_T=d_T'*10^6;

%% Stiffness matrix
c_11_T0=c_11_r*(1-Q_11_p*fi_0-Q_33*Cr_11_0-Q_11*(Cr_22_0+Cr_33_0));
c_33_T0=c_33_r*(1-Q_33_p*fi_0-Q_33*Cr_33_0-Q_11*(Cr_11_0+Cr_22_0));
c_44_T0=c_44_r*(1-Q_44_p*fi_0-Q_44*(Cr_22_0+Cr_33_0)-Q_66*Cr_11_0);
c_66_T0=c_66_r*(1-Q_66_p*fi_0-Q_44*(Cr_11_0+Cr_22_0)-Q_66*Cr_33_0);
c_12_T0=c_12_r*(1-Q_13_p*fi_0-Q_13*(Cr_11_0+Cr_22_0)-Q_12*Cr_33_0);
c_13_T0=c_13_r*(1-Q_13_p*fi_0-Q_13*(Cr_33_0+Cr_11_0)-Q_12*Cr_22_0);

C=[c_11_T0 c_12_T0 c_13_T0 0 0 0; c_12_T0 c_11_T0 c_13_T0 0 0 0;...
         c_13_T0 c_13_T0 c_33_T0 0 0 0; 0 0 0 c_44_T0 0 0;...
         0 0 0 0 c_44_T0 0;0 0 0 0 0 c_66_T0];

C=C*10^9;

%% Inverting for strain

E=zeros(size(d_T));

for i=1:1:length(T_11)

E(:,i)=C\d_T(:,i);

end

%% Predefinitions
Cr_11=zeros(length(n),length(B),length(T_11));
Cr_22=zeros(length(n),length(B),length(T_11));
Cr_33=zeros(length(n),length(B),length(T_11));
c_11_FjaerLin=zeros(length(n),length(B),length(T_11));
c_33_FjaerLin=zeros(length(n),length(B),length(T_11));
c_44_FjaerLin=zeros(length(n),length(B),length(T_11));
c_66_FjaerLin=zeros(length(n),length(B),length(T_11));
E_vol=zeros(1,length(T_11));
fi=zeros(1,length(T_11));

%% Crack densities
for k=1:1:length(n)
for l=1:1:length(B)
for i=1:1:length(T_11)

E_vol(i)=E(1,i)+E(2,i)+E(3,i);              %Volumetric strain for
porosity change
F=E(3,i)-(E(1,i)+E(2,i))/2;                 %Maximum shear strain
```

```
fi(i)=(fi_0-E_vol(i))/(1-E_vol(i));          %Updated porosity

%Crack densities
Cr_11(k,l,i)=Cr_11_0*(((T_11_r+Ten)/(T_11(i)+Ten))^n(k))*(1-
(B(l)*(2*E(1,i)-E(2,i)-E(3,i))+m*F^2));
Cr_22(k,l,i)=Cr_22_0*(((T_22_r+Ten)/(T_22(i)+Ten))^n(k))*(1-
(B(l)*(2*E(2,i)-E(1,i)-E(3,i))+m*F^2));
Cr_33(k,l,i)=Cr_33_0*(((T_33_r+Ten)/(T_33(i)+Ten))^n(k))*(1-
(B(l)*(2*E(3,i)-E(2,i)-E(1,i))+m*F^2));

%Effective elastic stiffness coefficients
c_11_FjaerLin(k,l,i)=c_11_r*(1-Q_11_p*fi(i)-Q_33*Cr_11(k,l,i)-
Q_11*(Cr_22(k,l,i)+Cr_33(k,l,i)));
c_33_FjaerLin(k,l,i)=c_33_r*(1-Q_33_p*fi(i)-Q_33*Cr_33(k,l,i)-
Q_11*(Cr_11(k,l,i)+Cr_22(k,l,i)));
c_44_FjaerLin(k,l,i)=c_44_r*(1-Q_44_p*fi(i)-
Q_44*(Cr_22(k,l,i)+Cr_33(k,l,i))-Q_66*Cr_11(k,l,i));
c_66_FjaerLin(k,l,i)=c_66_r*(1-Q_66_p*fi(i)-
Q_44*(Cr_11(k,l,i)+Cr_22(k,l,i))-Q_66*Cr_33(k,l,i));

end
end
end

%% PLOT
X_plot(c_33_FjaerLin,c_44_FjaerLin,T_11,n,B)

%% Error
%Summed squares of residuals
[SquareError]=X_error(c_11_FjaerLin, c_33_FjaerLin,c_44_FjaerLin,
c_66_FjaerLin);

%Average percentage error
[PercError]=X_error(c_11_FjaerLin, c_33_FjaerLin,c_44_FjaerLin,
c_66_FjaerLin);
```

APPENDIX B - Prioul et al. (2004) model (MATLAB script)

```
clear

%% Input

clear

rho_b=X;              %bulk density [g-cm3]
fi=X;                 %porosity [0-1.0]

rho_s=rho_b/(1-fi);     %solid porosity

%Third rank stiffness tensor elements estimation (from the paper)for
T_referebce

c_111 =X;
c_112 =X;
c_123 X;
c_144=(c_112-c_123)/2;
c_155=(c_111-c_112)/4;

%Thomsen's parameters
Vp0=X; %axial P-wave velocity [km/s]-reference state
Vs0=X; %axial S-wave velocity [km/s]-reference state
e=X;   %epsilon -reference state
g=X;   %gamma -reference state
d=X;   %delta -reference state

%Stiffness matrix elements
c_33_r=Vp0^2*rho_b;
c_44_r=Vs0^2*rho_b;
c_11_r=2*e*c_33_r+c_33_r;
c_66_r=2*g*c_44_r+c_44_r;
c_12_r=c_11_r-2*c_66_r;

%C13 approximation
delta=4*c_44_r^2-4*(c_44_r^2-2*d*c_33_r*(c_33_r-c_44_r)-(c_33_r-
c_44_r)^2);
delta_a=1;
delta_b=2*c_44_r;
delta_c=c_44_r^2-2*d*c_33_r*(c_33_r-c_44_r)-(c_33_r-c_44_r)^2;
c_13_1=(-delta_b-sqrt(delta))/(2*delta_a);
c_13_2=(-delta_b+sqrt(delta))/(2*delta_a);

if c_13_1 > 0
    c_13_r=c_13_1;
else
    c_13_r=c_13_2;
end

%% Stress vector

T_r=X; %reference state hydrostatic stress [MPa]

%Stress cycle
```

```
T_11=[X X X X X];
T_22=[X X X X X];
T_33=[X X X X X];
T_11=T_11-T_r;
T_22=T_22-T_r;
T_33=T_33-T_r;

T=zeros(length(T_11),6);

for i=1:1:length(T_11)
T(i,1)=T_11(i);
T(i,2)=T_22(i);
T(i,3)=T_33(i);
end

T=T'*10^6;
%% Stiffness matrix

C=[c_11_r c_12_r c_13_r 0 0 0; c_12_r c_11_r c_13_r 0 0 0;...
         c_13_r c_13_r c_33_r 0 0 0; 0 0 0 c_44_r 0 0;...
         0 0 0 0 c_44_r 0;0 0 0 0 0 c_66_r];

C=C*10^9;

%% Inverting for strain

E=zeros(size(T));

for i=1:1:length(T_11)
E(:,i)=C\T(:,i);
end

%% Predefinitions

c_11_Prioul=zeros(1,length(T_11));
c_33_Prioul=zeros(1,length(T_11));
c_44_Prioul=zeros(1,length(T_11));
c_66_Prioul=zeros(1,length(T_11));

%% New stiffness coefficients & velocities

for j=1:1:length(T_11)
c_11_Prioul(j)=c_11_r+c_111*E(1,j)+c_112*(E(2,j)+E(3,j));
c_33_Prioul(j)=c_33_r+c_111*E(3,j)+c_112*(E(1,j)+E(2,j));
c_44_Prioul(j)=c_44_r+c_144*E(1,j)+c_155*(E(2,j)+E(3,j));
c_66_Prioul(j)=c_66_r+c_144*E(3,j)+c_155*(E(1,j)+E(2,j));
end

Vs_axial=sqrt(c_44_Prioul/rho_b);
Vs_radial=sqrt(c_66_Prioul/rho_b);
Vp_axial=sqrt(c_33_Prioul/rho_b);
Vp_radial=sqrt(c_11_Prioul/rho_b);

%% PLOTS
```

```
Prioul_Colton_plot(c_33_Prioul,c_11_Prioul,c_44_Prioul,c_66_Prioul,V
p_axial,Vp_radial,Vs_axial,Vs_radial)

%% Error

[SquareError,PercError]=Errors(c_11_Prioul,c_33_Prioul,c_44_Prioul,c
_66_Priou;

Error_sum=sum(SquareError);
PercError_ave=(PercError(1)+PercError(2)+PercError(3)+PercError(4))/
4;)
```

APPENDIX C - Prediction error estimation (MATLAB script)

```
function [SquareError,PercError]=Errors(c,11,c_33,c_44,c_66)

%% Experimental values

c_11_exp_1=[X X X X X];
c_33_exp_1=[X X X X X];
c_44_exp_1=[X X X X X];
c_66_exp_1=[X X X X X];

...

%% Average values

c_11_ave=c_11_exp;
c_33_ave=c_33_exp;
c_44_ave=c_44_exp;
c_66_ave=c_66_exp;

%% Square errors

SE_c_11=sum((c_11_ave-c_11).^2);
SE_c_33=sum((c_33_ave-c_33).^2);
SE_c_44=sum((c_44_ave-c_44).^2);
SE_c_66=sum((c_66_ave-c_66).^2);

%% Percentage errors

Pe_c_33_p=zeros(1,length(c_33));
Pe_c_44_p=Pe_c_33_p;
Pe_c_11_p=Pe_c_33_p;
Pe_c_66_p=Pe_c_33_p;


for k=1:1:length(c_33)

Pe_c_33_p(k)=abs(((c_33_ave(k)-c_33(k))/(c_33_ave(k)))*100);
Pe_c_44_p(k)=abs(((c_44_ave(k)-c_44(k))/(c_44_ave(k)))*100);
Pe_c_11_p(k)=abs(((c_11_ave(k)-c_11(k))/(c_11_ave(k)))*100);
Pe_c_66_p(k)=abs(((c_66_ave(k)-c_66(k))/(c_66_ave(k)))*100);

end

Pe_c_33=sum(Pe_c_33_p)/length(c_33);
Pe_c_44=sum(Pe_c_44_p)/length(c_44);
Pe_c_11=sum(Pe_c_11_p)/length(c_11);
Pe_c_66=sum(Pe_c_66_p)/length(c_66);

SquareError=[SE_c_11 SE_c_33  SE_c_44 SE_c_66];
PercError=[Pe_c_11 Pe_c_33 Pe_c_44 Pe_c_66];
```

APPENDIX D - Inversion for third-order elastic stiffness coefficients (MATLAB script)

```
%% Input parameters
T_r=X;                      %Reference hydrostatic stress [MPa]

%Rest of the points
T_11=[X X X X X];
T_22=[X X X X X];
T_33=[X X X X X];
rho_b=2.38;           %Bulk density [g/cm3]

T_r=T_r*10^6;
T_11=T_11*10^6;
T_22=T_22*10^6;
T_33=T_33*10^6;

%%Stiffness coefficients at reference point [GPa]

c_33_r=X;
c_11_r=X;
c_44_r=X;
c_66_r=X;
% c_13_r=0;                %C_13 may be given or may be computed
below

c_33_r=c_33_r*10^9;
c_11_r=c_11_r*10^9;
c_44_r=c_44_r*10^9;
c_66_r=c_66_r*10^9;

%Thomsen's parameters
Vp0=X;                %axial P-wave velocity [km/s]-reference state
Vs0=X;                %axial S-wave velocity [km/s]-reference state
e=X;                  %epsilon -reference state
g=X;                  %gamma -reference state
d=X;                  %delta -reference state

%C13 approximation
delta=4*c_44_r^2-4*(c_44_r^2-2*d*c_33_r*(c_33_r-c_44_r)-(c_33_r-
c_44_r)^2);

delta_a=1;
delta_b=2*c_44_r;
delta_c=c_44_r^2-2*d*c_33_r*(c_33_r-c_44_r)-(c_33_r-c_44_r)^2;

c_13_1=(-delta_b-sqrt(delta))/(2*delta_a);
c_13_2=(-delta_b+sqrt(delta))/(2*delta_a);

if c_13_1 > 0
    c_13_r=c_13_1;
else
    c_13_r=c_13_2;
end
```

```
c_12_r=c_11_r-2*c_66_r;
%% Stiffness coefficients at measurement point [except for the
reference point] - experimental [GPa]

c_33=[X X X X X];
c_44=[X X X X X];
c_11=[X X X X X];
c_66=[X X X X X];

c_33=c_33*10^9;
c_11=c_11*10^9;
c_44=c_44*10^9;
c_66=c_66*10^9;




if length(T_11)==length(c_33)
else
    disp(' ')
    disp('WARNING!!! C_ij coefficients not inserted')
    disp(' ')
    return
end

%% Inverting for strains

T=zeros(6,length(T_11));
E=zeros(6,length(T_11));
E_11=zeros(size(T_11));
E_22=E_11;
E_33=E_11;

for i=1:1:length(T_11)

T(1,i)=T_11(i)-T_r;
T(2,i)=T_22(i)-T_r;
T(3,i)=T_33(i)-T_r;

end

C=[c_11_r c_12_r c_13_r 0 0 0;...
   c_12_r c_11_r c_13_r 0 0 0;...
   c_13_r c_13_r c_33_r 0 0 0;...
   0 0 0 c_44_r 0 0;...
   0 0 0 0 c_44_r 0;...
   0 0 0 0 0 c_66_r];


for i=1:1:length(T_11)

E(:,i)=C\T(:,i);

E_11(i)=E(1,i);
E_22(i)=E(2,i);
E_33(i)=E(3,i);
```

```
end

%% Inverting for third order elastic coefficients

C_ij=zeros(4*length(T_11),1);
E_coeff=zeros(length(T_11),3);

for i=1:1:length(T_11)
C_ij((i*4)-3)=c_11(i)-c_11_r;
C_ij((i*4)-2)=c_33(i)-c_33_r;
C_ij((i*4)-1)=c_66(i)-c_66_r;
C_ij(i*4)=c_44(i)-c_44_r;
end

for i=1:1:length(T_11)
E_coeff((i*4)-3,:)=[E_11(i) E_22(i)+E_33(i) 0];
E_coeff((i*4)-2,:)=[E_33(i) E_11(i)+E_22(i) 0];
E_coeff((i*4)-1,:)=[(0.25*(E_22(i)+E_11(i))) (0.5*E_33(i)-
0.25*(E_11(i)+E_22(i))) (-0.5*E_33(i))];
E_coeff((i*4),:)=[(0.25*(E_22(i)+E_33(i))) (0.5*E_11(i)-
0.25*(E_33(i)+E_22(i))) (-0.5*E_11(i))];
end

C_ijk=pinv(E_coeff)*C_ij;

%% Display

c_111_GPa=C_ijk(1)/10^9;
c_112_GPa=C_ijk(2)/10^9;
c_123_GPa=C_ijk(3)/10^9;
c_144_GPa=(c_112_GPa-c_123_GPa)/2;
c_155_GPa=(c_111_GPa-c_112_GPa)/4;

table(c_111_GPa,c_112_GPa,c_123_GPa,c_144_GPa,c_155_GPa)
```

APPENDIX E - Calibration support elements (C1 and C2)

Steel load cell support element C1 (left) and PVC support C2 (right).

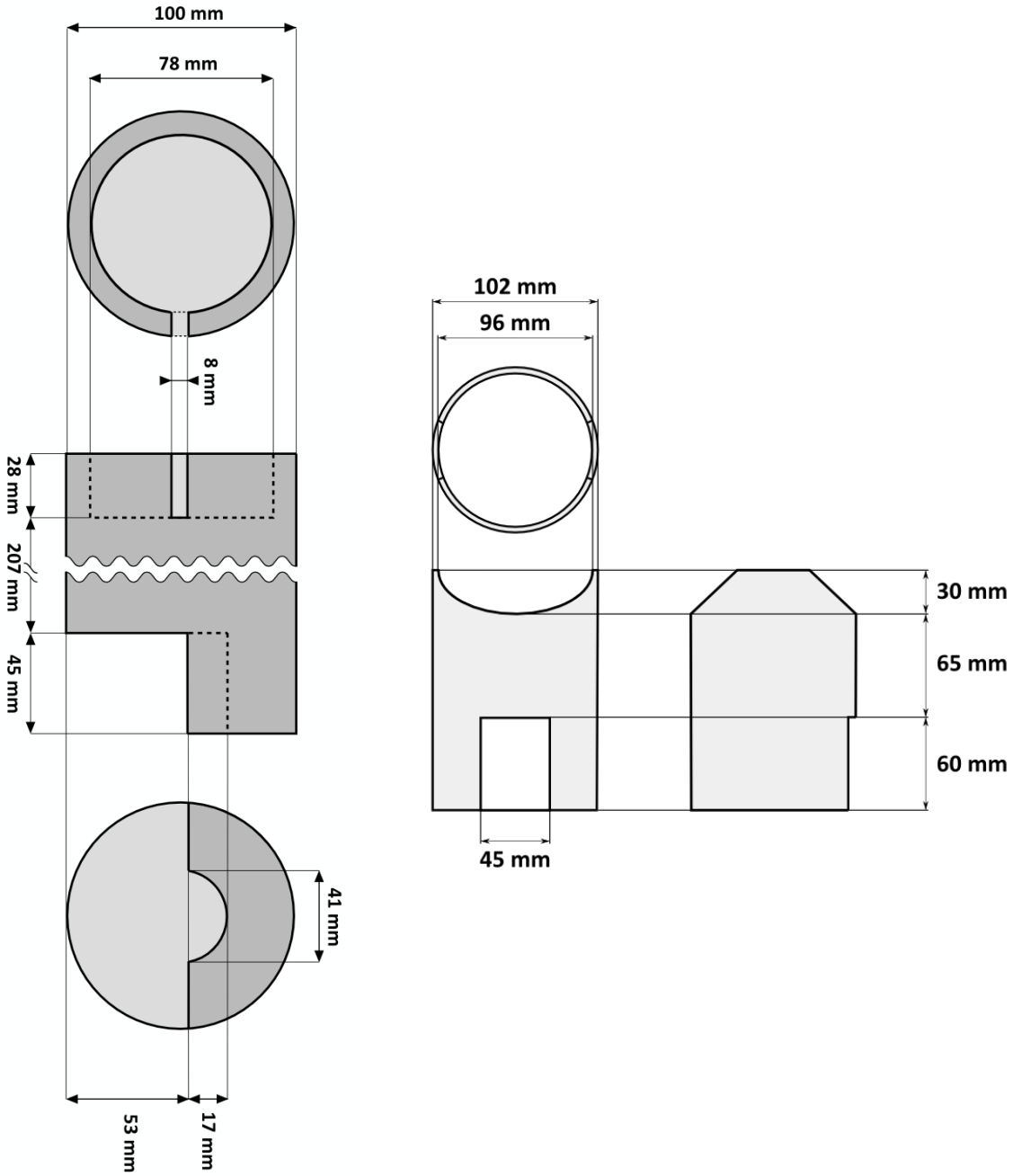

APPENDIX F - Load cells calibration

SENSOTEC verification

Force [kN]	
MTS Insight system	**Sensotec**
0.00	0.00
2.05	1.90
6.07	5.77
20.18	19.90
59.90	59.80
100.60	100.60
160.05	160.04
159.94	159.89
99.82	99.50
9.88	9.62
2.61	2.49
0.00	0.06

HBM C2 calibration

	Force [kN]	**Signal [mV/V]**
S1	0.31	-0.0011
	158.50	1.5936
S2	0.09	-0.0216
	159.7	1.5895
S3	1	0.0108
	159.2	1.6004

HBM C2 verification

Force [kN]					
Sensotec	**S1**	**Sensotec**	**S2**	**Sensotec**	**S3**
0.10	0.4	0.22	0.26	0.03	0.03
1.92	2.0	2.20	2.32	2.11	2.31
6.02	5.95	6.00	5.95	6.05	6.30
20.02	20.12	21.00	20.91	20.30	20.31
60.00	60.00	60.00	60.00	60.50	60.17
100.00	100.34	100.50	100.51	100.50	99.70
160.00	160.62	161.00	161.02	159.12	159.12
145.00	145.62	141.70	141.92	149.30	149.33
101.51	120.06	96.00	96.30	99.27	99.53
10.85	10.55	10.70	10.50	11.20	11.29
2.58	2.64	2.80	2.72	2.58	2.67
0	0.04	0	0	0.02	0.09

APPENDIX G - Aluminium frame elements (SP1)

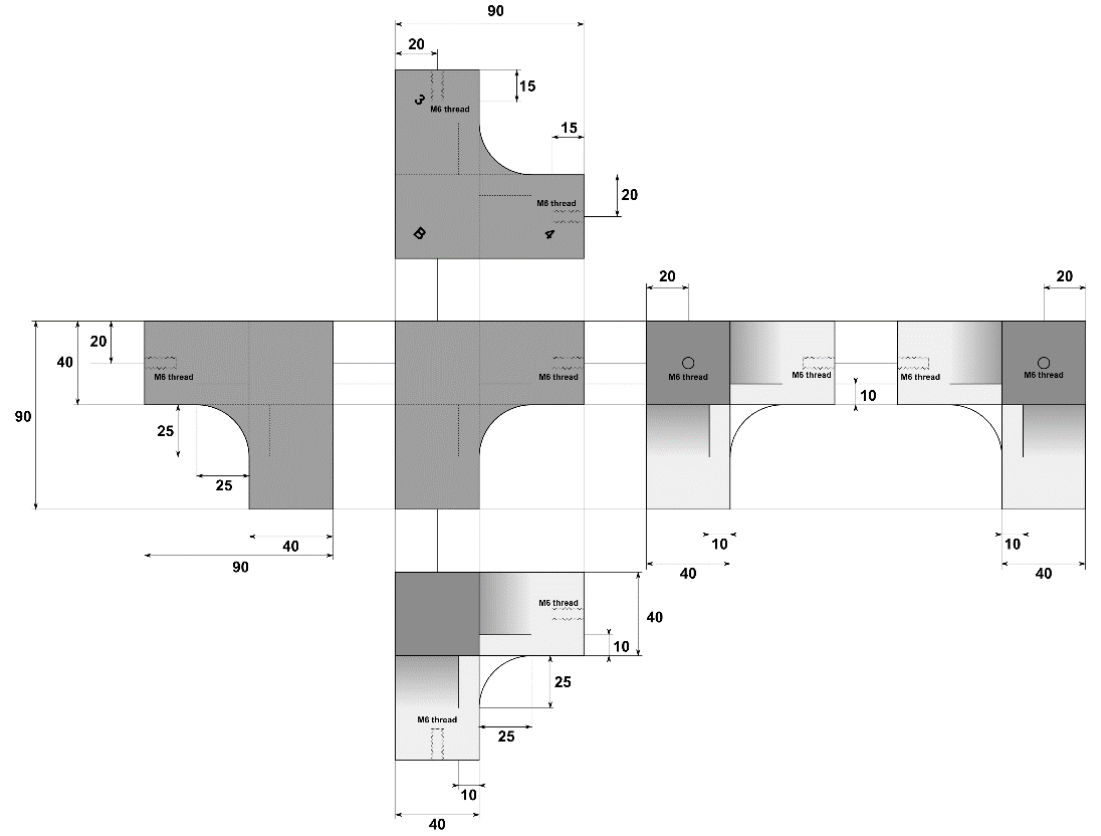

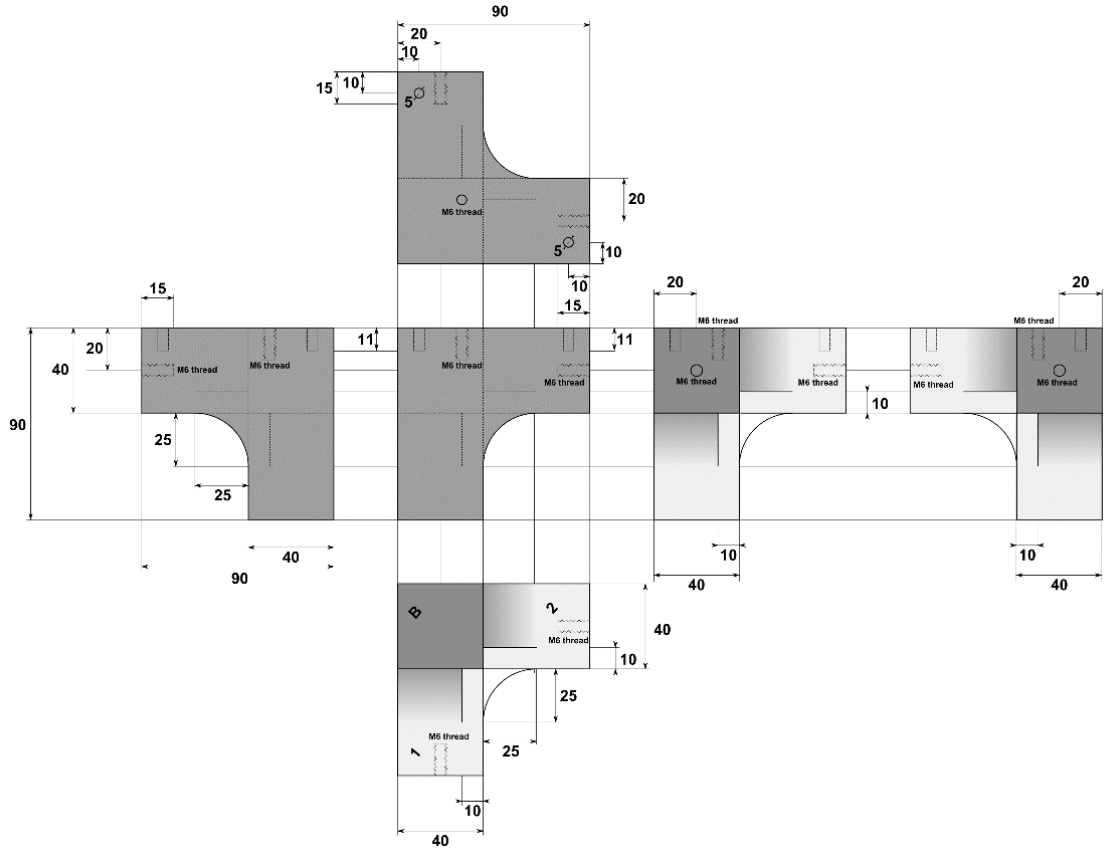

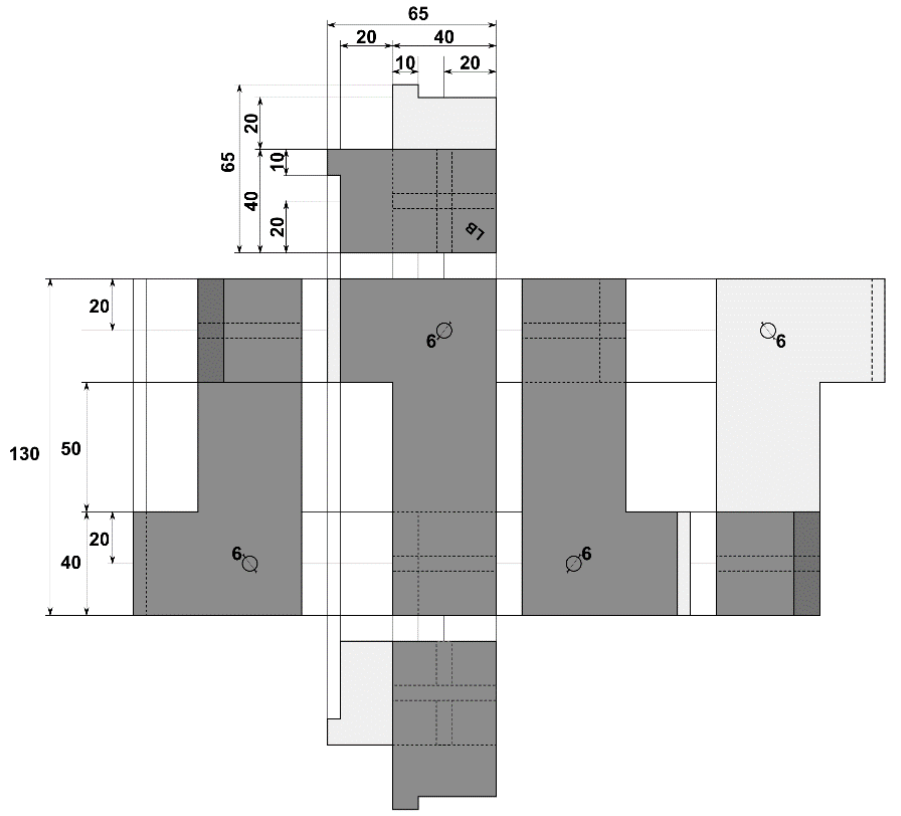
65
20
40
10
20
65
20
10
40
20
R7
20
130
50
20
40
6
6
6
6

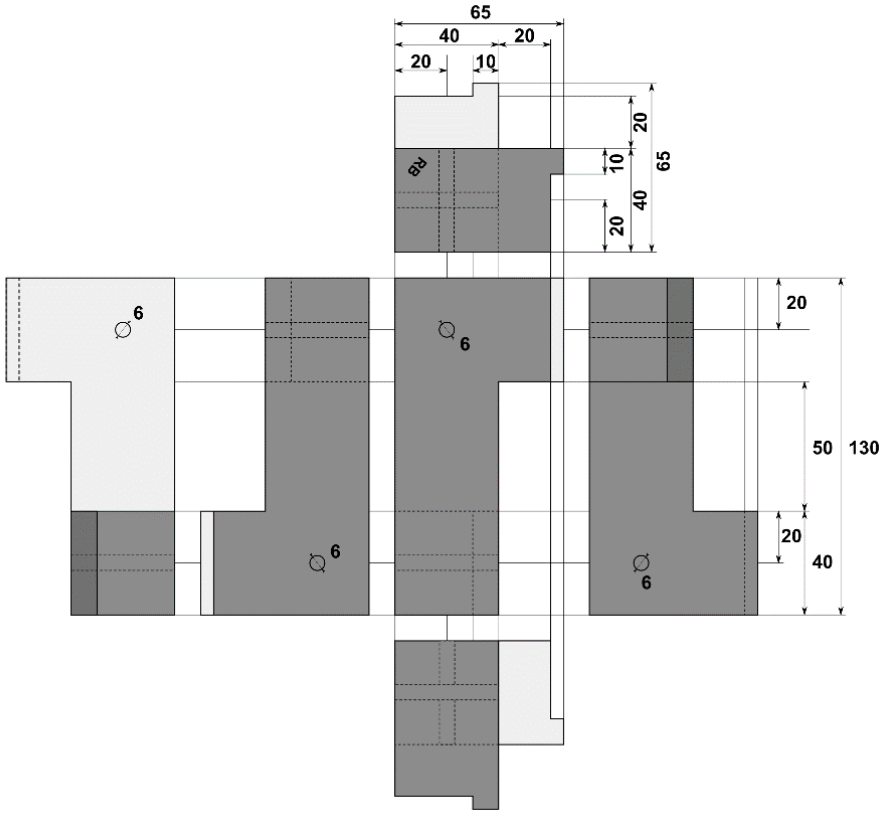
65
40
20
20
10
20
10
40
65
R8
20
6
6
6
20
50
130
20
40
6
6

APPENDIX H - Modified face platens (SP3)

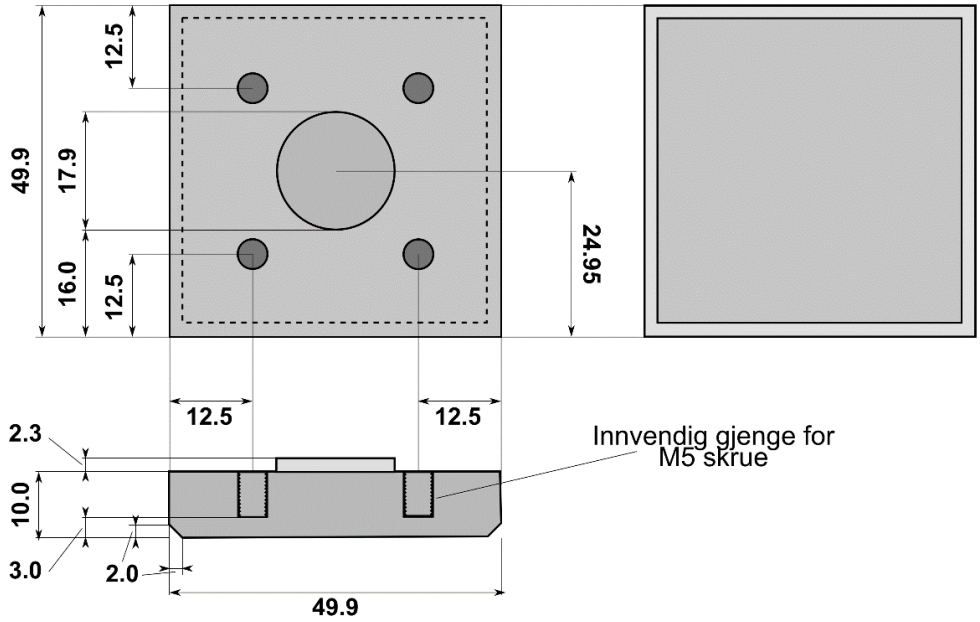

APPENDIX I - Aluminium rings (SP4)

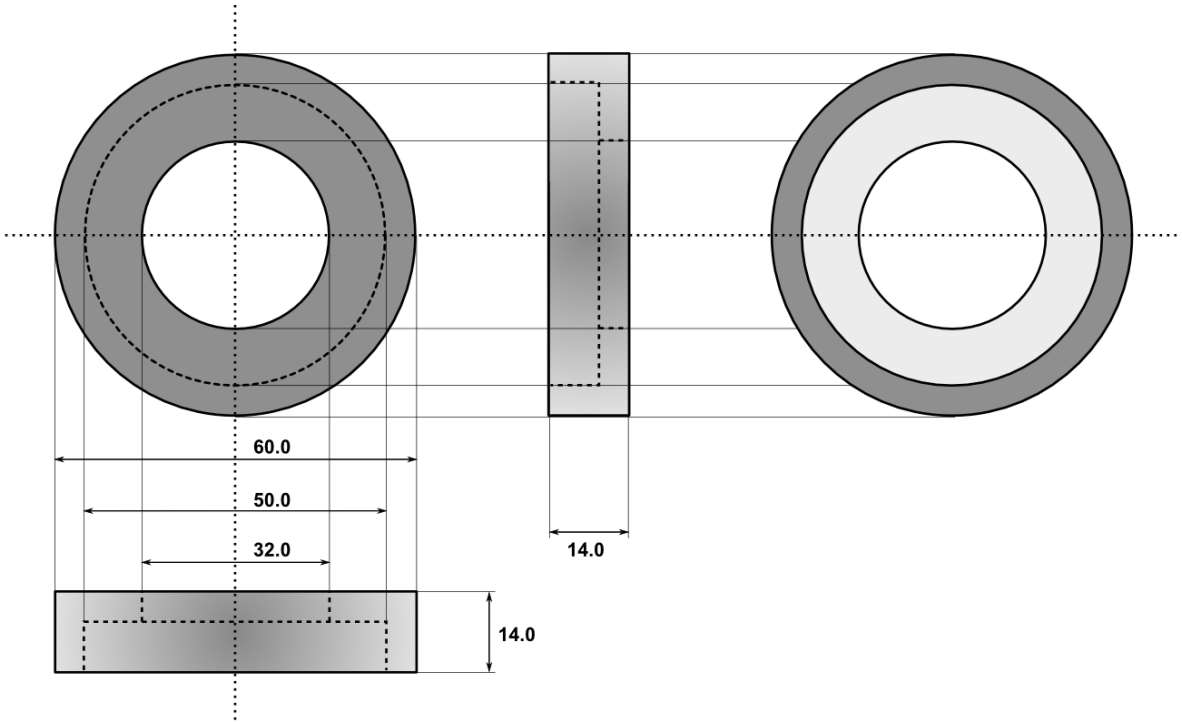

APPENDIX J - LVDT holders (H1)

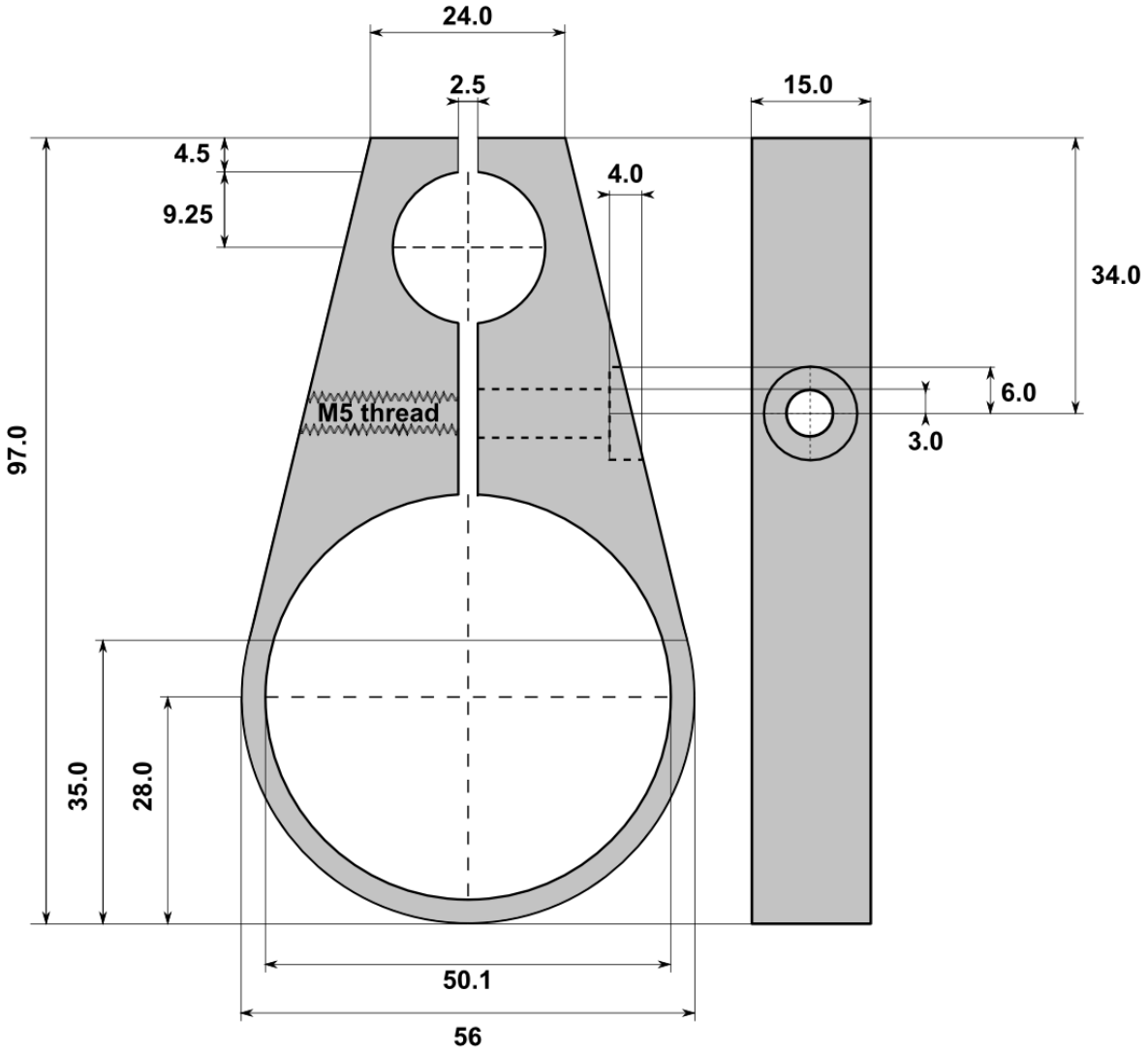

APPENDIX K - HBM LVDT adapter (H2)

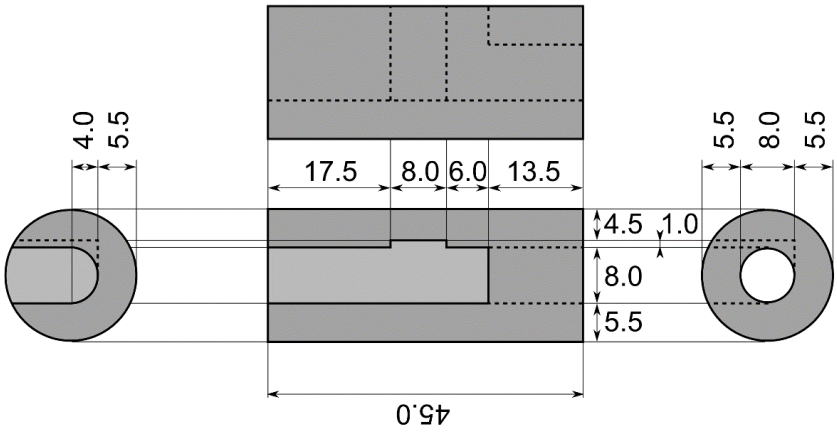

APPENDIX L - modified and produced apparatus elements.

New elements	
Name	**Quantity**
SP3 - PEEK face platens	15
SP3 – Aluminium face platens	4
SP1 - frame elements	4
C1 & C2 - Calibration support holders	2
SP2 - LVDT holders	3
H2 – LVDT adapters	2
Pipes for hydraulic system	3
PEEK cube	1
SUM	**34**

Modified elements	
Name	**Quantity**
SP3 - PEEK face platens	12
LVDT connectors	4
Load cells connectors	4
Hydraulic valves	5
SUM	**25**

APPENDIX M - Risk assessment

ID	16788	**Status**	**Date**
Area	Risikovurdering: Helse, miljø og sikkerhet (HMS)	Created	18.12.2016
Created by	Marcin Ireneusz Duda	Assessed	18.12.2016
Assigned to	Marcin Ireneusz Duda	Actions decided	
		Closed	18.12.2016

Stress-induced Anisotropy – from Theory to Experimental Systems.

Hazard: **Heavy equipment**

Incident: **Crush injury**

Konsekvensområde: Helse

Risk before planned actions: 

Risk after planned actions: 

Hazard: **Electricity**

Incident: **Electrocution**

Konsekvensområde: Helse

Risk before planned actions: 

Risk after planned actions: 

Hazard: **Poisonous fumes**

Incident: **Poisoning**

Konsekvensområde: Helse

Risk before planned actions: 

Risk after planned actions: 

Hazard: **Heat**

Incident: **Skin burn**

Konsekvensområde: Helse

Risk before planned actions: 

Risk after planned actions: 

Final result

All the risks are in the acceptable risk range, although the uncerainity of the assessment may be significant as was made by the tool user with use of the safety instructions.